الجمهورية الجزائرية الديمقراطية الشعبية
People's Democratic Republic of Algeria
وزارة التعليم العالي والبحث العلمي
Ministry of Higher Education and Scientific Research
المدرسة الوطنية العليا لعلوم البحر وتهيئة الساحل
High National School for Marine Sciences and Coastal Management

Final thesis project to obtain the Diploma
State Engineer in Marine Sciences
Option: Coastal Management and Protection

Topic:

Wave overtopping predictions using machine learning technique

Presented by:

- **Brahim Mohammed**
- **Alkama Hafsa Hadil**

Presented on 13/07/2023, in front of the jury composed of:

Mme. FEZAA N.	Professor ENSSMAL	President
M. MEZOUAR K.	Professor ENSSMAL	Advisor
M. GHOGGALI S.	Assistant professor B ENSEREDD	Co-advisor
M. DAHMANI AEA.	Assistant professor ENSSMAL	Examinator
Mme. FELLAH H.	Ph.D. student at ENSSMAL	BMC Examinator
M AINOUZ O.	Technical Director	Economic partner

Academic year: 2022/2023

Acknowledgments

At the end of this work, I thank Almighty God for granting me health, courage, and determination to complete this modest piece of work.

I am particularly grateful to my supervisor, Mr. MEZOUAR K., Professor at ENSSMAL, for guiding me throughout the process of this work. Despite his administrative responsibilities, his availability, guidance, and advice enabled me to successfully carry out this work. Please accept, Sir, the expression of my respectful consideration and profound admiration for all your scientific and human qualities.

I am immensely grateful to my co-supervisor, Mr. GHOGGALI S., Associate Professor at ENSER in Batna, who kindly accompanied and guided me in the Machine Learning and wave channel part. I want to express my deep gratitude for your support and unwavering kindness despite your professional responsibilities and the distance.

I would like to express my sincere gratitude to Ms. SALEM CHERIF Y., a teacher at ENSSMAL, for her guidance and valuable advice during the completion of my first three chapters. Despite her multiple commitments, she dedicated time and energy to provide exceptional guidance.

I extend my profound appreciation to Ms. MAOUEL D. and Ms. FELLAH H., teachers at ENSSMAL, for their support and valuable advice during the completion of the BMC part. Despite their numerous responsibilities, they generously devoted time to guide me.

It is with great pleasure that I thank Mr. DAHMANI AEA. for taking the time to review the scientific part of my work.

I also express my heartfelt gratitude to Ms. FELLAH H. for taking the time to review the BMC part of my work.

I would like to thank Ms. FEZAA N., a professor at ENSMAL, for agreeing to preside over my thesis defense.

Finally, I extend my gratitude to all those who have contributed directly or indirectly to the completion of this thesis.

Dedication

First and foremost, I would like to thank GOD

For giving me the strength and courage

to successfully complete this modest work.

I would like to dedicate this work to all those who believed in me and supported me throughout this journey:

To my dear mother and my beloved father, who have been my greatest supporters and always pushed me to give my best.

In loving memory of my grandfather, whose wisdom and encouragement continue to inspire me, and to my grandmother, whose unwavering love and strength have been a guiding light in my life.

To my dear sisters Amina and Dhoha

To my brothers: Omar and Abderezzak

To my close friends Alla, Mostafa, Rayan, Ilyas, Hicham, Lyna Abir, Nawel, and Meriem, who have been there for me in both good times and bad, always reminding me to believe in myself

To my classmates and colleagues, with whom I shared unforgettable moments and who encouraged me in my endeavors.

To all the special people in my life, who have inspired me and brought joy and happiness.

This dedication is for all of you because without your love, encouragement, and support, this work would not have been possible. I am grateful for everything you have done and for being a part of my life.

Table of Contents

List of Figures

List of Tables

List of Equations

List of Terms

$\mathbf{A}$	Horizontal viscosity.
$\mathbf{A_c}$	Armour crest freeboard of the structure
$\mathbf{B}$	Width of the berm
$\mathbf{B_h}$	Width of the horizontally schematized berm
$\mathbf{B_t}$	Width of the toe of the structure
$\mathbf{c_{pl}}$	Plunging coefficient
$\mathbf{c_s}$	Surging coefficient
$\mathbf{cot_{\alpha d}}$	Cotangent of the slope of the structure downward of the berm
$\mathbf{cot_{\alpha excl}}$	Mean cotangent of the slope of the structure, without contribution of the berm
$\mathbf{cot_{\alpha incl}}$	Mean cotangent of the slope of the structure, with contribution of the berm
$\mathbf{cot_{\alpha u}}$	Cotangent of the slope of the structure upward of the berm
$\mathbf{d}$	Water depth.
$\mathbf{f}$	Coriolis parameter
$\mathbf{g}$	Gravity acceleration.
$\mathbf{G_c}$	Width of the structure crest
$\mathbf{h}$	Water depth
$\mathbf{h_b}$	Water depth on the berm
$\mathbf{h_{deep}}$	Water depth at deep water
$\mathbf{h_t}$	Water depth on the toe of the structure
$\mathbf{H}$	The local wave height.
$\mathbf{H_{10\%}}$	Average of the 1/10 of the upper values of the record
$\mathbf{H_{2\%}}$	Average of the 2% of the upper values of the record
$\mathbf{H_b}$	Wave height at the toe of the structure.
$\mathbf{H_m}$	Average height
$\mathbf{H_{m0}}$	The spectral significant wave height.
$\mathbf{H_{m0\ deep}}$	Significant wave height from spectral analysis, determined at deep water
$\mathbf{H_{\ m0\ toe}}$	Significant wave height from spectral analysis at the toe of the structure.
$\mathbf{H_s}$	Significant wave height, H1/3 of the incident waves at the toe of the structure.
$\mathbf{k_\Delta}$	layer coefficient.
$\mathbf{K_d}$	Stability coefficient.
$\mathbf{L_0}$	The theoretical wavelength of the offshore wave.
$\mathbf{M_{50}}$	The median mass of armour stone.
$\boldsymbol{n}$	Number of layers.
$\boldsymbol{Pa}$	Atmospheric pressure.
$\mathbf{P}$	Notional permeability of the structure.
$\mathbf{Pow}$	Percentage of the waves resulting in overtopping
$\boldsymbol{\rho_0}$	The reference density of water.
$\boldsymbol{\rho_c}$	the apparent concrete density (kg/m³).
$\boldsymbol{\rho_r}$	the apparent rock density (kg/m³).
$\boldsymbol{\rho_w}$	the apparent water density (kg/m³).
$\mathbf{s_0}$	The fictitious wave steepness.
$\mathbf{s_{om}}$	wave steepness with Lo, based on Tm
$\mathbf{S}$	Amplitude of discharge caused by point sources.
$\boldsymbol{\sigma}$	Wave action density.
$\boldsymbol{t}$	Time.

$\tan \alpha B$	Tangent of the slope of the berm
T_{ij}	Lateral stresses.
T_m	the mean energy wave period.
$T_{m\ deep}$	Mean period either from spectral analysis or from time domain analysis at deep water
$T_{m-1,0\ deep}$	Mean period from spectral analysis at deep water
$T_{m-1,0}$	The mean energy wave period.
$T_{m\ -1,0\ toe}$	Mean period from spectral analysis at the toe of the structure
$T_{\ m\ toe}$	Mean period either from spectral analysis at the toe of the structure.
T_{max}	Maximum period value of the record.
$T_{p\ deep}$	Peak period from spectral analysis at deep water
$T_{p\ toe}$	Peak period from spectral analysis at the toe of the structure
T_s	Average period of the top 1/3 of the record.
$T_{s-1,0}$	The spectral mean energy wave period (s).
$T_{10\%}$	Average of the 1/10 of the upper period values of the record.
u	Velocity component in the x direction.
u_s	Velocity at which water is discharged into the ambient water.
v	Velocity component in the y direction.
v_s	Velocity at which water is discharged into the ambient water.
$\vec{v}$	Velocity of propagation of a wave group (in the four-dimensional c_x,c_y,c_σ,c_θ)
V_m	*A*verage height
V_{max}	Maximum value of the record
V_{min}	Minimum value of the record
V_s	Average of the top 1/3 of the record
w	Velocity component in the z direction.
$x.\ y\ ,\ z$	Cartesian coordinates.
$\overrightarrow{\nabla x}$	Two-dimensional differential operator in the space $\vec{x}$.
R_c	Crest freeboard of the structure
$R_{d1\%}$	The run-down exceeded by 1% of waves.
$R_{d2\%}$	The run-down exceeded by 2% of waves.
$R_{u2\%}$	The run-up exceeded by 2% of waves.
γ_b	the berm factor.
γ_f	Roughness/permeability factor for the structure
γ_v	correction factor for a vertical wall on the slope.
γ_β	the correction factor for oblique waves.
ν_t	Turbulent vertical viscosity.
ξ_{cr}	critical value of the surf similarity parameter.
ξ_m	breaker parameter based on s_m
$\xi_{m-1,0}$	breaker parameter based on $s_{\mathrm{m-1,0}}$
ξ_p	breaker parameter based on s_p
τ_{bx}, τ_{by},	x and y components of bottom wind stress.
τ_{sx}, τ_{sy}	x and y components of surface wind stress.
Δ	Relative buoyant density.
q	Overtopping discharge per second per meter width $[m^3/s.m]$
Ω	Angular velocity of rotation.
∇	Four-dimensional differential operator in the space: (x, y, σ, θ.)
α	The slope angle (°).
β	Angle of wave attack relative to the normal on the structure

List of Acronyms

AI	Artificial Intelligence
ANN	Artificial Neural Networks Artificial Neural Networks
BM	Block maxima
CETMEF	Centre d'Études Techniques Maritimes et Fluviales
CF	Complexity Factor
CLASH	Crest Level Assessment of Coastal Structures by full scale monitoring, neural network prediction and Hazard Analysis on permissible wave overtopping
DHI	Danish Hydraulic Institute
ENSSMAL	Ecole Nationale Supérieure des Science de la Mer et de l'Aménagement du Littoral
EurOtop	European Overtopping Manual for Coastal Structures.
EVT	Extreme value theory
FM	Flexible mesh
GBMs	Gradient Boosting Machines
GEBCO	General Bathymetric Chart of the Oceans
GEV	generalized extreme value
GIS	geographic information system
IPCC	Intergovernmental Panel on Climate Change
HD	hydrodynamic
ML	Machine Learning
NAVIONICS	Navigation Electronics
NGA	Niveau general algerien
POT	Peaks over Threshold Method
Rd	Run dowm
RF	Reliability Factor
Ru	Run up
SW	Spectral Waves
SWL	still water level
TAW	Technical Advisory on Wave run-up
TVC	Tout-venant de carrière
XGBoost	Extreme Gradient Boosting

Introduction

Coastal engineering is a multidisciplinary field that seeks to comprehend the complex interactions between waves, coastal structures, and the shoreline. Waves play a fundamental role in shaping coastal environments and significantly influence the design and construction of various coastal works, including ports, shore protection measures, and coastal defense structures. Understanding the effects of waves on coastal areas is crucial for ensuring the safety and stability of coastal communities. To enhance our comprehension of these dynamics, extensive research has been conducted, drawing insights from esteemed coastal engineering reference books such as the "Shore Protection Manual" (CERC, 1984), the rock armor guide (CETMEF, 2009), and the "Coastal Engineering Manual" (U.S. Army Corps of Engineers, 2012).

Overtopping, the phenomenon where waves exceed the crest of coastal structures and flow onto protected areas, has significant implications for ports. It poses safety risks to personnel, vessels, and infrastructure, while also eroding protective structures and contributing to coastal erosion. Its events disrupt port operations, causing delays and financial losses. Predicting and understanding overtopping is then important. Our estimation of wave overtopping relies on extensive global research that has employed diverse Machine Learning methods. Several notable studies have been instrumental in this field, including the research conducted by Verhaeghe, H., Meer, J. W., et al. (2003); Gosse, J. S., Jentsje Wouter, v. d.., et al. (2004); Gent, M. R., Boogaard, H. F., et al. (2007); Bieman, J. P., al, J. M. (2020); and a, J. P., Gent, M. R. (2021). Additionally, we have benefited from the pioneering contributions of Amara, L. and Chalal, Y. (2022), who were the first students to introduce this subject at ENSSMAL.

This thesis aims to investigate the wave and wind climate, extreme events, breakwater design, hydraulic performance, overtopping prediction using machine learning techniques and a study of the wave flume. By integrating these various aspects, this thesis aims to contribute to the development of robust coastal engineering practices and effective strategies for mitigating overtopping risks in wave-impacted areas.

In the first chapter, we focus on the wind and wave climate off Algiers Bay. This study begins by analyzing a database of about 30 years records to draw rose diagrams and extract the frequent directions in order to understanding the wave characteristics.

Accurate statistical analyses of measured wave data time series enable us to estimate the extreme wave events and their associated probabilities using the theory of extreme values. To obtain reliable results, statistical treatment is done in chapter two. The wave height associated with the return period are extracted. In fact, these analyses provide crucial information for designing coastal defense structures with the appropriate level of protection.

Numerical simulations and modeling techniques have evolved, allowing for more precise and efficient analysis of wave behavior. In the third chapter, we utilize the DHI Mike 21 software to simulate wave and current behavior along Algiers Bay. This was done in order to estimate wave properties reaching Algiers and Marina ports.

The design of these structures relies on accurate formulas such the empirical formulas of Hudson and Van Der Meer. In chapter four, these formulas are used to design the rubble mound breakwaters which were used in the focused study area.

Chapter five focus on the interaction between waves and hydraulic structures, such as rubble mound breakwaters. Various hydraulic responses, including wave run-up, wave run-down, and overtopping, influence the stability and performance of these structures. Understanding these phenomena is necessary for optimizing the design and hydraulic stability of coastal protection structures.

In recent years, machine learning techniques have gained significant prominence in engineering fields, including coastal engineering. By utilizing these methods, researchers have been able to develop overtopping prediction models. In Chapter Six of this work, an analysis of well-known works in this field is explored. Furthermore, a new machine learning model is presented, specifically focusing on predicting overtopping for rubble mound breakwaters, which demonstrates its effectiveness for these types of coastal structures.

In the last chapter, a study of the wave flume is presented, employing the first-order wavemaker theory, which serves as the foundation for wave generation in wave flumes. This topic, leading to the development of a significant tool in physical modeling, is being explored and approached for the first time at ENSSMAL. The wave flume, serving as a laboratory tool, provides researchers with the means to study and comprehend wave behavior on a smaller scale. Consequently, we can acquire valuable insights into wave characteristics and their impacts on coastal areas. Understanding the principles of wavemaker design and operation enhances indeed our understanding of wave behavior. This study was inspired by the notable work presented in the book "Physical Models and Laboratory Techniques in Coastal Engineering" (Steve,1993) which served as a valuable resource.

Chapter I. Climatological data for the study area

I.1. Introduction

According to Shore Protection Manual (U.S. Army Corps of Engineers, 2012), the effects of waves are important in the field of coastal engineering. Waves determine the geometry and composition of beaches and have a significant effect on the design and construction of ports, waterways, shore protection measures, coastal structures, and other coastal works. Surface waves generally derive their energy from the winds.

In this chapter, we will analyze the wind and wave climate off Algiers Bay. which is a necessary point for the following chapters.

I.2. Study area geographical location

The Algiers Bay, situated on the Mediterranean coast of Algeria to the west of Algiers, is a vast expanse of water. It stretches approximately 15,27 kilometers from Cape Matifou, situated in the town of Bordj-el-Bahri, in the east, to Cape Caxine in the west. and is characterized by its calm and shallow waters, with a maximum depth of approximately 50 meters. The Bay of Algiers benefits from the protection effect of the surrounding mountains, which provide protection against strong winds. As a result, it serves as a natural and easily accessible harbor, ensuring safety for maritime activities.

Our study areas in Algiers Bay are

The Algiers Marina is bounded by the following geographic coordinates

Longitude: 3°8'41.42"E to 3°9'15.45"E.
Latitude: 36°44'29.35"N to 36°44'43.60"N.

On the other hand, the Algiers Port is bounded by the following geographic coordinates

Latitude: 36°45'24.92"N to 36°47'18.46"N.
Longitude: 3°03'55.29"E to 3°04'37.18"E.

Figure I-1 Map of the geographical location of Algiers Bay and study area.

I.3. General information about waves

Wave is an undulatory movement of the sea surface that is formed by a distant wind field away from the observation area called the Fetch zone. Typically, the surface of the sea displays a continuous series of nearly identical, parallel undulations that move uniformly towards the shoreline (Bonnfille. R., 2010).

The wave is primarily characterized by its wavelength L, its amplitude H, its celerity C, and its period T. Furthermore, there are significant parameters required for classification, such as the ratio of height H to wavelength L (steepness H/L), and the relative depth d.

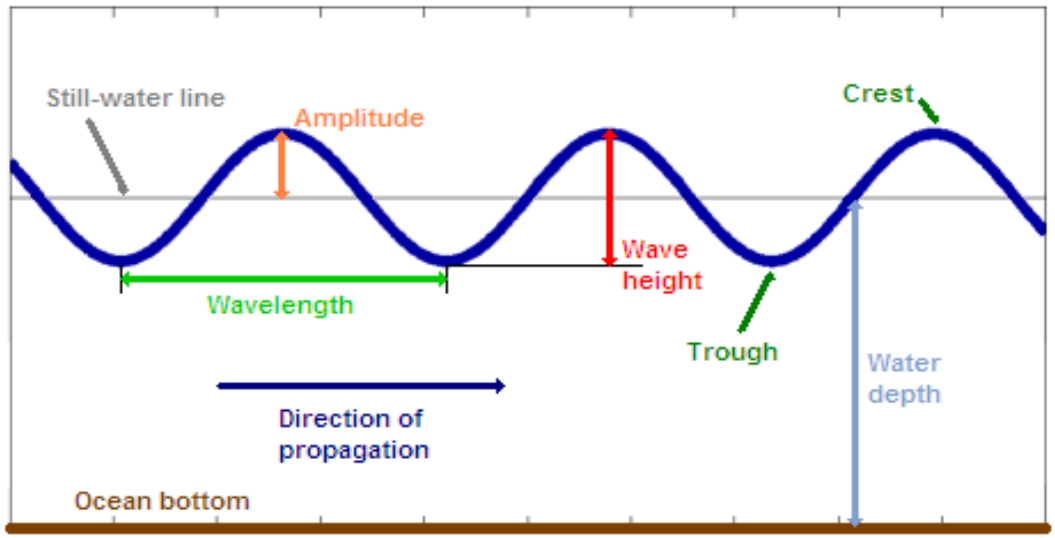

Figure I-2 Wave parameters.

I.4. Climatological data for the study area

This section focuses on the analysis of wave and wind climate in the study area. It provides an overview of the extracted wave data, including significant wave height and period, as well as wave direction distribution. Additionally, it presents the recorded wind speed data and analyzes wind direction patterns throughout thirty years.

I.4.1. Wave climate

Wave climate is defined as the distribution of wave height, period, and direction in which they occur. It is determined by averaging these wave properties over a specific time period and location.

The 30-year wave climate data used in the presented study is extracted from infoplaza. We have chosen the extraction point located at 37°N latitude and 3°E longitude Figure I-3, which covers a larger time interval from 1992 to 2021. This data consists of a vast collection of 87,665 wave records, recorded at regular intervals of three hours. Each record includes 21 parameters, capturing various aspects of the wave characteristics.

Table I-1 Coordinates of the recording.

Longitude	37N	Registration start date	End of registration
Latitude	3E	01/01/1992	31/12/2021

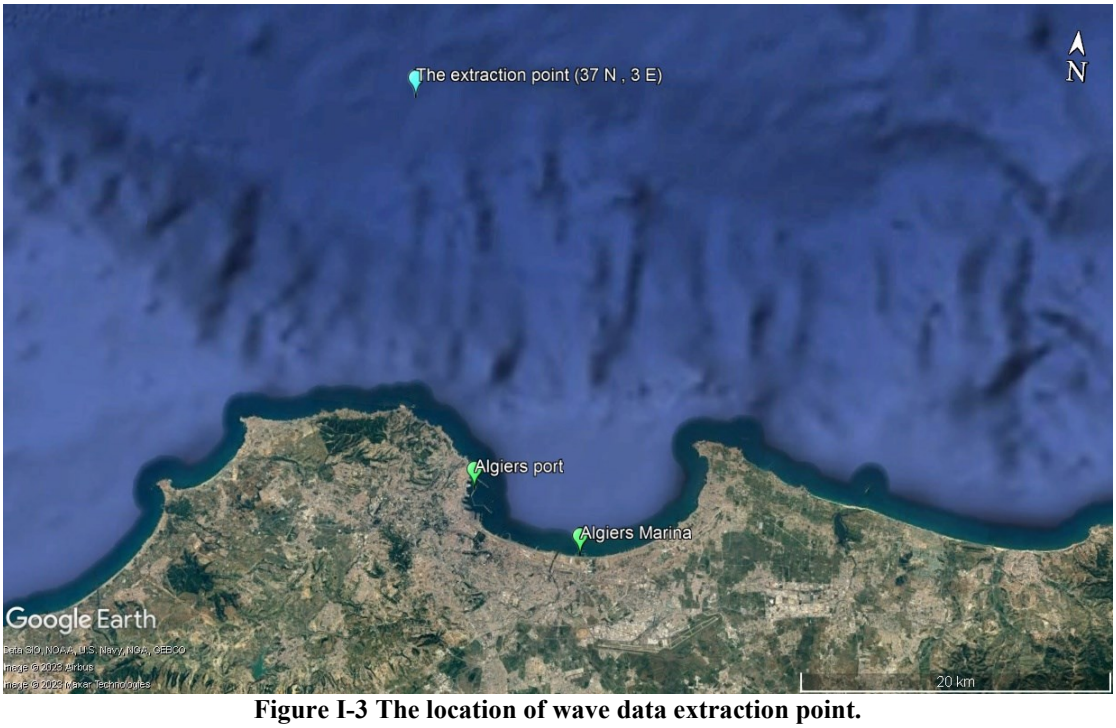

Figure I-3 The location of wave data extraction point.

Significant height: The significant wave height (Hs) varies between 0.03 m and 7.48m with an average of 1.16m over the entire 30-year period 1992-2021.

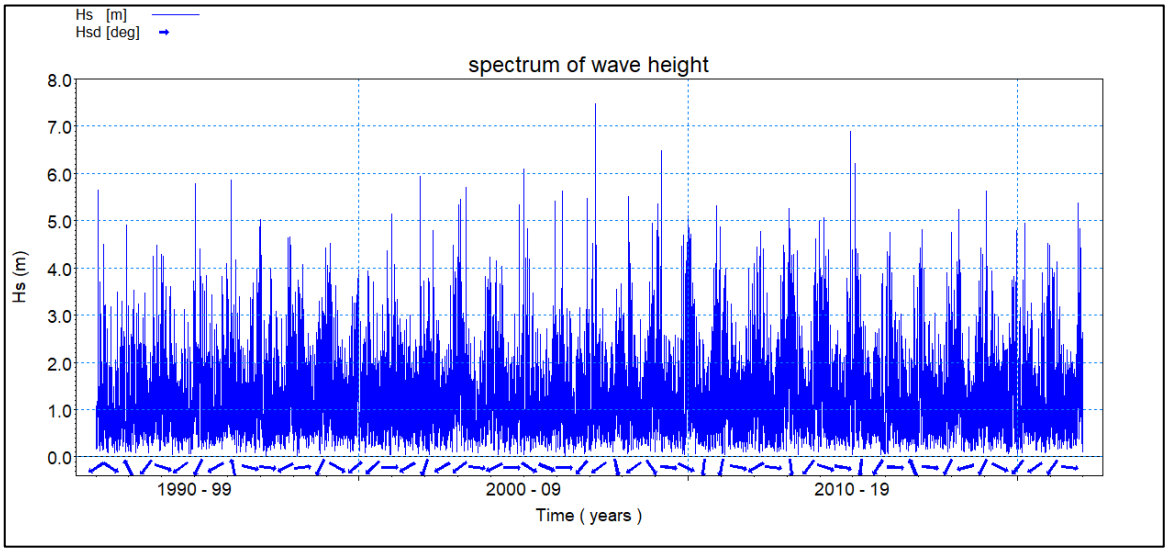

Figure I-4 Representation of the spectrum of recorded wave heights.

From the spectrum Figure I-4 we can see that most of the waves are smaller than 4m, with extreme values every 4-6 years that exceed 5m.

Table I-2 Significant wave heights

Wave heights		Value (m)
H_m	Average height	1.16
H_s	Average of the top 1/3 of the record	2.00
$H_{10\%}$	Average of the 1/10 of the upper values of the record	2.84
$H_{2\%}$	Average of the 2% of the upper values of the record	3.88
H_{max}	Maximum value of the record	7.48

Peak period: The recorded periods vary between 2.74s to 15.99s, the highest density in the Figure above is globally located between 4s and 10s.

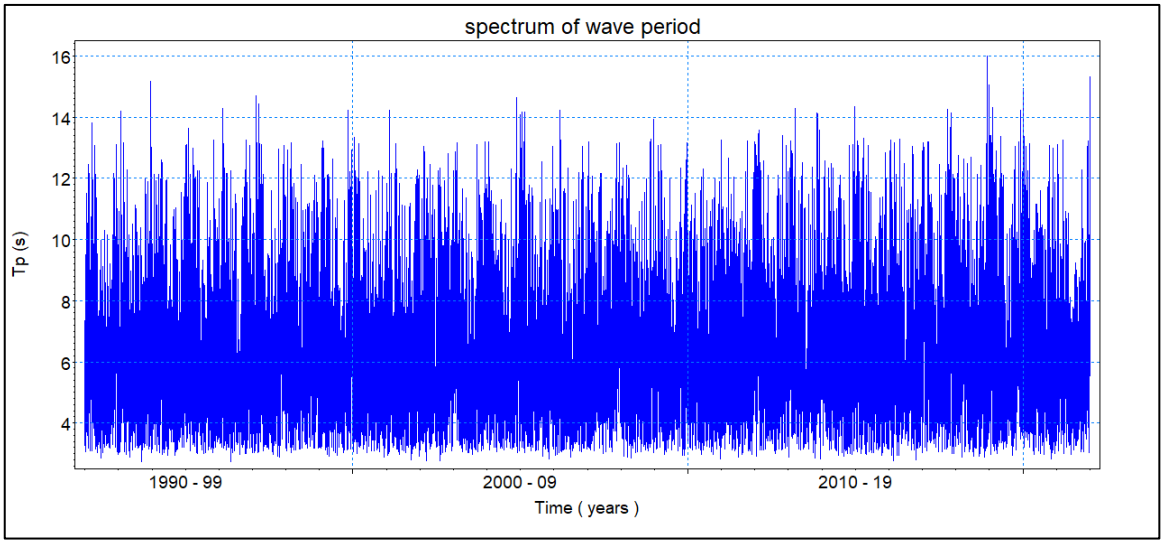

Figure I-5 Representation of the spectrum of recorded wave periods.

Statistical analysis of offshore wave period allowed us define some Wave periods represented in Table I-3

Table I-3 Period of significant wave.

Wave periods		Value (s)
T_m	Average period.	6.46
T_s	Average period of the top 1/3 of the record.	8.50
$T_{10\%}$	Average of the 1/10 of the upper period values of the record.	10.15
T	Of the maximum height.	10.47
T_{max}	Maximum period value of the record.	15.99

Statistical analysis of offshore wave directions allowed us to plot annual and seasonal roses and define some significant wave height represented in Table I-4.

Table I-4 Annual and seasonal frequency of occurrence of offshore waves by direction.

	Annual (%)	Winter (%)	Spring (%)	Summer (%)	Autumn (%)
N (0°)	14.10	20.90	14.52	7.04	14.73
NE (45°)	44.08	26.87	43.32	65.56	42.22
E (90°)	3.43	2.56	3.59	4.76	2.96
SE (135°)	0.77	1.23	0.49	0.13	1.28
S (180°)	1.19	2.51	0.53	0.21	1.58
SW (225°)	0.95	2.02	0.52	0.19	1.12
W (270°)	25.61	31.40	28.36	17.03	26.93
NW (315°)	8.75	12.51	8.68	5.08	9.18

From the annual wave rose Figure I-6, we can see the dominance of two directions: North-East and West nearly 70% of all waves blowing off Algiers Bay with a peak height recorded reach more than 7,48m come from North sector.

- North-East direction: with a 44% percentage of annual time with a higher frequency of occurrence in summer (65%) than in winter (27%).
- West direction: with a 26% percentage of annual time with a higher frequency of occurrence in winter (31%) than in summer (17%).

From the monthly wave roses Figure I-7,we can classify three categories of waves (calm and agitated and alternate between both of them):

- Calm wave during the months: June, July, August and September with heights lower than 3 m overall.
- More agitated wave during the months: October, November, April and May with an alternation between calm and agitated weather in however, several peaks of more than 4 m in height were recorded.
- On the other hand, the remaining months: December, January, February and March record heights exceeding 5 m during the year.

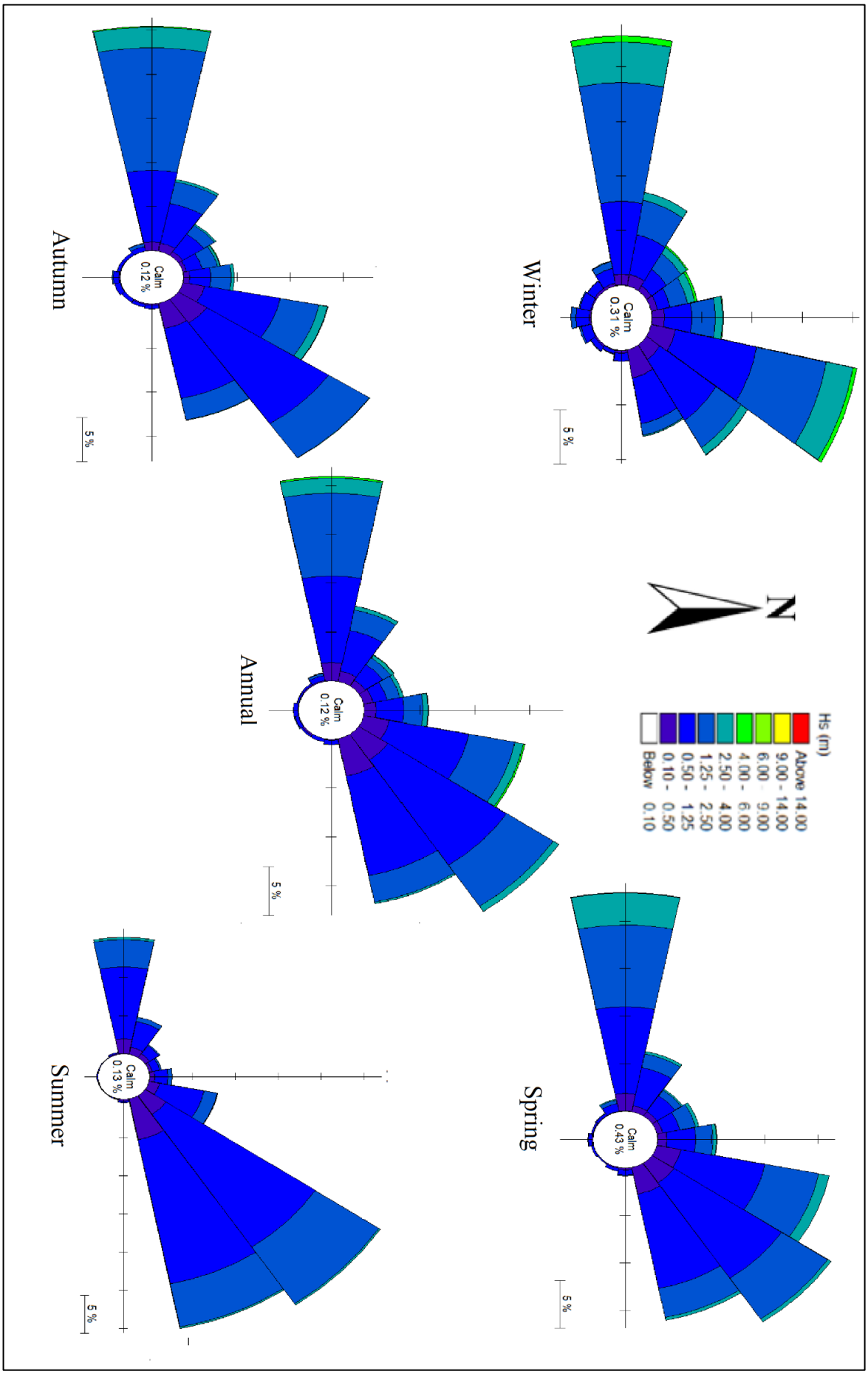

Figure I-6 Annual and seasonal wave roses recorded from 1992 - 2021 at 37° N and 3° E.

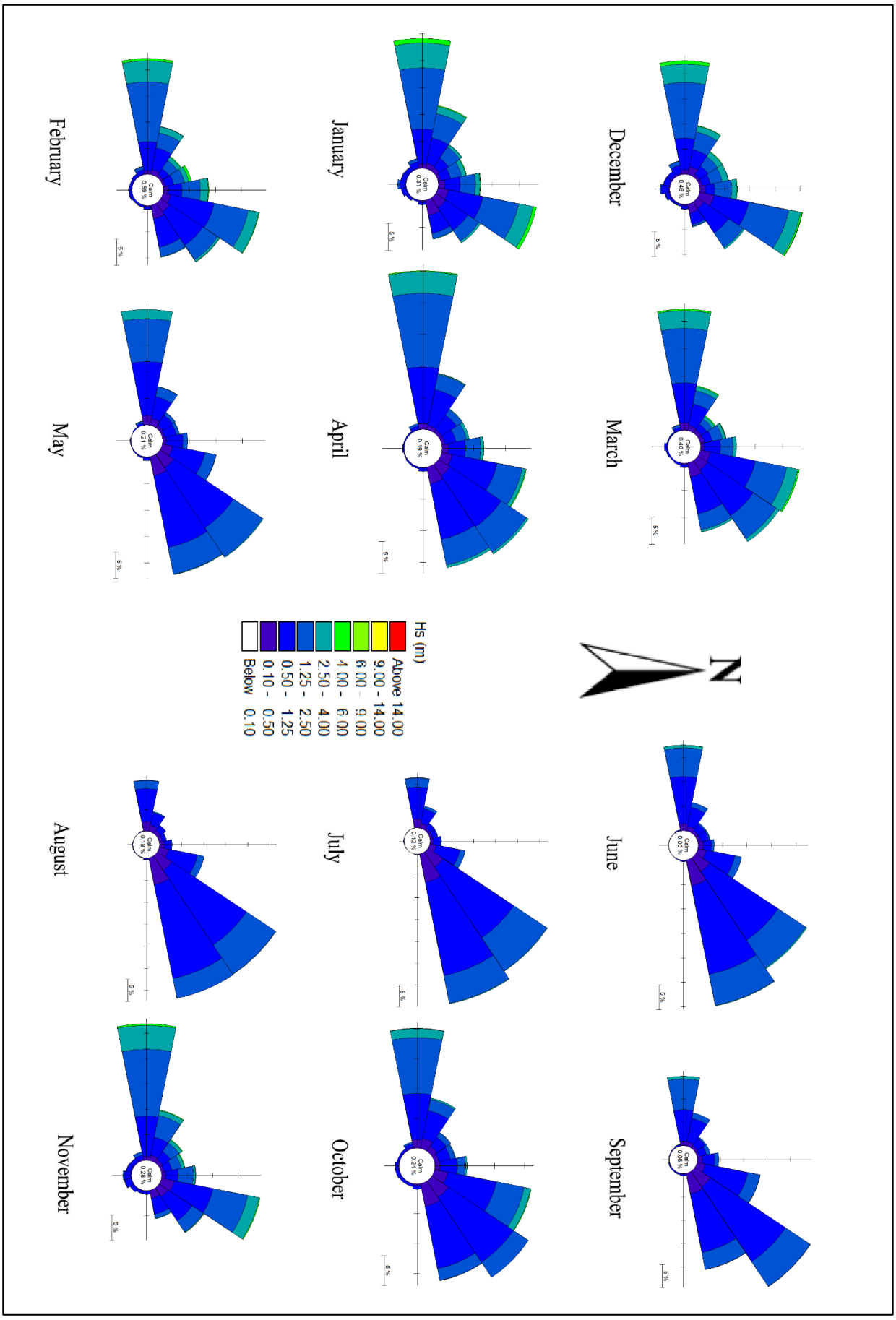

Figure I-7 Monthly wave roses recorded from 1992 - 2021 at 37° N and 3° E.

To visualize the distribution of height and period data, they have been represented in a diagram with marginal distributions in Figure I-8.

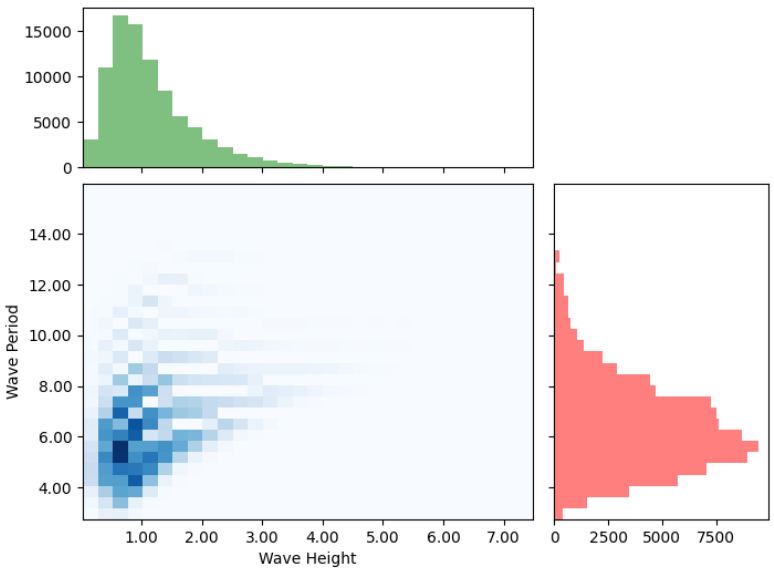

Figure I-8 Diagram with marginal distributions of wave heights and periods.

Figure I-8 illustrates the correlation between wave height and its corresponding period. Notably, there is a dense cluster of data points (dark blue) representing wave heights ranging from 0.02 m to 1.4 m, with corresponding periods falling between 3s and 8s.

Additionally, wave heights below 3.5 m often coincide with periods around 10s, as indicated by a significant proportion of the data.

I.4.2. Wind climate

The wind has a significant influence on the wave. a study on the wind climate in the same extraction point 37° N 3° E was done over the period 1992 - 2021 with data from the infoplaza database. The recorded wind speed varies between 0.2m/s to 5.53m/s, the highest density Figure I-9 is globally located between 0.2 and 15m/s.

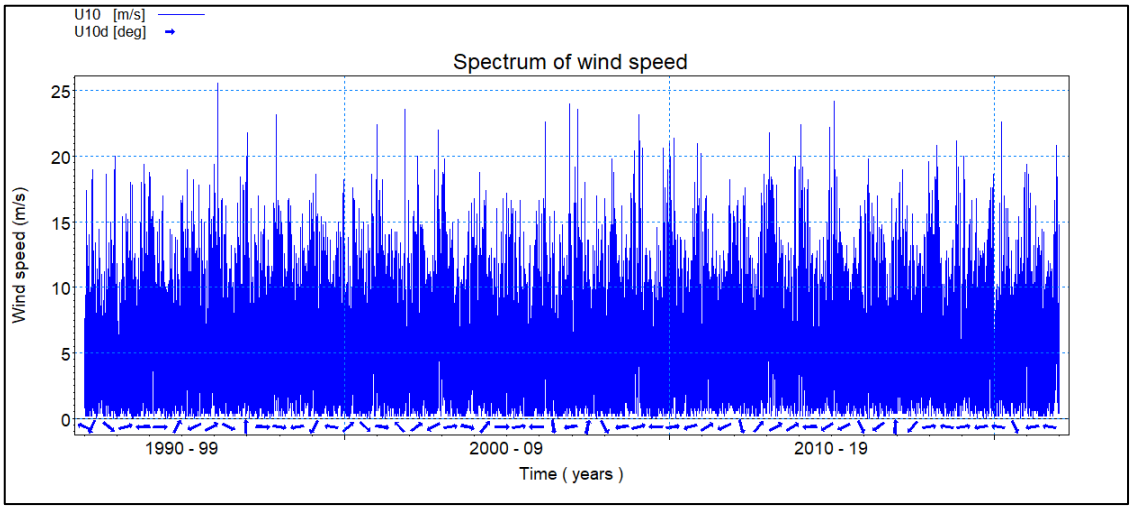

Figure I-9 Representation of the spectrum of recorded wind speed.

Statistical analysis of offshore wind speed allowed us to define some values represented in Table I-5

Table I-5 Wind speed.

Wave heights		Value (m)
V_m	Average height	5.53
V_s	Average of the top 1/3 of the record	9.35
V_{min}	Minimum value of the record	0.20
V_{max}	Maximum value of the record	25.60

The database of the study area allowed us to determine the plots annual and seasonal wind roses and the frequency of wind occurrence by direction represented in Table I-6.

Table I-6 Annual and seasonal occurrence of offshore winds by direction.

	Annual (%)	Winter (%)	Spring (%)	Summer (%)	Autumn (%)
N (0°)	5.80	5.25	5.94	6.72	5.55
NE (45°)	15.07	7.49	15.26	24.95	13.08
E (90°)	21.67	11.84	21.25	33.86	20.53
SE (135°)	7.13	7.05	7.52	6.29	8.01
S (180°)	8.04	11.99	6.95	4.28	9.41
SW (225°)	14.09	20.59	14.72	6.19	15.63
W (270°)	19.37	27.20	20.03	10.69	20.59
NW (315°)	7.70	8.58	8.34	7.02	7.21

From the annual wind rose, illustrated in Figure I-10, we can clearly observe the dominance of two directions: East and West, which account for nearly 40% of all winds blowing off Algiers Bay. The highest peak speed recorded reach more than 25,6 m/s from the West sector.

- East direction: This wind direction represents approximately 21% of the annual time. Interestingly, it exhibits a higher frequency of occurrence during summer (33%) compared to winter (11%). This indicates that during the summer months, there is a greater likelihood of winds blowing from the East.
- West direction: Constituting around 19% of the annual duration, the West direction shows a higher frequency of occurrence in winter (27%) compared to summer (10%). Thus, during winter, there is a heightened probability of winds originating from the West.

Furthermore, an examination of the monthly wind roses (Figure I-11) uncovers additional insights:

- Calm winds: During the summer months, wind speeds do not exceed 18 m/s.
- Stronger winds: In contrast, the winter months experience more vigorous winds, with speeds exceeding 18 m/s.

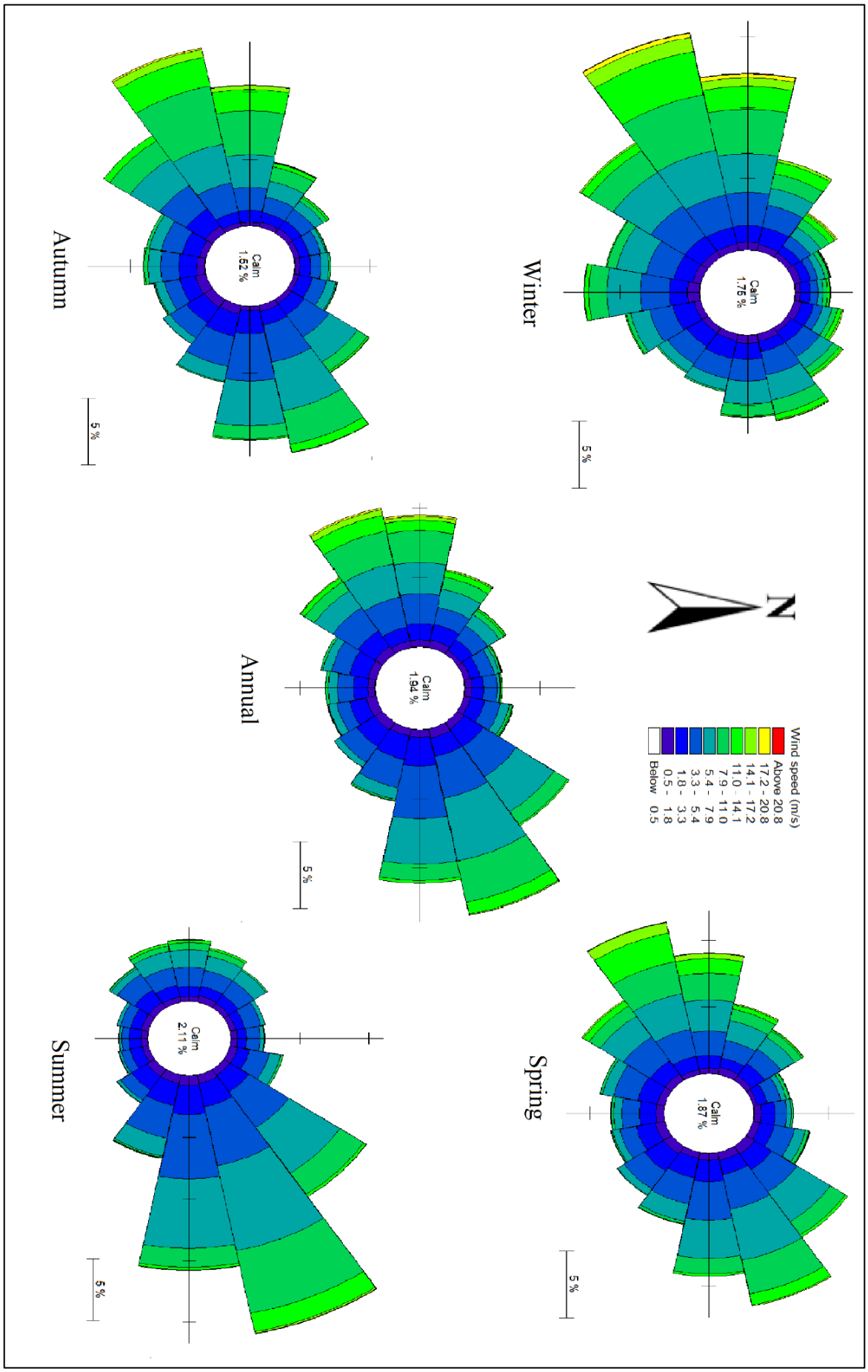

Figure I-10 Annual and seasonal wind roses recorded from 1992 - 2021 at 37° N and 3° E.

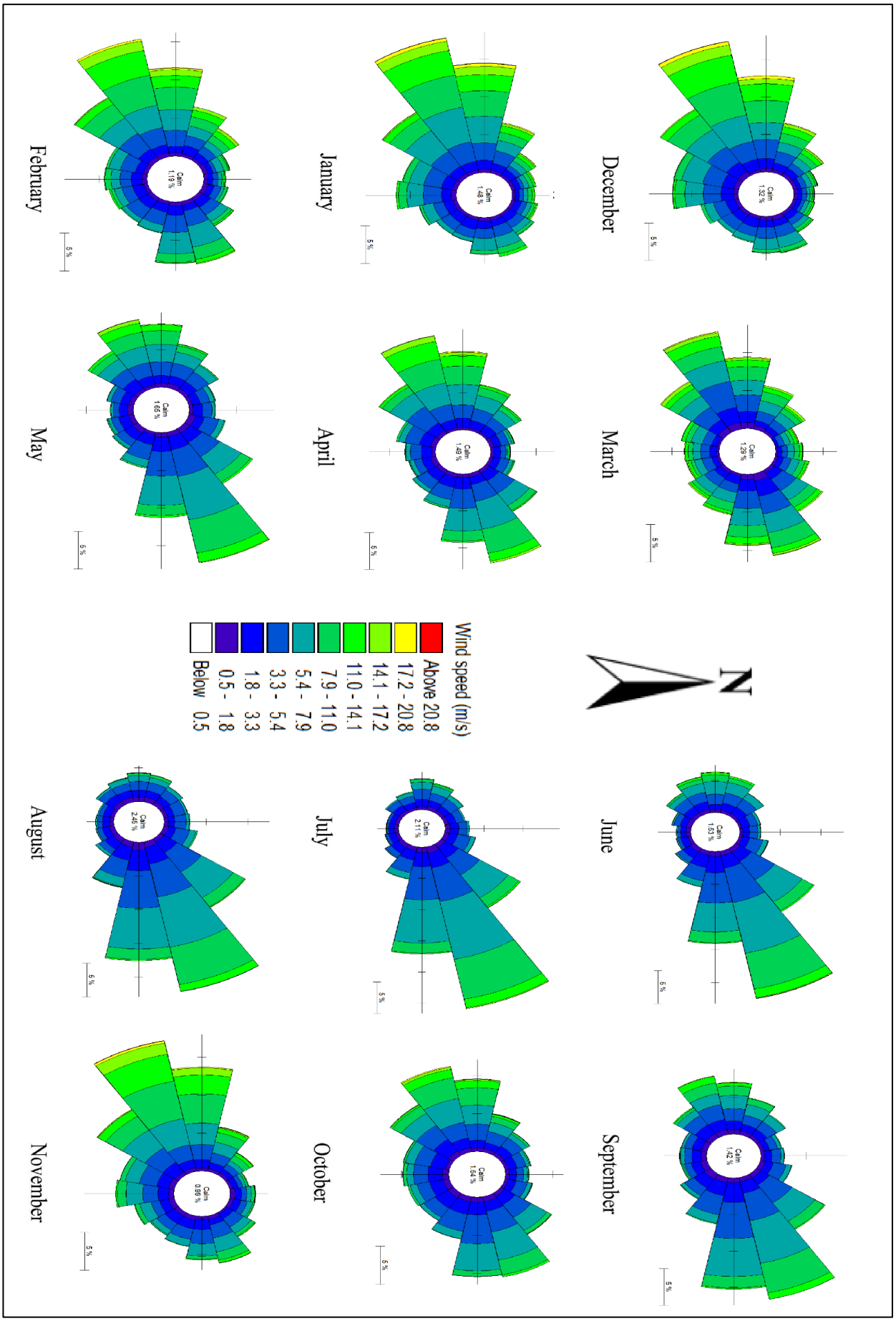

Figure I-11 Monthly wave roses recorded from 1992 - 2021 at 37° N and 3° E.

I.5. Conclusion

In conclusion, the wind and wave climate analysis conducted for Algiers Bay provides valuable insights into the environmental conditions of the area.

The wave climate analysis shows that the significant wave height in Algiers Bay ranges from 0.03m to 7.48m, with an average of 1.16m over a 30-year period. Most waves are smaller than 4m, but extreme values exceeding 5m occur every 4-6 years. The dominant wave directions are from the North-East and West, with North-East winds prevailing during summer and West winds more frequent in winter.

The wind climate analysis reveals that wind speed in Algiers Bay varies from 0.2m/s to 25.6m/s, with the highest density of wind speeds between 0.2m/s and 15m/s. The dominant wind directions are East and West, with East winds more prevalent in summer and West winds more frequent in winter.

Understanding the wind and wave climate is crucial for designing effective coastal protection measures.

Chapter II. Extreme events

II.1. Introduction

Coastal zones are subject to storm events with associated extreme waves. Various parameters are of interest, but in this study, emphasis is put on the return periods and their extreme waves, which are important in the design of coastal defense structures such as seawalls and breakwaters. This is done in order to provide sufficient protection against flooding or erosion to a desired return level associated with a particular return period, for example 100 years (Thompson et al. 2009). Under or over design can lead to very costly consequences and even fatalities. Proper statistical analyses of measured wave data of a time series are therefore required for these estimations.

To achieve convincing results, we have opted to work, in this chapter with the theory of extreme values.

II.2. Extreme value theory

Extreme value theory provides a framework that enables extrapolation in order to estimate the probability of events that are more extreme than any that have already been observed (Coles 2001). In other words, it is used to determine bounds by estimating statistical models that fit the extreme values of the observed data (Cornel Stander, 2015).

Although there are various statistical approaches for analyzing extreme values, they are typically divided into two main categories: methods that consider maxima over fixed intervals (block maxima approach) and methods that consider exceedances (peaks) above high thresholds based on exceedances over a chosen threshold (u) is called the Points Over Threshold (POT) method (Jacob, Neves, & Greetham, 2020).

These methods are illustrated in Figure II-1 (Cornel Stander, 2015) where the block maxima approach is illustrated in the graph on the left and the POT approach is illustrated in the graph on the right. The red dots indicate the values to be used for analysis. The block maxima (BM) approach in extreme value theory (EVT) involves dividing the observation period into non-overlapping periods of equal size and focusing on the maximum observation in each period.

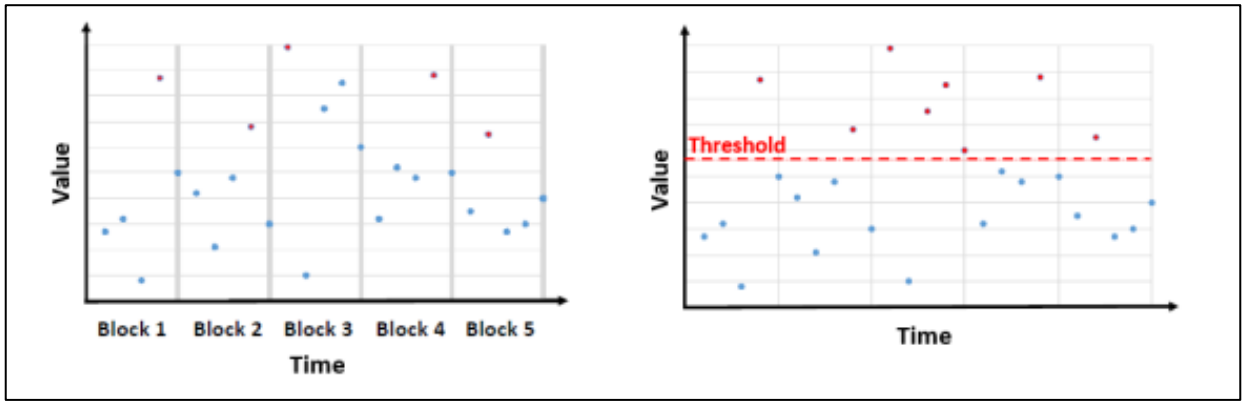

Figure II-1 Representative schema of the block maxima and POT methods.

II.2.1. Block maxima method

Let $X_1, X_2, \cdots, X_n$ be a sequence of independent distributed random variables, where X_i, $i = 1 \ldots, n$ has some unknown distribution function F. Define $Mn = max\{X_1, X_2, \cdots, X_n\}$, i.e., M_n is the block maxima. The objective is now to find the distribution of M_n. Since X has distribution function F (Andersson, K. 2020), we could argue that:

$$\begin{aligned} \Pr(M_n \leq x) &= \Pr(X_1 \leq x, X_2 \leq x, \ldots, X_n \leq x) \\ &= \Pr(X_1 \leq x)\Pr(X_2 \leq x) \ldots \Pr(X_n \leq x) \\ &= (F(x))^n, \end{aligned}$$

Equation II-1

This is insufficient since F is unknown, (Coles, 2001). Fortunately, the Fisher-Tippet theorem can be employed in this case. This theorem states that as n approaches infinity, M_n converges in distribution to the generalized extreme value (GEV) family of distributions (Andersson, K. 2020). These distributions are defined in the Equation II-2

$$H_{\mu,\sigma,\xi}(x) = \begin{cases} \exp\left(-\left(1+\xi\dfrac{x-\mu}{\sigma}\right)^{-\frac{1}{\xi}}\right) & \xi \neq 0 \\ \exp\left(-\exp\left(\dfrac{x-\mu}{\sigma}\right)\right) & \xi = 0, \end{cases}$$

Equation II-2

Provided that $1 + \xi(x - \mu) = \sigma > 0$. The three parameters μ, σ and ξ are the location parameter, the scale parameter and the shape parameter respectively. μ indicates where on the axis the distribution of M_n is located and σ illustrate the width of the distribution. Finally, ξ is a measure of the shape of the distribution.

- $\xi > 0$, then M_n follows the Fréchet distribution, which is a distribution with heavy tails.
- $\xi = 0$, M_n follows the Gumbel distribution, which has exponential tails. For $\xi < 0$. The tails of this distribution are lighter than in the normal one.
- $\xi < 0$, the distribution has an upper end-point; $\mu - \sigma = \xi$

$\xi > 0$ and $\xi = 0$ are of most interest, since this sort of data rarely have tails lighter than normal (Coles, 2001).

The Generalized Extreme Value (GEV) distribution is commonly used in the field of coastal engineering to estimate the probability of extreme events, such as storm surges, waves, and sea level rise. Two popular methods for estimating return periods using the GEV distribution are the Gumbel and Weibull methods.

In this study, the data analysis process was conducted using the Python programming language, with the help of the Pyextreme library. It offers an efficient and effective way to analyze data. The output of the analysis was presented in the form of graphs and tables, which provided a visual representation of the findings.

The estimation of the data block was carried out by considering a period of one year. The Figure II-2 illustrate data in the form of blue lines and red points, allowing for the identification of the maximum value of each year to be taken separately. Once the maximums have been selected for each year, we go directly to the calculation of the wave height return values to each return period.

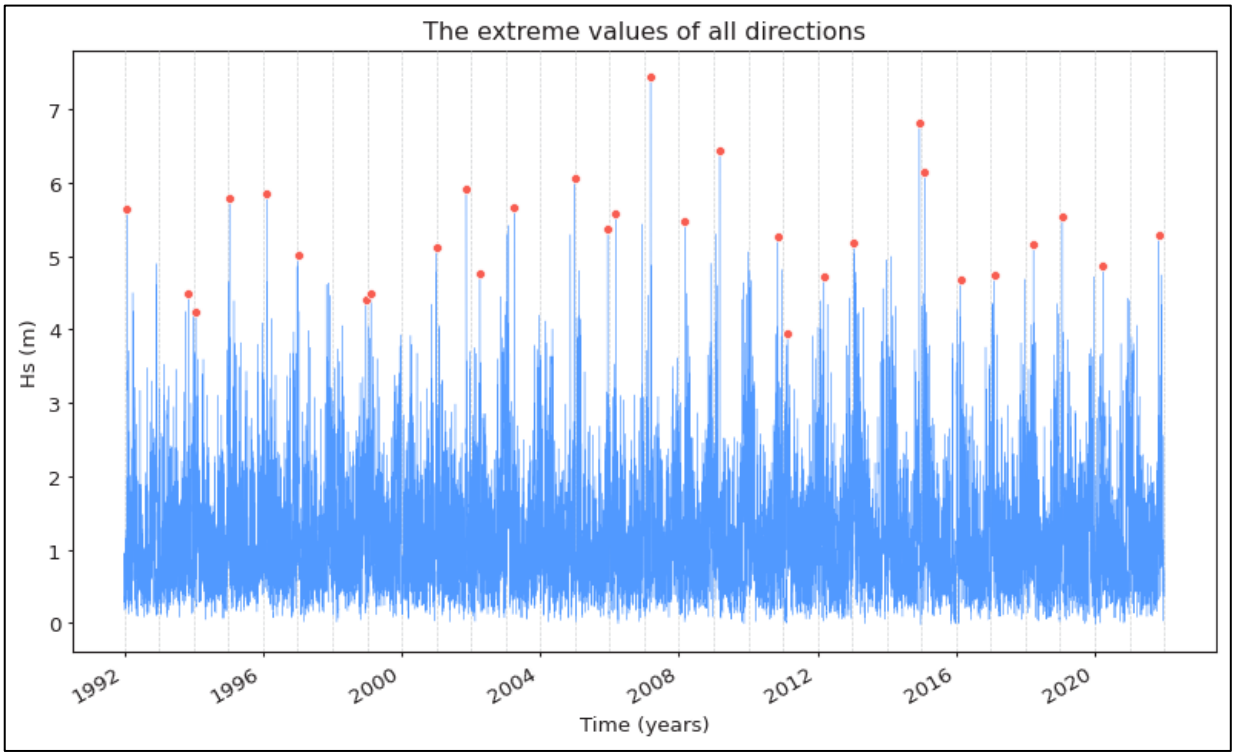

Figure II-2 Representation of Maximum Blocks method on 1992 - 2021 wave heights.

Gumbel and Weibull distribution Results

The Gumbel distribution (Equation II-3) is used to model the maximum values of a random variable, such as the maximum wave height. This distribution is characterized by two parameters, the location parameter (μ) and the scale parameter (σ).

$$F(x;\mu,\sigma) = e^{-e^{-(x-\mu)/\sigma}}$$ **Equation II-3**

The Weibull method (Equation II-4) is another commonly used distribution for modeling extreme events. This distribution is characterized by two parameters, the shape parameter (k) and the scale parameter (λ).

$$F(x;k,\lambda) = 1 - e^{[-\left(\frac{x}{\lambda}\right)^{k}]}$$ **Equation II-4**

The findings of this study are presented in Figure II-3 & Figure II-4, where blue and red lines are used to represent the limits of the accepted error, set at 15% for the results. The red crosses in the graph indicate the values of wave heights for specific return periods, including 2, 5, 10, 20, 30, 50, 100,500 and 1000 years.

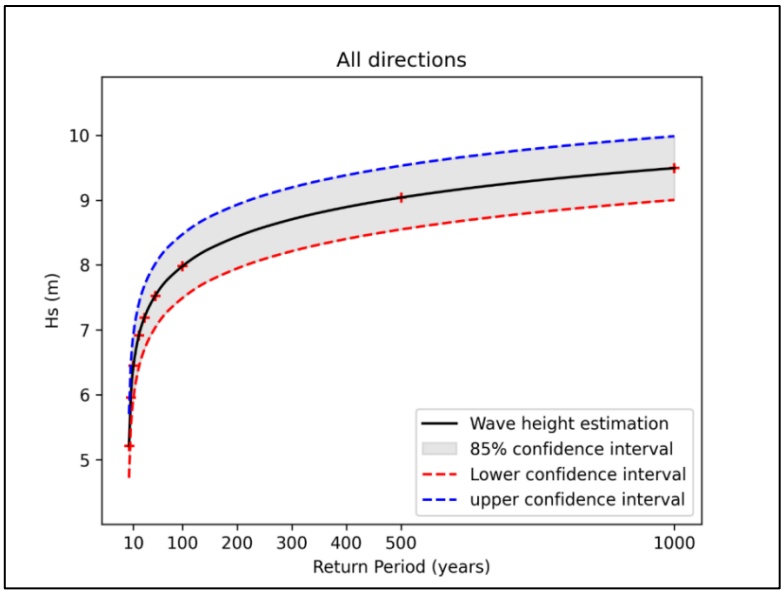

Figure II-3 Estimation of extreme events via the Gumbel distribution for omnidirectional.

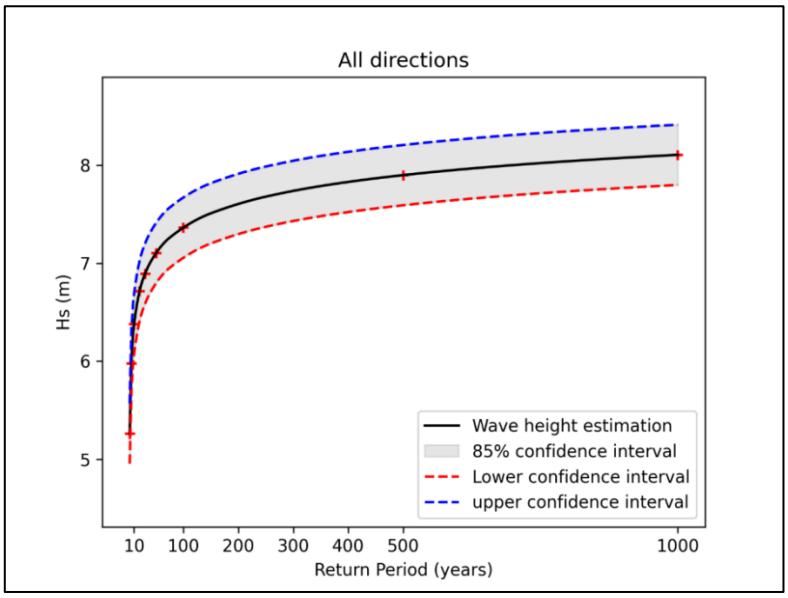

Figure II-4 Estimation of extreme events via the Weibull distribution for omnidirectional.

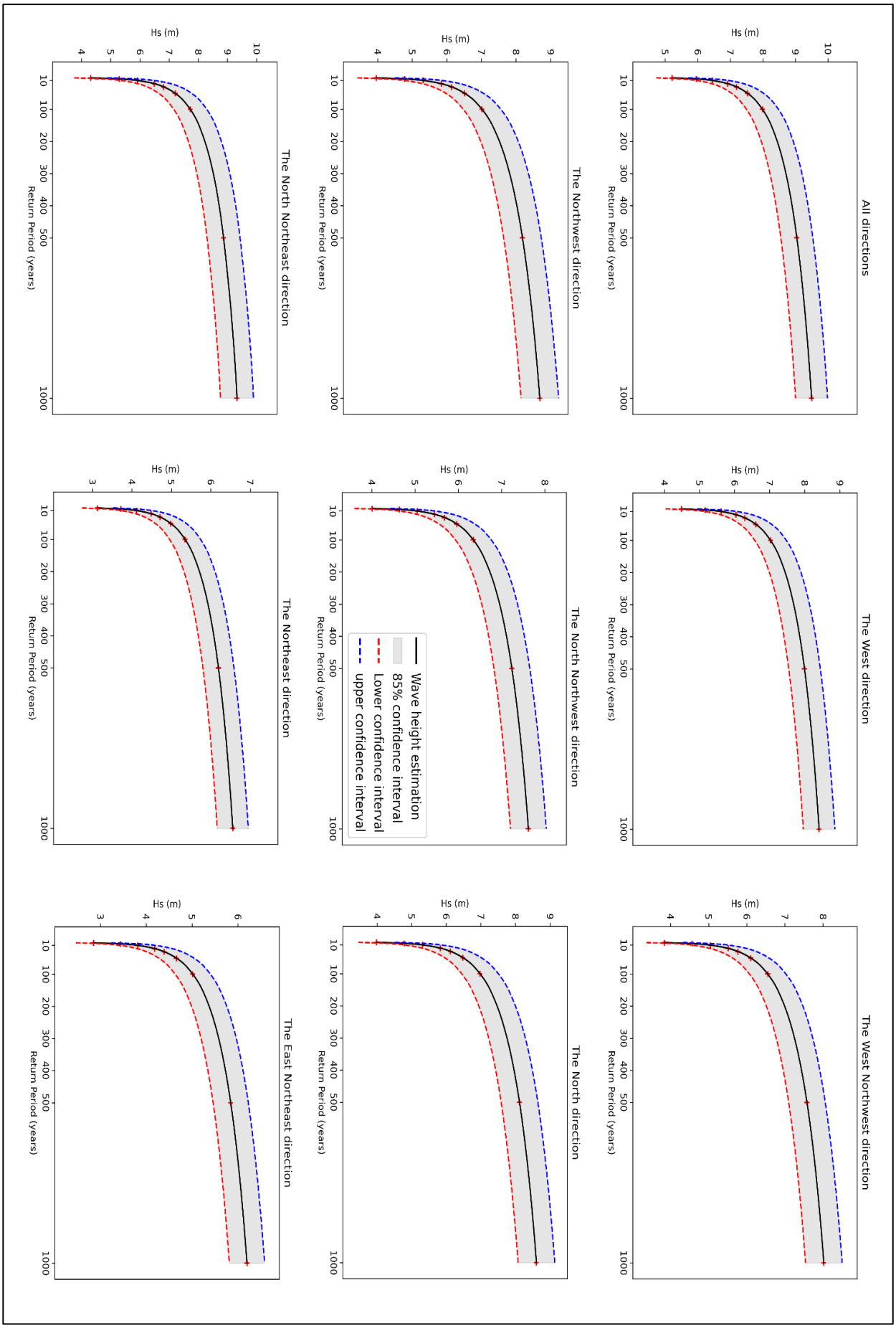

Figure II-5 Estimation of extreme events via the Gumbel distribution for each direction.

To facilitate the interpretation of the results obtained through the use of the Gumbel distribution, a table has been created to summarize the set of extreme heights obtained based on the return periods of these extreme events in the future.

Table II-1 summarizing all the results obtained by the GEV method according to the Gumbel distribution.

GEV - Gumbel distribution									
Return period (years)	**Wave height by direction (meter)**								
	W	**WNW**	**NW**	**NNW**	**N**	**NNE**	**NE**	**ENE**	**Omni**
2	4.48	3.84	3.95	4.01	3.98	4.31	3.12	2.85	5.21
5	5.16	4.56	4.77	4.63	4.78	5.29	3.72	3.43	5.96
10	5.61	5.04	5.31	5.05	5.31	5.91	4.11	3.81	6.45
20	6.04	5.50	5.83	5.44	5.82	6.49	4.49	4.18	6.92
30	6.29	5.77	6.13	5.67	6.11	6.81	4.71	4.39	7.19
50	6.60	6.10	6.51	5.96	6.48	7.20	4.98	4.66	7.53
100	7.02	6.54	7.01	6.34	6.97	7.72	5.34	5.01	7.98
500	7.99	7.58	8.18	7.23	8.11	8.86	6.19	5.84	9.04
1000	8.41	8.02	8.68	7.62	8.60	9.32	6.55	6.19	9.49

Table II-1 presents the results obtained from the analysis conducted using the Gumbel distribution for predicting wave heights. The numerical values within the table provide valuable insights into the likelihood of extreme wave events in different directions.

The findings reveal that the East Northeast (ENE) direction exhibits relatively lower wave heights compared to other directions.

Conversely, the North, North Northeast, Northwest and West directions are more likely to generate higher wave heights. For instance, at a 1000-year return period, the wave heights recorded in these directions are as follows: North (N) at 8.60 meters, North Northeast (NNE) at 9.32 meters, Northwest (NW) at 8.68 meters and West (W) at 8.41 meters. These demonstrate that these directions have a greater tendence for extreme wave events.

Of particular interest is the observation that the North Northeast (NNE) direction exhibits the highest predicted wave height within the dataset. At a 1000-year return period, wave heights in the NNE direction reach 9.32 meters, suggesting a heightened risk of extreme wave events originating from this direction.

In contrast to the directional analysis, the analysis of omnidirectional heights yields the highest results, as the model simulates the maximum heights that can exist within the dataset. At a 2-year return period, wave heights in the Omni direction reach 5.21 meters, and for the 1000-year return period, wave heights reach 9.49 meters.

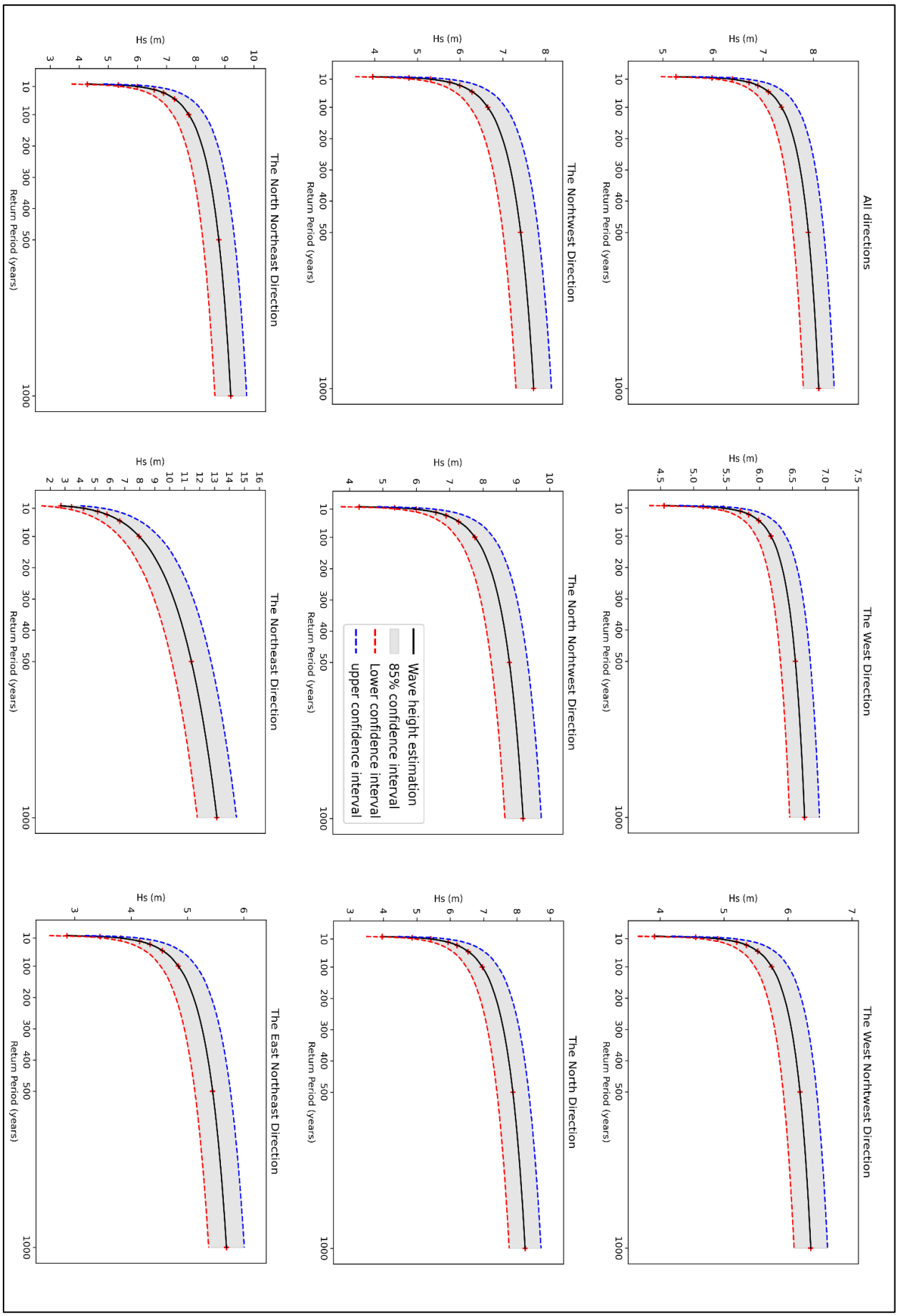

Figure II-6 Estimation of extreme events via the Weibull distribution for each direction.

To facilitate the interpretation of the results obtained through the use of the Weibull distribution, a table has been created to summarize the set of extreme heights obtained based on the return periods of these extreme events in the future.

Table II-2 summarizing all the results obtained by the GEV method according to the Weibull distribution.

GEV - Weibull distribution									
Return period (years)	**Return period (years)**								
	W	**WNW**	**NW**	**NNW**	**N**	**NNE**	**NE**	**ENE**	**Omni**
2	4.55	3.91	3.95	4.03	3.96	4.28	2.71	2.86	5.26
5	5.14	4.55	4.80	4.64	4.86	5.34	3.44	3.45	5.98
10	5.45	4.90	5.30	4.99	5.42	5.99	4.22	3.81	6.38
20	5.70	5.19	5.75	5.29	5.92	6.58	5.17	4.15	6.71
30	5.83	5.35	5.99	5.45	6.20	6.89	5.80	4.33	6.89
50	5.99	5.52	6.28	5.64	6.53	7.27	6.66	4.55	7.10
100	6.17	5.74	6.64	5.88	6.96	7.76	7.95	4.84	7.36
500	6.54	6.18	7.41	6.38	7.87	8.79	11.44	5.45	7.90
1000	6.68	6.35	7.72	6.58	8.24	9.20	13.15	5.69	8.11

Table II-2 provides a summary of the results obtained from the analysis conducted using the Weibull distribution to predict wave heights. These findings offer insights into the characteristics of extreme wave events in various directions.

The findings indicate that the East north east direction is the least likely to generate extreme wave heights. For example, at a 1000-year return period, the wave height in the ENE direction is recorded as 5.69 meters, which is the lowest value among all directions in that return period.

Analyzing the directional wave heights, it is observed that the Northeast (NE) direction is the most likely to generate the highest waves, followed by the North Northeast (NNW), North (N), and Northwest (NW) directions. For instance, at a 1000-year return period, the wave heights in these directions are as follows:

- Northeast (NE): 13.15 meters
- North Northeast (NNW): 9.20 meters
- North (N): 8.24 meters
- Northwest (NW): 7.72 meters

However, it is worth noting that the analysis of omnidirectional wave heights yields even higher results. The omnidirectional analysis considers the maximum heights that can be present in the dataset. Yet, there were some anomalies observed regarding the estimated heights in the North, North East, and North East directions, which exceeded those estimated in the omnidirectional case. This raises doubts about the suitability of the Weibull distribution for accurately modeling these specific directional patterns.

To determine which distribution is most appropriate for our data, we fit both distributions (Gumbel or Weibull) to our data and compare the goodness of fit. The goodness of fit can be evaluated using graphical methods such as the probability plot.

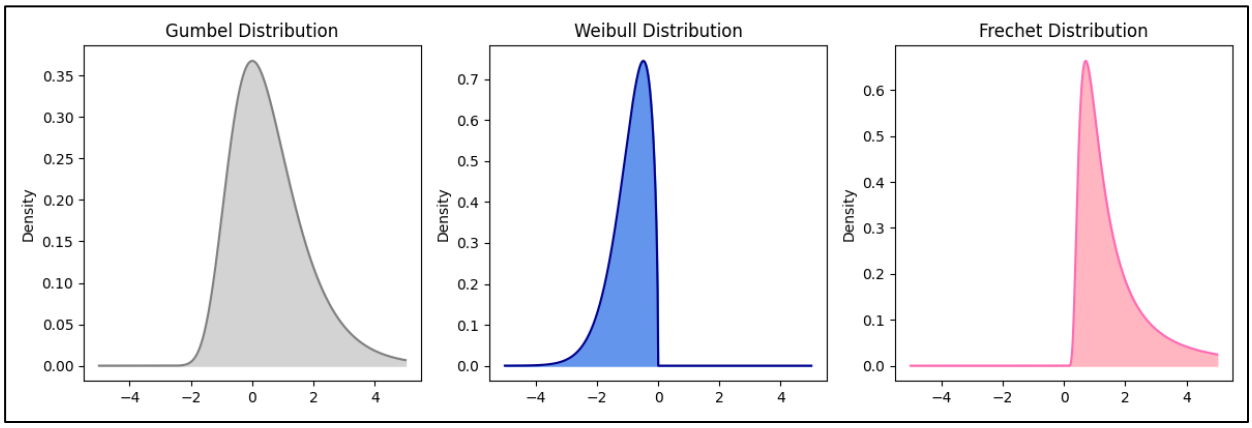

Figure II-7 Representation of the possible distributions of the GEV method.

In order to graphically represent the real distribution of our wave height data, we use a script in the python language of the seaborn library (Figure II-8)

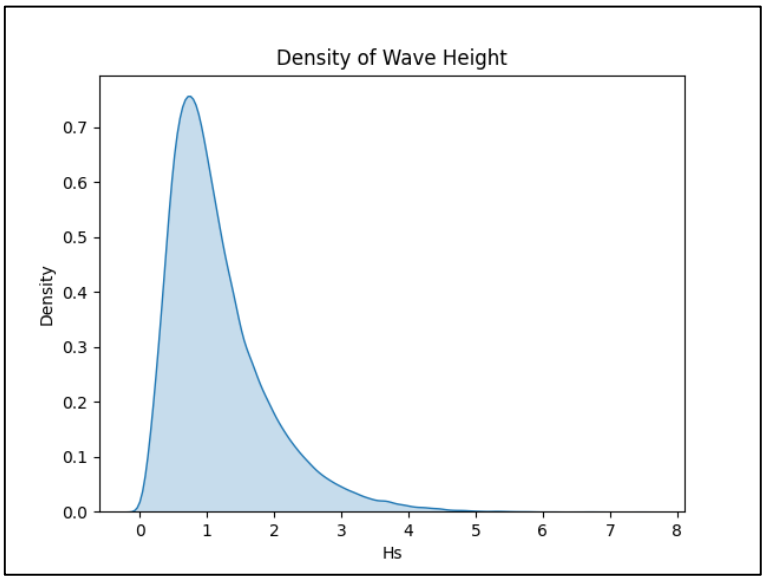

Figure II-8 Graphical representation of the wave height distribution.

To proceed to the second method (POT), we will opt for the results obtained with the Gumbel distribution. On the other hand, we neglect the results obtained with the Weibull distribution because our data graph Figure II-8 is similar to the one of Gumbel in the Figure II-7.

II.2.2. Peaks over Threshold Method (POT)

Let X_1, X_2,⋯,$X_n$be a sequence of random variables that are independent and identically distributed with some unknown distribution function F. Then, the POT method can be summarized as that we want to find the distribution of all excess observations that are greater than some chosen threshold u. Denote this distribution by $F_u(x)$. Thus, we have:

$$F_u(x) = \Pr(X - u \leq x) \mid X > u) = \frac{F(u+x) - F(u)}{1 - F(u)}. \qquad \textbf{Equation II-5}$$

Threshold selection

The choice of the threshold is not straightforward; we can determine the ideal threshold by visually inspecting the plot of the mean residual, The threshold should be on the straight line before the variations of the mean residual. The choice of the threshold, it is carried on the value 3.42 m (Figure II-9).

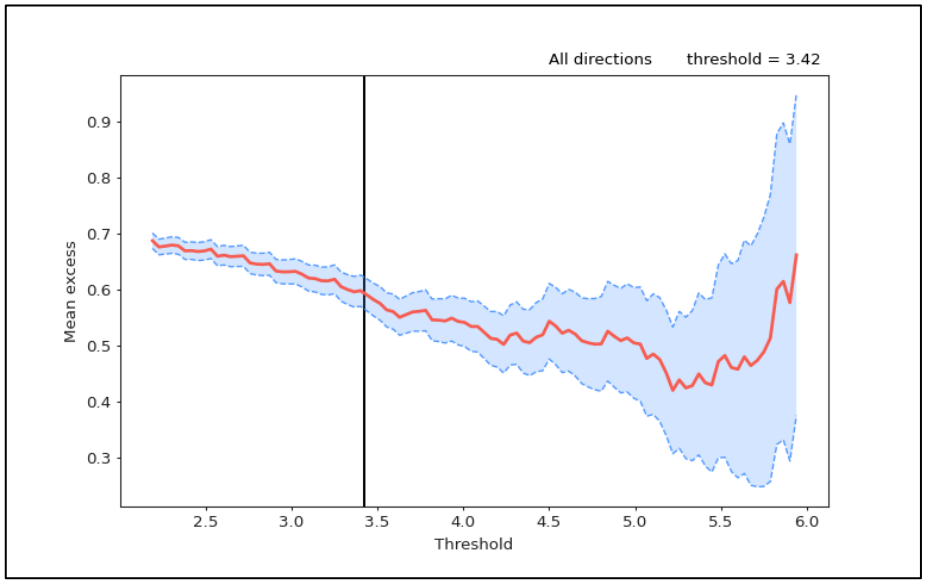

Figure II-9 Residual mean of the omnidirectional wave height of the record.

After determining the threshold for the peak over threshold (POT) method, the next step is to estimate the distribution of extreme values that exceed the threshold (Figure II-10).

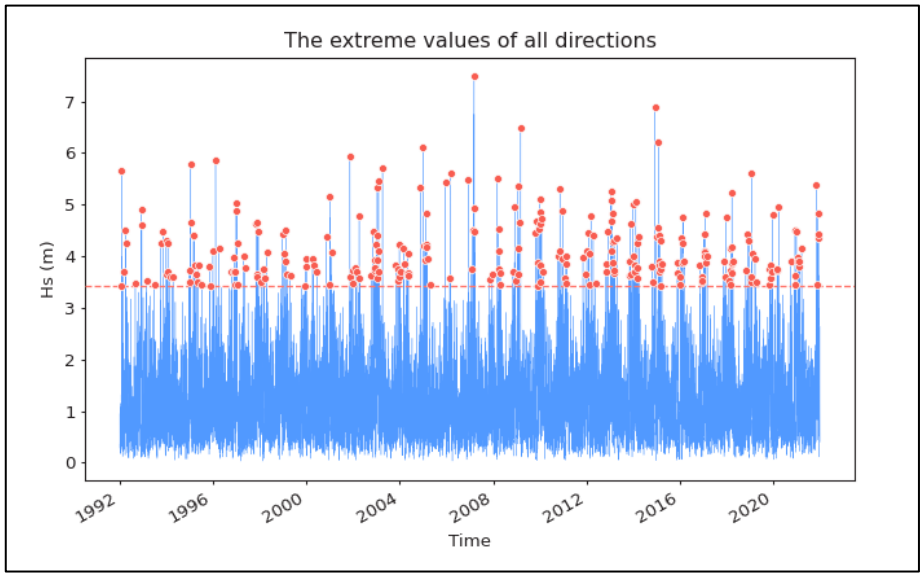

Figure II-10 Representation of POT method on wave heights data from 1992 - 2021.

After the selection of the peaks, we calculate the wave heights with their return periods via the same library pyextreme on the python language. We obtain the following results following results:

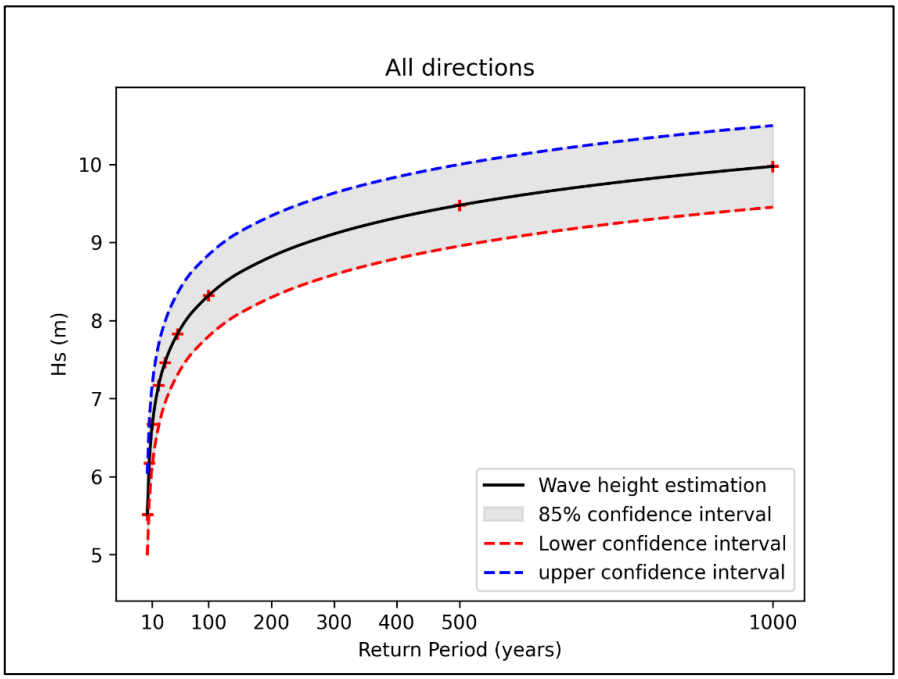

Figure II-11 Estimation of extreme events via the POT method for omnidirectional.

The findings of this study are presented in Figure II-13, where blue and red lines are used to represent the limits of the accepted error, set at 15% for the results. The red crosses in the graph indicate the values of wave heights for specific return periods, including 2, 5, 10, 20, 30, 50, 100,500 and 1000 years.

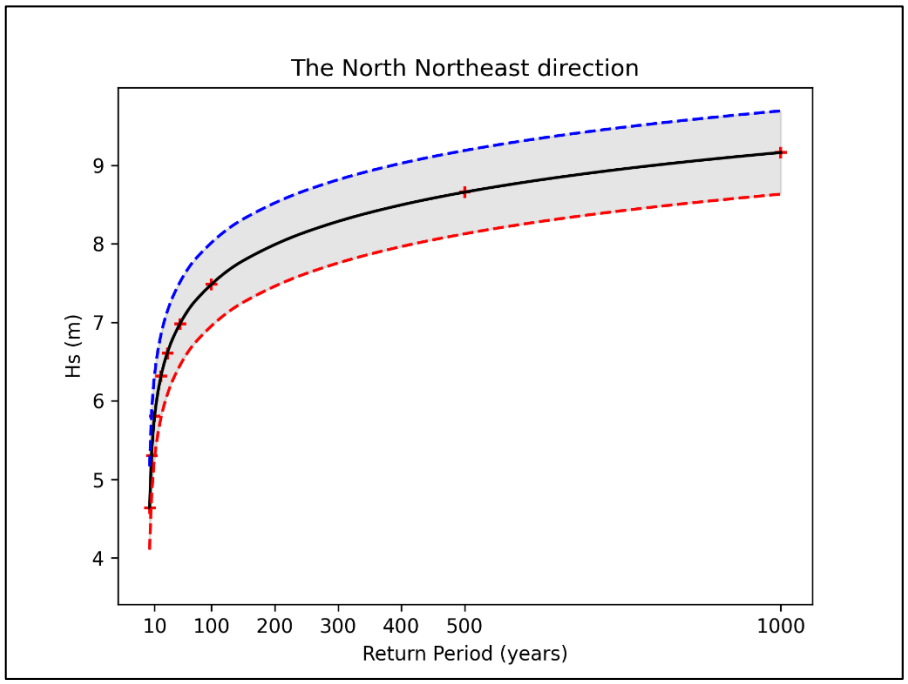

Figure II-12 Estimation of extreme events via the POT method for North Northeast direction.

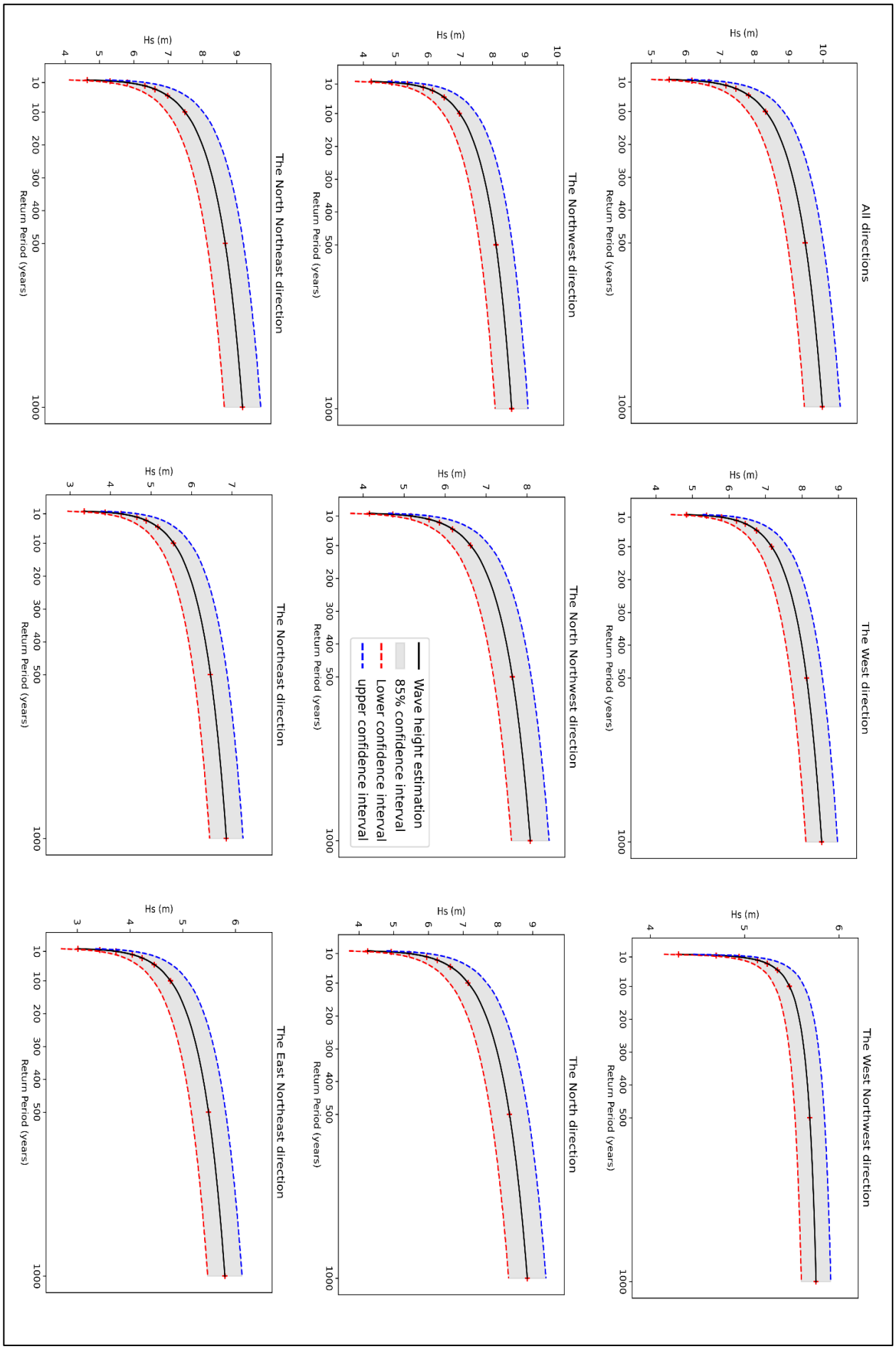

Figure II-13 Estimation of extreme events via the POT method for each direction.

To facilitate the interpretation of the results obtained through the use of the peak over threshold (POT) method, a table has been created to summarize the set of extreme heights obtained based on the return periods of these extreme events in the future.

Table II-3 summarizing all the results obtained by the peak over threshold (POT) method

The peak over threshold (POT) method									
Return period (years)	**Return period (years)**								
	W	**WNW**	**NW**	**NNW**	**N**	**NNE**	**NE**	**ENE**	**Omni**
2	4.83	4.30	4.24	4.15	4.25	4.64	3.34	3.01	5.51
5	5.38	4.70	4.88	4.73	4.93	5.30	3.86	3.42	6.17
10	5.79	4.94	5.36	5.16	5.44	5.81	4.25	3.73	6.67
20	6.21	5.14	5.85	5.60	5.95	6.31	4.64	4.04	7.17
30	6.45	5.24	6.13	5.86	6.25	6.61	4.87	4.22	7.46
50	6.75	5.35	6.49	6.18	6.63	6.98	5.16	4.45	7.82
100	7.16	5.47	6.97	6.62	7.14	7.49	5.56	4.76	8.32
500	8.12	5.69	8.10	7.64	8.33	8.66	6.47	5.48	9.48
1000	8.54	5.75	8.58	8.08	8.85	9.16	6.86	5.79	9.97

Table II-3 presents the results obtained by the peak over threshold (POT) method for predicting wave heights. The table provides insights into the likelihood of extreme wave events in different directions based on the return periods.

The findings indicate that the East north east direction is the least likely to generate extreme waves heights. For example, at a 1000-year return period, the wave height in the ENE direction is recorded at 5.79 meters, which is the lowest value among all directions for that return period.

In contrast, the North Northeast (NNE), North (N), Northwest (NW), and West (W) directions are more likely to generate higher wave heights. For instance, at a 1000-year return period, the wave heights recorded in these directions are as follows: NNE at 9.16 meters, N at 8.85 meters, NW at 8.58 meters, and W at 8.54 meters. These indicate a higher propensity for extreme wave events in these directions.

Of particular interest is the observation that the North Northeast (NNE) direction. The analysis suggests that extreme waves are more likely to originate from this direction compared to others. At a 1000-year return period, wave heights in the NNE direction reach 9.16 meters.

Diverging from the analysis of wave heights in individual directions, the examination of omnidirectional wave heights reveals the most significant outcomes. By considering the maximum wave heights attainable within the dataset, the omnidirectional analysis unveils the highest values. For instance, at a return period of 1000 years, the wave height in the omnidirectional direction reaches an impressive 9.97 meters, surpassing all other directions and demonstrating the potential for extreme wave events in any direction.

II.3. Comparison between Peak Over Threshold and Block Maxima

Our goal was to obtain more accurate and efficient results in our analysis of extreme events, so we worked with both the POT and GEV methods. After implementing each method, we then proceeded to compare the results of the two approaches.

In this section, our focus will be on working with the omnidirectional in order to select the most appropriate approach for our analysis of hydraulic performance for extreme conditions in the hydraulic performance chapter.

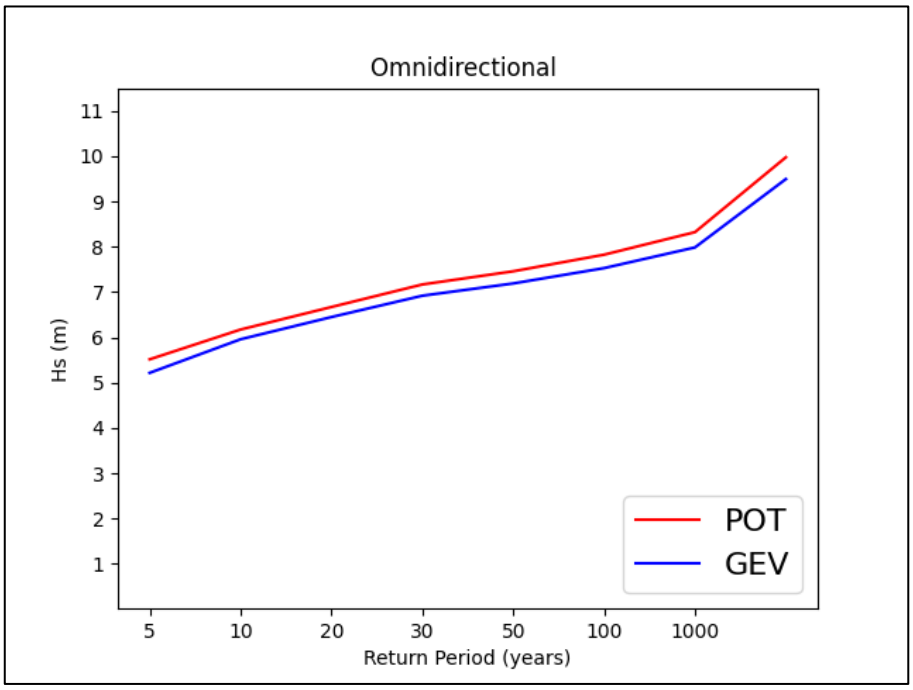

Figure II-14 Comparison of the results obtained with the two methods POT and GEV.

From Figure II-14, we can see that the two methods have almost the same results Also, we can see that the POT method proposes higher values than the GEV method for all the return periods. Because the POT method can capture more extreme events since it considers all events above a certain threshold, while the block maxima method only considers the maximum value within each block Both the choice of threshold and block size can also impact the results of the two methods.

II.4. Conclusion

Analyzing extreme events has allowed us to understand the likelihood of rare marine phenomena and create models that represent their probability distributions. This knowledge is crucial for designing reliable coastal defense structures and mitigating the impact of these events. Nevertheless, it is imperative to enhance estimation and modeling techniques to enhance our ability to predict the risks linked to extreme events more accurately.

Chapter III. Numerical Modeling

III.1. Introduction

In order to model marine, coastal, and estuarine areas, a diverse range of digital modeling software options exist. These models have been developed by universities, research institutions, and private companies. While certain models have been made commercially available, others are primarily intended for academic research purposes (Symonds et al., 2017).

The DHI Mike 21 model was chosen for the wave simulations in this study.

III.2. Presentation of the model

DHI MIKE 21 is a numerical model widely used to simulate ocean wave propagation in offshore and coastal environments. Developed by the Danish Hydraulic Institute, the model is based on the spectral density conservation method, which allows it to accurately capture the complex interactions between wave energy and the environment. MIKE 21 includes features such as wave refraction, and shoaling related to bathymetry variations, wave generation and dissipation, and can be used to simulate a wide range of wave conditions and scenarios. To use MIKE 21 for wave simulation, a mesh must first be generated using the Mesh Generator tool within the MIKE software suite. The mesh is typically composed of triangular elements in the horizontal plane, which can be refined in areas of interest to increase resolution.

III.2.1. Mesh Generator

The Mesh Generator is an advanced tool that provides a workspace for creating detailed digital meshes for use in Mike zero flexible mesh (FM) models. It is critical to provide these new generation models with a suitable mesh in order to obtain reliable results from model simulations.

III.2.2. MIKE SW

MIKE SW is an advanced numerical modeling software specifically designed for simulating wave propagation in shallow water environments. By incorporating various physical phenomena, including wave refraction, shoaling, wind-generated wave generation, frictional dissipation, breaking, and wave-current interaction, the software provides accurate predictions of wave

characteristics. With its flexible non-structured mesh grid, MIKE 21 SW offers precise calculations and considers dissipations due to wave breaking and nonlinear interactions.

The model typically necessitates the following inputs:

- Digitized bathymetry: Essential model parameters that outline the model's scope, such as the dimensions of the modeled area, the grid spacing on the computational grid, the time step, and the simulation duration.
- Boundary conditions: The model requires a spectral formulation as an initial condition, along with specific wave parameters (Significant wave height (H_s), Peak period (T_p), Wave direction, and Directional spreading) that need to be provided for all open boundaries.

Shallow water equations

MIKE SW employs a computational approach that solves the Reynolds-averaged Navier-Stokes equations, which describe the motion of incompressible fluids in three dimensions. The model is designed to simulate shallow water flow, using the assumptions of Boussinesq and hydrostatic pressure. In particular, the model solves the continuity equation to ensure that mass is conserved, which is given by:

$$\frac{\partial u}{\partial x}+\frac{\partial v}{\partial y}+\frac{\partial w}{\partial z}=S \qquad \textbf{Equation III-1}$$

And the two horizontal momentum equations for the x and y components can be expressed as follows

$$\frac{\partial u}{\partial t}+\frac{\partial u^2}{\partial x}+\frac{\partial \eta p}{\partial y}+\frac{\partial wu}{\partial z}=fv-g\frac{\partial \eta}{\partial x}-\frac{1}{\rho_0}\frac{\partial p_a}{\partial x}-\frac{g}{\rho_0}\int_z^{\eta}\frac{\partial \rho}{\partial x}dz-\frac{1}{\rho_0 h}\left(\frac{\partial s_{xx}}{\partial x}+\frac{\partial s_{xy}}{\partial y}\right)+F_u+\frac{\partial}{\partial z}\left(v_t\frac{\partial u}{\partial z}\right)+u_sS \qquad \textbf{Equation III-2}$$

$$\frac{\partial v}{\partial t}+\frac{\partial v^2}{\partial y}+\frac{\partial uv}{\partial x}+\frac{\partial wv}{\partial z}=-fu-g\frac{\partial \eta}{\partial y}-\frac{1}{\rho_0}\frac{\partial p_a}{\partial y}-\frac{g}{\rho_0}\int_z^{\eta}\frac{\partial \rho}{\partial y}dz-\frac{1}{\rho_0 h}\left(\frac{\partial s_{yx}}{\partial x}+\frac{\partial s_{yy}}{\partial y}\right)+F_v+\frac{\partial}{\partial z}\left(v_t\frac{\partial v}{\partial z}\right)+v_sS \qquad \textbf{Equation III-3}$$

Table III-1 Symbols and Significations in Continuity and Momentum Equations.

Symbol	Signification	Symbol	Signification
t	Time.	**A**	Horizontal viscosity.
Pa	Atmospheric pressure.	**g**	Gravity acceleration.
x. y , z	Cartesian coordinates.	$\boldsymbol{\rho_w}$	Water density.
η	Surface elevation.	$\boldsymbol{S_{xx}}$,$\boldsymbol{S_{xy}}$ $\boldsymbol{S_{yx}}$,$\boldsymbol{S_{yy}}$	Component of the radial tensor.
d	Water depth.	$\boldsymbol{\nu_t}$	Turbulent vertical viscosity.
h = η+d	Total water depth.	$\boldsymbol{\rho_0}$	The reference density of water.
u, v , w	Velocity components in the x, y, and z directions.	**S**	Amplitude of discharge caused by point sources.
$\boldsymbol{(u_s,v_s)}$	Velocity at which water is discharged into the ambient water.	**f = 2Ω sinΦ**	Coriolis parameter {Ω is the angular velocity and Φ is the geographical latitude}.
$\boldsymbol{(\tau_{sx}, \tau_{sy})}$	x and y components of surface wind stress.	$\boldsymbol{(\tau_{bx},\tau_{by})}$	x and y components of bottom wind stress.

The horizontal stress terms are described using a gradient-stress relationship, which is simplified as follows:

$$F_u = \frac{\partial}{\partial x}\left(2A\frac{\partial u}{\partial x}\right) + \frac{\partial}{\partial y}\left(A\left(\frac{\partial u}{\partial y} + \frac{\partial v}{\partial x}\right)\right)$$ **Equation III-4**

$$F_v = \frac{\partial}{\partial x}\left(A\left(\frac{\partial u}{\partial y} + \frac{\partial v}{\partial x}\right)\right) + \frac{\partial}{\partial y}\left(2A\frac{\partial v}{\partial y}\right)$$ **Equation III-5**

The surface and bottom boundary conditions for u, v, and w are as follows:

A $z = \eta$:

$$\frac{\partial \eta}{\partial t} + u\frac{\partial \eta}{\partial x} + v\frac{\partial \eta}{\partial y} - w = 0, \left(\frac{\partial u}{\partial z}, \frac{\partial v}{\partial z}\right) = \frac{1}{\rho_0 \nu_t}(\tau_{sx}, \tau_{sy})$$ **Equation III-6**

A $z = -d$:

$$u\frac{\partial d}{\partial x} + v\frac{\partial d}{\partial y} + w = 0, \left(\frac{\partial u}{\partial z}, \frac{\partial v}{\partial z}\right) = \frac{1}{\rho_0 \nu_t}(\tau_{bx}, \tau_{by})$$ **Equation III-7**

Equations of wave action conservation

The fundamental equation that describes wave action is the equilibrium equation, expressed in either Cartesian or spherical coordinates.

Cartesian coordinates

The equation of wave action conservation can be written as follows in horizontal Cartesian coordinates

$$\frac{\partial N}{\partial t} + \nabla \cdot (\vec{v}N) = \frac{S}{\sigma}$$ **Equation III-8**

Table III-2 Symbols and Significations in Wave Action Conservation Equation.

Symbol	Signification
N ($\vec{x}$, σ, θ, t)	Wave action density.
t	Time.
$\vec{x}$ = (x, y)	Cartesian coordinates.
σ	Wave action density.
S	Source term for the energy balance equation.
$\vec{v}$ (c_x,c_y,c_σ,c_θ)	Velocity of propagation of a wave group (in the four-dimensional phase space)
∇	Four-dimensional differential operator in the space : x, y, σ, θ.

The four characteristic propagation velocities are specified by the following formulas:

$$(c_x, c_y) = \frac{d\vec{x}}{dt} = \vec{c}_g + \vec{U}$$ **Equation III-9**

$$c_\sigma = \frac{d\sigma}{dt} = \frac{\partial \sigma}{\partial d}\left[\frac{\partial d}{\partial t} + \vec{U} \cdot \nabla_{\vec{x}} d\right] - c_g \vec{k} \cdot \frac{\partial \vec{U}}{\partial s}$$ **Equation III-10**

$$(c_x, c_y) = \frac{d\vec{x}}{dt} = \vec{c}_g + \vec{U}$$ **Equation III-11**

$$c_\theta = \frac{d\theta}{dt} = -\frac{1}{k}\left[\frac{\partial \sigma}{\partial d}\frac{\partial d}{\partial m} + \vec{k} \cdot \frac{\partial \vec{U}}{\partial m}\right]$$ **Equation III-12**

Table III-3 Symbols and Significations for Characteristic Propagation Velocities.

Symbol	Signification
S	Spatial coordinate in the direction of wave propagation θ.
m	Coordinate perpendicular to S.
$\overrightarrow{\nabla x}$	Two-dimensional differential operator in the space $\vec{x}$.

III.2.3. MIKE HD

MIKE HD is an advanced hydrodynamic module that enables users to define initial and boundary hydrographic conditions, incorporate bed resistance and wind forcing, and accommodate various sources, sinks, and structures. It solves the Saint-Venant equations while considering factors such as bottom friction, meteorological events, Coriolis force, turbulence modeling, and temporal variations in domain geometry. The module accurately predicts water flow patterns, velocities, and pressure distributions, and also calculates nearshore currents, accounting for wave radiation stresses in the surf zone. MIKE HD's flexibility is enhanced by its support for different grid types and its user-friendly interface. It seamlessly integrates with other modules, providing hydrodynamic conditions for coupled modelling, and leverages efficient parallelization techniques and high-performance computing resources. Overall, MIKE HD is a comprehensive and powerful tool for modelling and analyzing hydrodynamic processes in various marine and coastal applications.

The equation in shallow water is as follows

By merging the equation of horizontal momentum and the continuity equation for shallow water depth ($h = \eta + d$) where h represents the total water depth as the sum of the water level η and the bottom elevation d within the Cartesian coordinate system, we arrive at the subsequent equation:

$$\frac{\partial h}{\partial t} + \frac{\partial \overline{hu}}{\partial x} + \frac{\partial \overline{hv}}{\partial y} = hS$$

Equation III-13

$$\frac{\partial \overline{hu}}{\partial t} + \frac{\partial \overline{hu^2}}{\partial x} + \frac{\partial \overline{hvu}}{\partial y} = fvh - gh\frac{\partial \eta}{\partial t} - \frac{h}{\rho_0}\frac{\partial p_a}{\partial x} - \frac{gh^2}{2\rho_0}\frac{\partial \rho_w}{\partial x} + \frac{\tau_{sx}}{\rho_0} - \frac{\tau_{bx}}{\rho_0} - \frac{1}{\rho_0}\left(\frac{\partial S_{xx}}{\partial x} + \frac{\partial S_{xy}}{\partial y}\right) + \frac{\partial}{\partial x}(hT_{xx}) + \frac{\partial}{\partial x}(hT_{xy}) + hu_sS$$

Equation III-14

$$\frac{\partial \overline{hv}}{\partial t} + \frac{\partial \overline{huv}}{\partial x} + \frac{\partial \overline{hv^2}}{\partial y} = fuh - gh\frac{\partial \eta}{\partial t} - \frac{h}{\rho_0}\frac{\partial p_a}{\partial y} - \frac{gh^2}{2\rho_0}\frac{\partial \rho_w}{\partial y} + \frac{\tau_{sy}}{\rho_0} - \frac{\tau_{by}}{\rho_0} - \frac{1}{\rho_0}\left(\frac{\partial S_{yx}}{\partial y} + \frac{\partial S_{yy}}{\partial y}\right) + \frac{\partial}{\partial x}(hT_{xy}) + \frac{\partial}{\partial x}(hT_{yy}) + hv_sS$$

Equation III-15

The speeds of the currents at the average depth are defined as follows:

$$h\bar{u} = \int_{-d}^{\eta} udz$$ **Equation III-16**

$$h\bar{u} = \int_{-d}^{\eta} vdz$$ **Equation III-17**

The lateral stress forces T_{ij} consist of viscous friction, differential advection, and turbulent friction. These forces are computed based on turbulent viscosity using the formulation of average velocity gradients at depth.

$$T_{xx} = 2A\frac{\partial \bar{u}}{\partial x'}$$ **Equation III-18**

$$T_{xy} = A(\frac{\partial \bar{u}}{\partial y'} + \frac{\partial \bar{v}}{\partial x'})$$ **Equation III-19**

$$T_{yy} = 2A\frac{\partial \bar{v}}{\partial y}$$ **Equation III-20**

Table III-4 Symbols and Significations in Shallow Water Equations and Current Velocities.

Symbol	Signification	Symbol	Signification
t	Time.	**A**	Horizontal viscosity.
Pa	Atmospheric pressure.	**g**	Gravity acceleration.
x. y et z	Cartesian coordinates.	$\boldsymbol{\rho_w}$	Water density.
η	Surface elevation.	$\boldsymbol{S_{xx}}$,$\boldsymbol{S_{xy}}$ $\boldsymbol{S_{yx}}$ et $\boldsymbol{S_{yy}}$	Component of the radial tensor.
d	Water depth.	$\boldsymbol{\nu_t}$	Turbulent vertical viscosity.
h = η+d	Total water depth.	$\boldsymbol{\rho_0}$	The reference density of water.
u, v et w	Velocity components in the x, y, and z directions.	**S**	Amplitude of discharge caused by point sources.
$\boldsymbol{(u_s,v_s)}$	Velocity at which water is discharged into the ambient water.	$\boldsymbol{(\tau_{bx},\tau_{by})}$	x and y components of bottom wind stress.
$\boldsymbol{(\tau_{sx}, \tau_{sy})}$	x and y components of surface wind stress.	**Tij**	Lateral stresses.
u, v	Velocities of currents at the mean depth.	**f = 2Ω sinΦ**	Coriolis parameter {Ω is the angular velocity and Φ is the geographical latitude}.
Ω	Angular velocity of rotation.		

III.3. Methodology of Study

III.3.1. Generation of the mesh

To ensure comprehensive analysis and minimize errors that can affect simulation outcomes, both the marina and Algiers Port have been included as study areas. The regional scale chosen covers approximately 15.27 km extends from Cap Caxine in the west to Cap Matifou in the east, passing through Algiers Bay. Additionally, a distance of 19 km north of the marina is considered.

This scale allows account the coastal features and various structures present in both the marina and Algiers Port, which can potentially impact water movement. By considering the hydrodynamic effects of waves in both areas, a more comprehensive understanding of their impact on the marina and Algiers Port can be achieved.

Input bathymetric data for the mesh

The bathymetry utilized in this study was generated by combining data from three different sources: field data, NAVIONICS, and GEBCO. For the marina area and Algiers Port, comprehensive bathymetric data were available, covering both the interior of the basin and the areas outside the protective structures.

To obtain the bathymetry of Algiers Bay, a digitalization process was employed on the NAVIONICS SonarChart™ map, specifically the 2021 edition. This map was scaled at 1/250,000 and provided varying resolution ranging from 100 to 0.5 meters, transitioning from offshore to the coastline (ALEM.A and SAF.B, 2021).

For depths exceeding -200 meters, the GEBCO database served as the primary data source. However, to enhance the accuracy and detail, additional bathymetric information was incorporated. This included digitizing marine charts specific to the central Algerian region and incorporating previously developed bay-scale bathymetry data.

The ArcGIS 10.4 software package, developed by Esri (Environmental Systems Research Institute), was employed for this purpose. ArcGIS encompasses several interconnected modules, such as ArcMap, ArcScene, and ArcCatalog, enabling efficient geographic information system (GIS) workflows.

In order to integrate the bathymetric data into the MIKE21 modeling software and minimize errors during the simulation process, a conversion process was necessary. The ArcMap shapefile bathymetry data were transformed into XYZ files using the conversion tool available within the ArcToolbox. This conversion facilitated the compatibility of the bathymetric data with MIKE21 for subsequent analysis and simulations.

After generating the mesh, it is necessary to interpolate the bathymetry points onto the mesh grid. Various interpolation methods can be employed regardless of the type of mesh used. The

mesh generator provides two interpolation options specifically for triangular elements. These two possible interpolation methods are the nearest neighbor and linear interpolation (DHI, 2014).

In our case, we have chosen the nearest neighbor interpolation method. This method involves assigning the value of the nearest bathymetry point to each corresponding node or element in the mesh. By utilizing this interpolation approach, we ensure that each node or element in the mesh is associated with the bathymetry value of the closest point.

The nearest neighbor interpolation method is particularly useful when accuracy and preservation of sharp features or abrupt changes in bathymetry are crucial. It provides a straightforward and efficient way to transfer bathymetry information onto the mesh, allowing for accurate representation of the underwater topography in the simulation.

III.3.2. Mesh and bathymetry results

The nested mesh consists of 5391 nodes and 9820 triangular elements. The spacing between nodes varies from 13 meters near the marina and 18m near to the Algiers Port and 2 kilometers in the offshore area. This resolution allows for a detailed representation of the topography and bathymetry in the study area.

To ensure accurate simulation results and capture the specific characteristics of the marina and Algiers Port, the nested mesh was carefully tailored. It provides a high level of resolution and detail in these areas, enabling the modeling of complex hydrodynamic processes, including wave interactions, refraction, and the impact of structures.

By utilizing a nested mesh, we can accurately simulate the behavior of waves and other water-related phenomena within the marina and Algiers Port. This approach enhances the precision and reliability of our modeling results, enabling a thorough understanding of the hydrodynamics and potential impacts in these specific areas of interest.

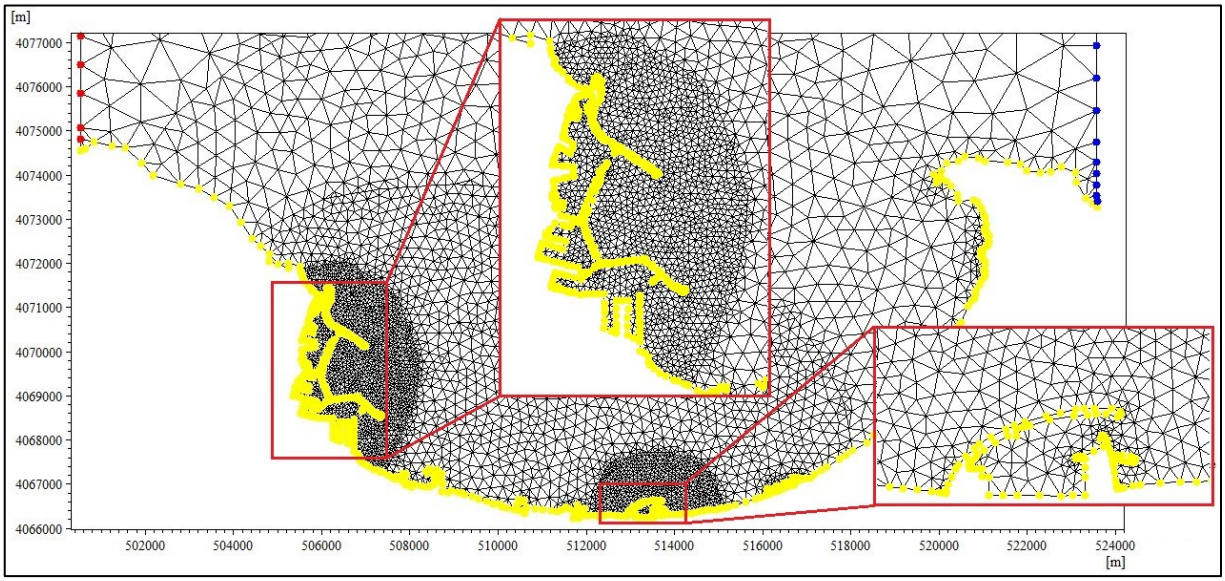

Figure III-1 The mesh of the Marina and Port of Algiers

Bathymetry of Algiers Bay

The bathymetry of the bay of Algiers can be categorized into three distinct zones. The areas near the eastern and western capes exhibit steep slopes, influenced by the geology of the capes, which consist of harder and more resistant lithology such as cliffs. These zones also experience strong hydrodynamic effects, making them energetically favorable areas where wave orthogonal converge. The transition from the coastline to the -50 meter isobath occurs over a relatively short distance on both sides of the bay.

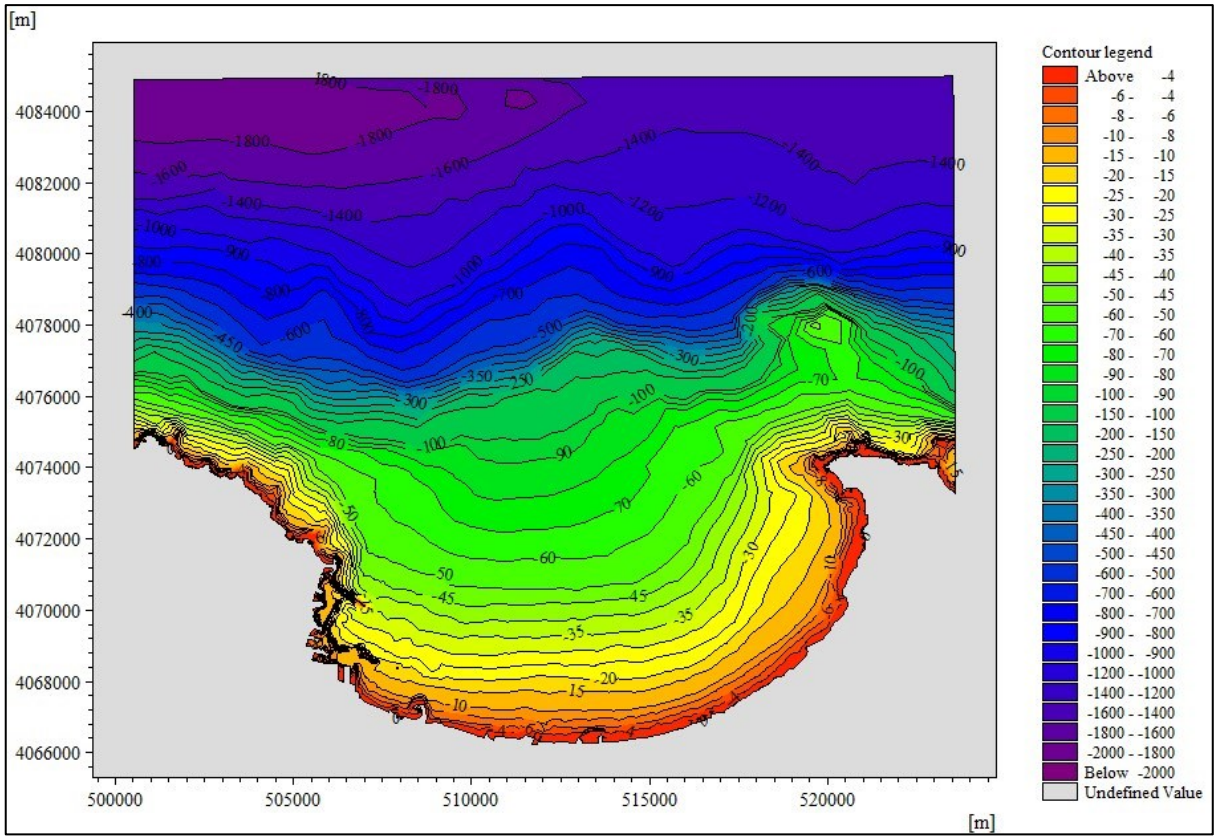

Figure III-2 Bathymetry of Algiers Bay.

In contrast, the central zone of the bay of Algiers features a predominantly smooth slope. This is primarily attributed to the lithology of this area, which is softer and more erodible. The presence of sandy beaches, nourished by sediment input from the two rivers in the bay, contributes to the overall low slope observed. Additionally, the wave energy in this central area is relatively lower compared to the zones near the capes.

Offshore of the bay of Algiers, the continental shelf terminates directly at the bay's exit. This is characterized by closely spaced isobaths, confirming the findings from the regional-scale analysis of the broader central Algerian region's morphology.

Bathymetry in the area of the Marina and the Port of Algiers

Bathymetry of the Algiers Port

From Figure III-3, the bathymetry of the port can be categorized into two distinct sections

Outside the port: The area between the Khireddine and Mustapha jetties exhibits uniform and parallel isobaths aligned with the coastline. Depths range from -15m to -30m, with an access channel situated at a depth of -30m. These features indicate a consistent seabed and a gradual slope.

Inside the port: it can be divided into three parts:

- **Old Port Basin:** Accessed through the North Pass and located between the Khireddine and Old Port jetties. The bathymetry in this zone varies from -8m near the quays with closely spaced isobaths to -20m at the center of the basin, where the isobaths are more regularly spaced. The basin has a depth of -10m to accommodate large ships. The decrease in depth near the quays can be attributed to sedimentation.
- **Agha Basin:** Accessed through the South Pass and protected by the Agha jetty. Depths in this area range from -6m near the quays with closely spaced isobaths to -12m at the center of the basin, where the isobaths are more evenly spaced. The depth reduction near the quays is also caused by sedimentation.
- **Mustapha Basin:** Accessed through the South Pass and protected by the Mustapha jetty and Mustapha East Breakwater jetty. Depths in this basin range from -4m near the quays with closely spaced isobaths to -15m at the center, where the isobaths are more regularly spaced. There is a -15m access channel to accommodate medium-sized vessels. The decrease in depth near the quays is a result of sedimentation in this basin.

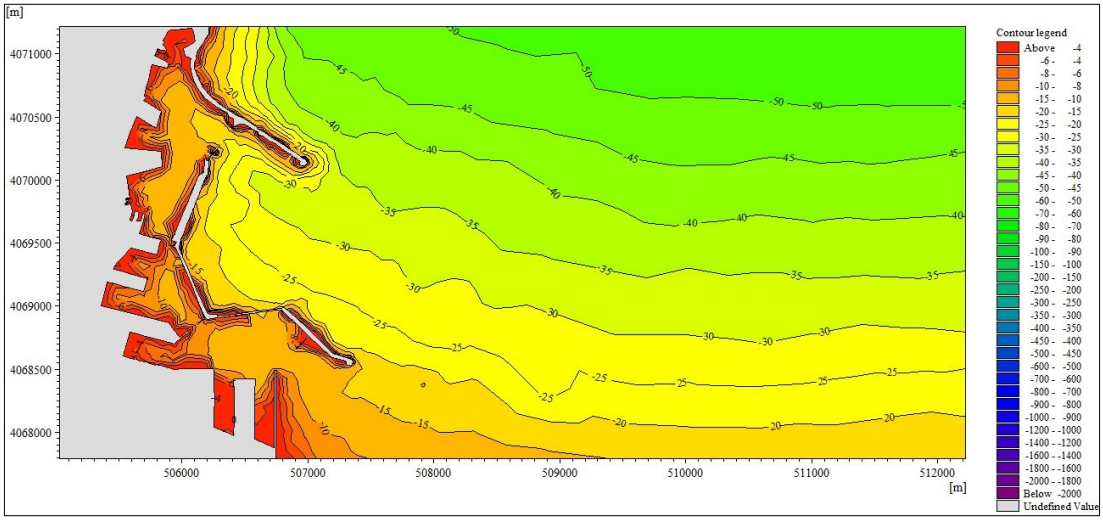

Figure III-3 Bathymetry of the Algiers Port.

Bathymetry of the Algiers Marina:

Bathymetry Inside the Marina:

The bathymetric data within the marina area reveals moderately regular and parallel isobaths to the coastline, indicating a smooth slope and a consistent seabed. Depths range from 0.5 to 2 meters, with the overall basin depths varying from -0.8 to -5.2 meters. The shallowest depths (-0.8 to -2 meters) are found near the rooting area, potentially due to the original geomorphology

associated with underlying rock formations. The rest of the basin exhibits bathymetry ranging from -2 to -5.2 meters, displaying a gradual slope.

Bathymetry Outside the Marina:

- The outer section of the primary jetty displays closely spaced isobaths (-1.2 meters and -6 meters), indicative of a steep slope resulting from construction materials and the dike's configuration.
- Towards the eastern side of the marina, isobaths appear relatively spaced apart (-1.6 meters to -6 meters), suggesting a regular seabed and smooth slope due to the presence of a secondary jetty which obstructs longitudinal sediment transport from east to west, leading to sediment accumulation and the formation of a new beach.
- To the west of the marina, the isobaths are also spaced apart (ranging from -1.6 meters to -10 meters), reflecting a regular seabed with a smooth slope. This area benefits from sediment supply originating from Oued El Harrach, located further west. The sediment influx replaces sediment trapping on the east side, thus safeguarding the western beach from erosion.

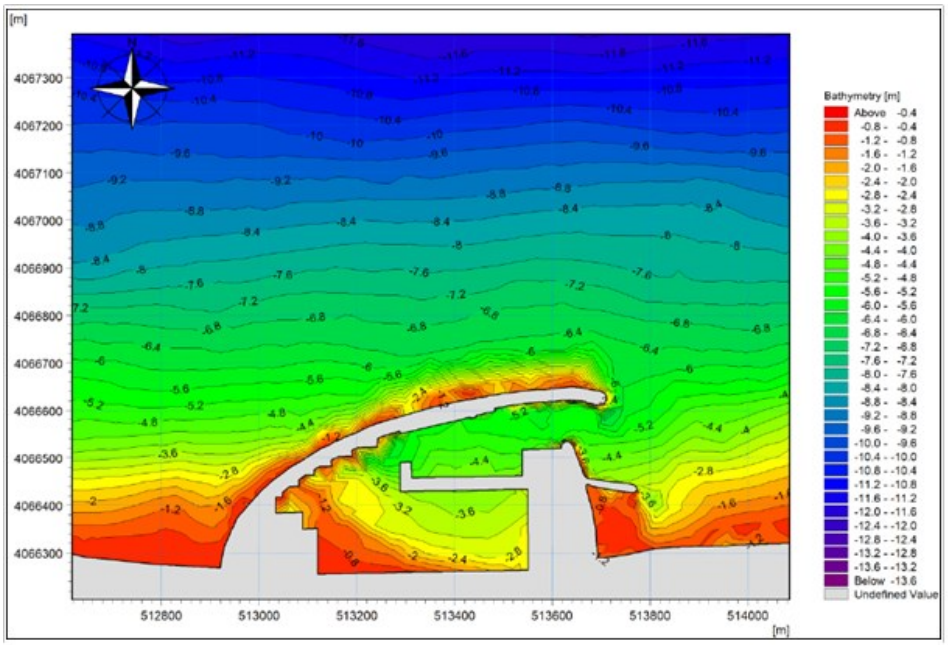

Figure III-4 Bathymetry of the Algiers Marina.

III.4. Penalizing directions

In the context of modeling the hydrodynamics of the study area, the Algerian Bay, specifically the selected ports, the Port of Algiers and the Algiers Marina, we analyzed the "Infoplaza" wave climate database. Through this analysis, we were able to identify the four most influential directions on the evolution and stability of the port structures: NNW (north-northwest), N (north), NNE (north-northeast), and NE (northeast). These directions correspond to return periods of 2 years, 10 years, 30 years, and 100 years.

To facilitate the interpretation of the results, we chose two extraction points located 20 meters from the main dike of the Marina and 40 meters from the Khireddine jetty of the Port of Algiers. The coordinates (x, y) of these points are provided, and the figures illustrate these two locations.

Table III-5 The coordinates (x, y) for the two extracted points.

Coordinates (X, Y)	for the Algiers Marina	for the Port of Algiers
X (m)	513550	506978
Y (m)	4066668	4070210

Algiers Port

Algiers Marina

Figure III-5 Map of Extraction Points at 20 meters from the Main Breakwater of the Marina and 40 meters from the Base of the Khireddine Jetty in the Port of Algiers.

III.5. Simulations and results

III.5.1. Simulation Scenario

After identifying the penalizing wave directions and calculating extreme events in the previous chapter, a methodology was employed to determine the maximum wave height associated with each return period for the four critical directions. Additionally, the analysis considered the projected sea level rise as outlined in the IPCC 2019 report. The resulting wave and current data for these directions are presented in Table III-6.

Table III-6 Simulation inputs for all return periods.

Return Periods (years)	Parameters	Wave Parameters					Sea Level (m)
		NW	NNW	N	NNE	NE	
	U10 (m/s)	5.53	5.29	6.61	4.1	5.37	
	DirU10 (°)	231.94	226.49	359.8	141.49	107.62	
2	Hs (m)	4.24	4.15	4.25	4.64	3.34	NGA = +0.34 m
	Tp (s)	8.51	8.34	9.46	8.73	8.39	Future elevation = 0m
							Total = 0.34 m
5	Hs (m)	4.88	4.73	4.93	5.3	3.86	NGA = +0.34 m
	Tp (s)	8.4	8.72	9.59	10.53	8.37	Future elevation = 0 m
							Total = 0.34 m
10	Hs (m)	5.36	5.16	5.44	5.81	4.25	NGA = +0.34 m
	Tp (s)	9.75	8.75	11.58	11.57	7.95	Future elevation = 0 m
							Total = 0.34 m
20	Hs (m)	5.85	5.6	5.95	6.31	4.64	NGA = +0.34 m
	Tp (s)	9.56	9.56	10.49	11.56	8.76	Future elevation = 0 m
							Total = 0.34 m
30	Hs (m)	6.13	5.86	6.25	6.61	4.87	NGA = +0.34 m
	Tp (s)	9.13	8.69	11.04	11.54	8.76	Future elevation = 0.25 m
							Total = 0.59 m
50	Hs (m)	6.49	6.18	6.63	6.98	5.16	NGA = +0.34 m
	Tp (s)	9.54	9.12	11.04	11.61	9.13	Future elevation = 0.30 m
							Total = 0.64 m
100	Hs (m)	6.97	6.62	7.14	7.49	5.56	NGA = +0.34 m
	Tp (s)	9.54	9.33	10.48	11.89	10.56	Future elevation = 0.45 m
							Total = 0.79 m
1000	Hs (m)	8.58	8.08	8.85	9.16	6.86	NGA = +0.34 m
	Tp (s)	10.53	9.54	11.06	12.4	11.95	Future elevation = 1 m
							Total = 1.34 m

Note:

It should be noted that all the simulations were associated with a constant wind for each direction (see Table III-1). The average wind speed and direction were obtained after processing a record from 1992 to 2022 from the WaveClimat database in Algiers Bay.

The coupling of a wind event with a wave event of the same return period results in significantly overestimated results. For instance, coupling a 100-year wave and wind event would yield a scenario that occurs once every 10,000 years, which is illogical considering the average lifespan of maritime structures, typically ranging from 100 to 150 years. The proposed solution is to determine the probability of occurrence for wind/wave combinations, commonly known as joint or cross probability.

After the simulations, the results are presented in the form of labeled maps and comparative tables for the four influential directions NNW (North-Northwest), N (North), NNE (North-Northeast), and NE (Northeast). The simulations focus on several output parameters, including:

- Significant Wave Height (Hs) at:
    1. 20 meters from the main breakwater of the Marina
    2. 40 meters from the main breakwater Khireddine of the Port of Algiers
- Peak Wave Period: This parameter represents the duration between successive wave crests or troughs. It indicates the time it takes for the most energetic wave to pass a certain point.
- Mean Wave Direction: This parameter denotes the average direction from which the waves approach the specified locations. It provides valuable information about the prevailing wave patterns.
- Wave Power Energy: This parameter quantifies the amount of energy carried by the waves at the selected locations. Wave power is an essential factor in evaluating the potential for harnessing renewable energy from sea waves.

The Table III-7 presents wave simulation results for different return periods (2, 10, 30, and 100 years) at the Marina and Port of Algiers. It provides information on wave characteristics such as significant wave height (H_s), shoaling coefficient, peak wave period (T_p), mean wave direction, and wave power. The data is organized based on simulated directions, including NNW (North-Northwest), N (North), NNE (North-Northeast), and NE (Northeast). For each combination of direction and return period, the table specifies the offshore H_s, H_s at the base of the structure, shoaling coefficient, T_p, mean wave direction, and wave power. This information offers insights into the wave conditions at the two locations under different return periods and simulated directions.

Table III-7 Results of wave simulations for the return periods of 2, 10,30, and 100 years.

Wave Characteristics							
Simulated Directions	Return Period (years)	Offshore H_s (m)	H_s (m)at the base of the structure	Shoaling Coefficient (%)	T_p (s)	Mean Wave Direction (°)	Wave Power (KW/m)
Marina of Algiers							
NNW (337.5°)	2	4.15	2.19	52.77	8.46	349.51	26.03
	10	5.16	2.31	44.77	8.92	350.54	19.77
	30	5.86	2.32	39.59	8.8	351	20.07
	100	8.08	2.35	29.08	9.42	351	20.78
N (360°)	2	4.25	2.33	54.82	9.39	356.45	20.29
	10	5.44	2.49	45.77	11.42	356.46	23.87
	30	6.25	2.47	39.52	11.14	356.4	23.41
	100	7.14	2.43	34.03	10.48	356.32	22.67
NNE (22.5°)	2	4.64	2.22	47.84	8.74	2.79	17.69
	10	5.81	2.49	42.86	11.4	2.46	23.76
	30	6.61	2.5	37.82	11.41	2.21	23.91
	100	7.49	2.53	33.78	11.98	2	24.59
NE (45°)	2	3.34	1.75	52.4	8.41	8.54	9.81
	10	4.25	1.86	43.76	8	7.73	11.31
	30	4.87	2.02	41.48	8.75	7.78	13.98
	100	5.56	2.22	39.93	10.46	7.63	17.93
Port of Algiers							
NNW (337.5°)	2	4.15	2.34	56.39	8.39	8.19	22.7
	10	5.16	2.96	57.36	8.72	9.12	37.66
	30	5.86	3.53	60.24	8.66	9.6	55.6
	100	8.08	3.81	47.15	9.34	10.31	65.93
N (360°)	2	4.25	3.13	73.65	9.36	16.66	45.51
	10	5.44	4.05	74.45	11.41	17.64	86.5
	30	6.25	4.42	70.72	11.11	17.92	102.35
	100	7.14	4.93	69.05	10.41	17.95	124.14
NNE (22.5°)	2	4.64	3.54	76.29	8.74	24.9	56.15
	10	5.81	4.68	80.55	11.41	25.14	118.3
	30	6.61	5.11	77.3	11.41	25.2	142.48
	100	7.49	5.7	76.1	11.99	25.25	181.44
NE (45°)	2	3.34	2.53	75.75	8.41	34.94	27.52
	10	4.25	3.07	72.24	8.09	34.14	39.1
	30	4.87	3.45	70.84	8.84	33.82	53.52
	100	5.56	4.08	73.38	10.46	33.35	84.97

III.5.2. Results interpretation

2-Year Return Period

The results obtained for the 2-year return period are presented in Table III-7 and Figure III-6. Offshore waves in the Bay retain more than 95% of their initial height of 4.64 m at the model boundaries due to the deep water near the Bay of Algiers. The seabed does not affect the waves significantly.

As the waves enter the bay, their characteristics (height and initial power of 83 KW/m) gradually decrease due to the underwater morphology of the bay, which is characterized by reduced depth. The waves are slowed down by the seabed, undergo significant deviation through diffraction and refraction when encountering obstacles, resulting in a progressive loss of energy.

All waves approach the structure with a north direction in the marina and a North-Northeast direction in the port, influenced by orthogonal lines perpendicular to the isobaths.

On the marina side, Cape Matifou provides direct protection to the area. Additionally, due to the underwater topography, the waves reaching the base of the structure have a height of approximately 2.22 m, with a shoaling coefficient of 0.48, indicating a loss about half of their intensity.

On the port side, Cape Matifou does not offer any protection to the area. Waves from this direction attack the port obliquely, resulting in higher wave heights at the jetties compared to the marina. These waves have a height of approximately 3.54 m, with a shoaling coefficient of about 0.48, indicating a loss of only 17% of their initial energy.

The currents in the area, generated by winds and waves from the North-Northeast direction, flow East-West along the coast with an average speed of about 0.33 m/s. The incident wave direction plays a significant role in generating currents in shallow areas near the coast.

In conclusion, the wave simulation for the 2-year return period, considering the most challenging direction, demonstrates that the marina remains protected against wave and current impacts. Although wave diffraction on the breakwater is observed, the marina's protection is maintained; unlike the Port which is quite exposed to wave attacks of this direction.

10-Year Return Period

The results obtained for the 10-year return period are presented in Table III-7and Figure III-7. According to the results, offshore waves in the Bay retain over 93% of their initial height of 5.81 m at the model boundaries.

As the waves enter the bay, their hydrodynamic characteristics, such as height and initial power of 170 KW/m, gradually decrease due to friction with the seabed, which slows down the wave and causes deviation through diffraction and refraction when encountering obstacles, leading to a progressive loss of energy.

In the marina area, the protection provided by Cape Matifou and the bathymetry result in waves reaching the base of the structure with a height of approximately 2.49 m, with a shoaling coefficient of about 0.43. This indicates that the waves have lost more than half of their intensity.

On the port side, since Cape Matifou does not offer any protection to the area and the waves from this direction attack the port obliquely, the wave heights on the jetties are higher compared to those observed in the marina, reaching approximately 4.68 m with a shoaling coefficient of about 0.48. This means that the waves have only lost 20% of their initial energy.

It is observed that all waves arrive at the base of the structure from the North direction in the marina and from the North-Northeast direction in the port. This observation can be explained by the presence of orthogonal lines perpendicular to the isobaths.

Regarding the currents in the area, the winds and waves from the North-Northeast direction generate East-West currents along the coast with an average speed of about 0.35 m/s. These observations lead us to conclude that the current patterns in the area are not significantly influenced by variations in wave height and period offshore.

30-Year Return Period

The results obtained for the 30-year return period are presented in Table III-7 and Figure III-8. The analysis reveals that the Bay waves offshore retain over 92% of their initial height of 6.61 m at the model boundaries.

Once the waves enter the bay, their hydrodynamic characteristics, including height and initial power of 220 KW/m, gradually decrease due to friction with the seabed. This friction slows down the wave's progression and alters its path through diffraction and refraction when encountering obstacles, resulting in a progressive dissipation of its energy.

Concerning the Marina, the combined protection offered by Cape Matifou and the bathymetry leads to waves reaching the base of the structure with a height of approximately 2.50 m and a shoaling coefficient of around 0.38. This indicates a significant reduction of 63% in wave intensity.

On the other hand, the Port area lacks the protective effect of Cape Matifou, causing waves approaching from this direction to strike the port obliquely. As a result, the wave heights observed on the jetties are higher than those in the marina, reaching approximately 5.11 m with a shoaling coefficient of about 0.48. In this case, the wave energy decreases by only 33% from its initial state.

The analysis also reveals that all waves converge at the structure's base with a Northward direction in the marina and a North-Northeast direction in the port. This behavior is attributed to the presence of orthogonal lines perpendicular to the isobaths.

Regarding the current patterns in the area, winds and waves originating from the North-Northeast generate East-West currents along the coast, with an average speed of around 0.4 m/s. These observations indicate that the current dynamics in the area are not significantly influenced by variations in wave height and period offshore.

100-Year Return Period

The results obtained for the 100-year return period are presented in Table III-7 and Figure III-9. The analysis shows that the Bay waves offshore retain over 91% of their initial height of 7.49 m at the model boundaries.

As the waves enter the bay, their hydrodynamic characteristics, including height and initial power of 292 KW/m, gradually decrease due to friction with the seabed. This friction slows down the wave's progression and alters its path through diffraction and refraction when encountering obstacles, resulting in a progressive dissipation of its energy.

Concerning the Marina, the combined protection offered by Cape Matifou and the bathymetry results in waves reaching the base of the structure with a height of approximately 2.53 m and a shoaling coefficient of around 0.34. This indicates a significant reduction of 77% in wave intensity.

On the other hand, the Port area lacks the protective effect of Cape Matifou, causing waves approaching from this direction to strike the port obliquely. As a result, the wave heights observed on the jetties are higher than those in the marina, reaching approximately 5.7 m with a shoaling coefficient of about 0.76. In this case, the wave energy decreases by only 24% from its initial state.

The analysis also reveals that all waves converge at the structure's base with a Northward direction in the marina and a north-northeast direction in the port. This behavior is attributed to the presence of orthogonal lines perpendicular to the isobaths.

Regarding the current patterns in the area, winds and waves originating from the North-Northeast generate East-West currents along the coast with a higher average speed compared to other return periods, approximately 0.45 m/s. These observations indicate that the current dynamics in the area are not significantly influenced by variations in wave height and period offshore.

In summary, the wave simulation results reveal varying levels of protection and exposure for the marina and port. The marina benefits from effective protection provided by Cape Matifou and the bathymetry, resulting in a significant reduction in wave intensity. However, the port lacks the same level of protection, making it more vulnerable to higher wave heights. These findings emphasize the importance of considering different return periods and implementing appropriate measures to ensure the resilience of coastal structures. The consistent east-west flow of currents along the coast indicates a stable pattern in the area, unaffected by offshore wave variations.

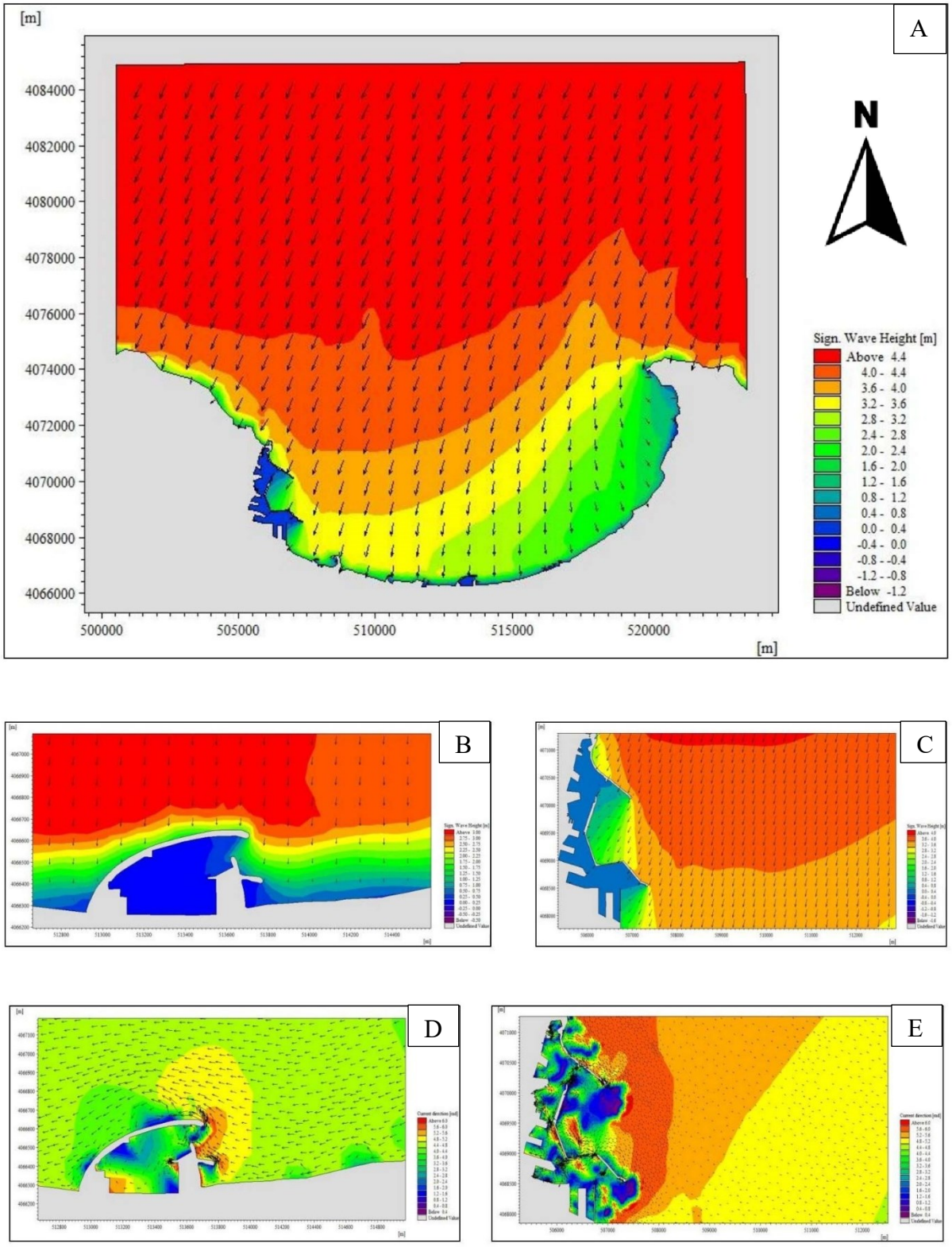

Figure III-6 Wave fields and current directions for the NNE direction in the Bay of Algiers (For 2 years return period)

A. Overview of wave fields for the NNE direction in the Bay of Algiers
B. Wave fields for the NNE direction in Algiers Marina
C. Wave fields for the NNE direction in Algiers Port
D. Current directions for the NNE direction near the Marina in Algiers Marina
E. Current directions for the NNE direction near Algiers Port

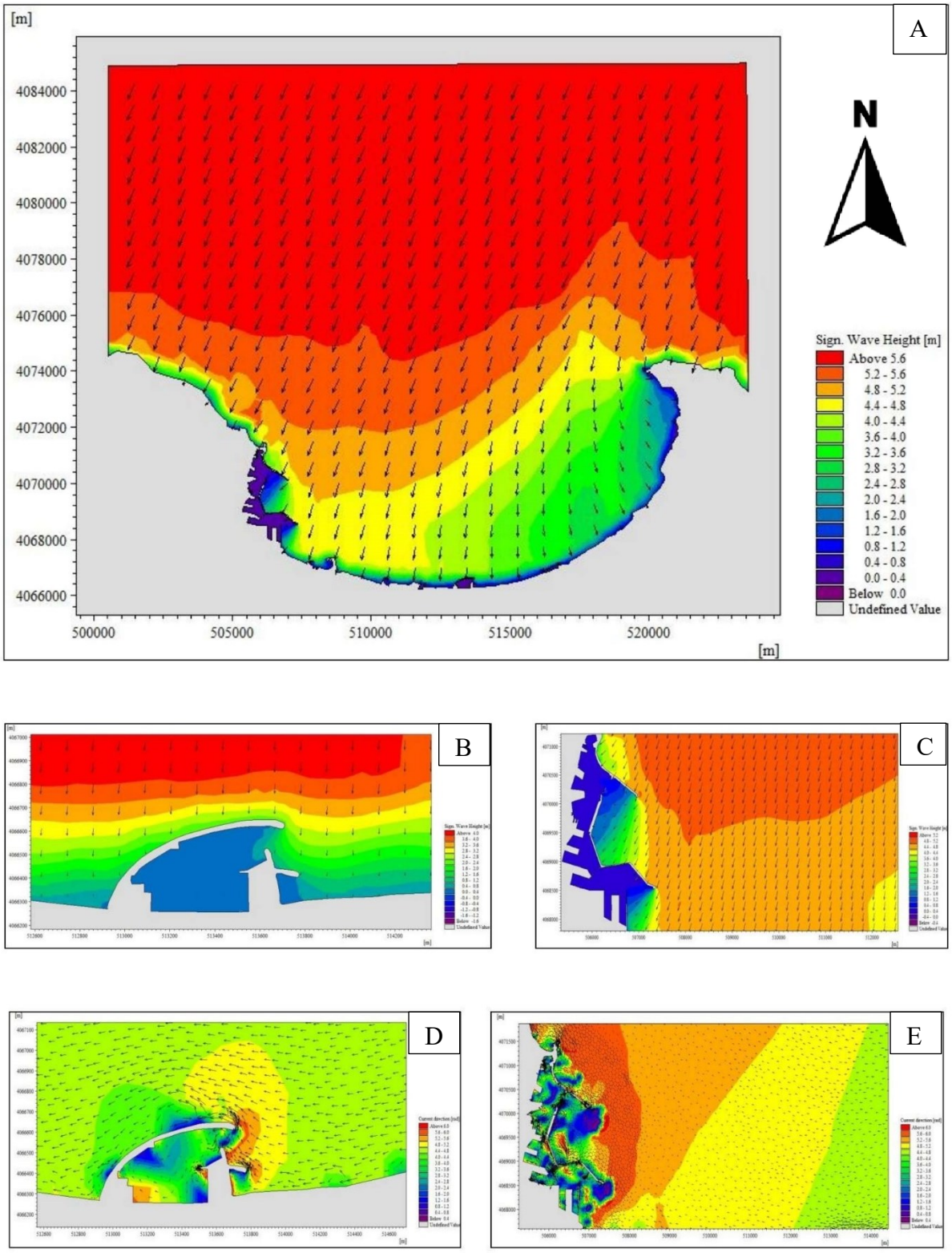

Figure III-7 Wave fields and current directions for the NNE direction in the Bay of Algiers (For 10 years return period)

A. Overview of wave fields for the NNE direction in the Bay of Algiers.
B. Wave fields for the NNE direction in Algiers Marina.
C. Wave fields for the NNE direction in Algiers Port.
D. Current directions for the NNE direction near the Marina in Algiers Marina.
E. Current directions for the NNE direction near Algiers Port.

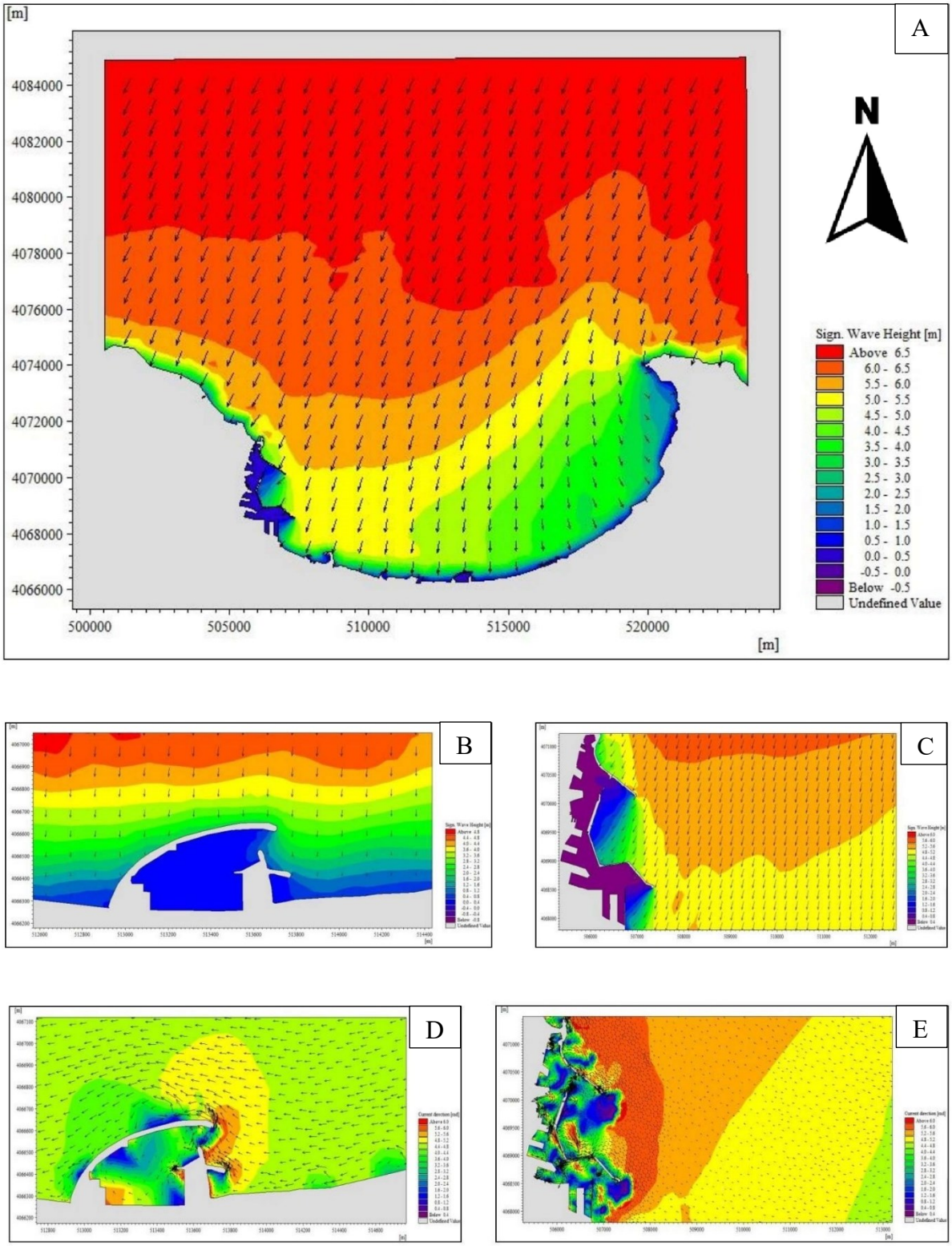

Figure III-8 Wave fields and current directions for the NNE direction in the Bay of Algiers (For 30 years return period)

A. Overview of wave fields for the NNE direction in the Bay of Algiers
B. Wave fields for the NNE direction in Algiers Marina
C. Wave fields for the NNE direction in Algiers Port
D. Current directions for the NNE direction near the Marina in Algiers Marina
E. Current directions for the NNE direction near Algiers Port

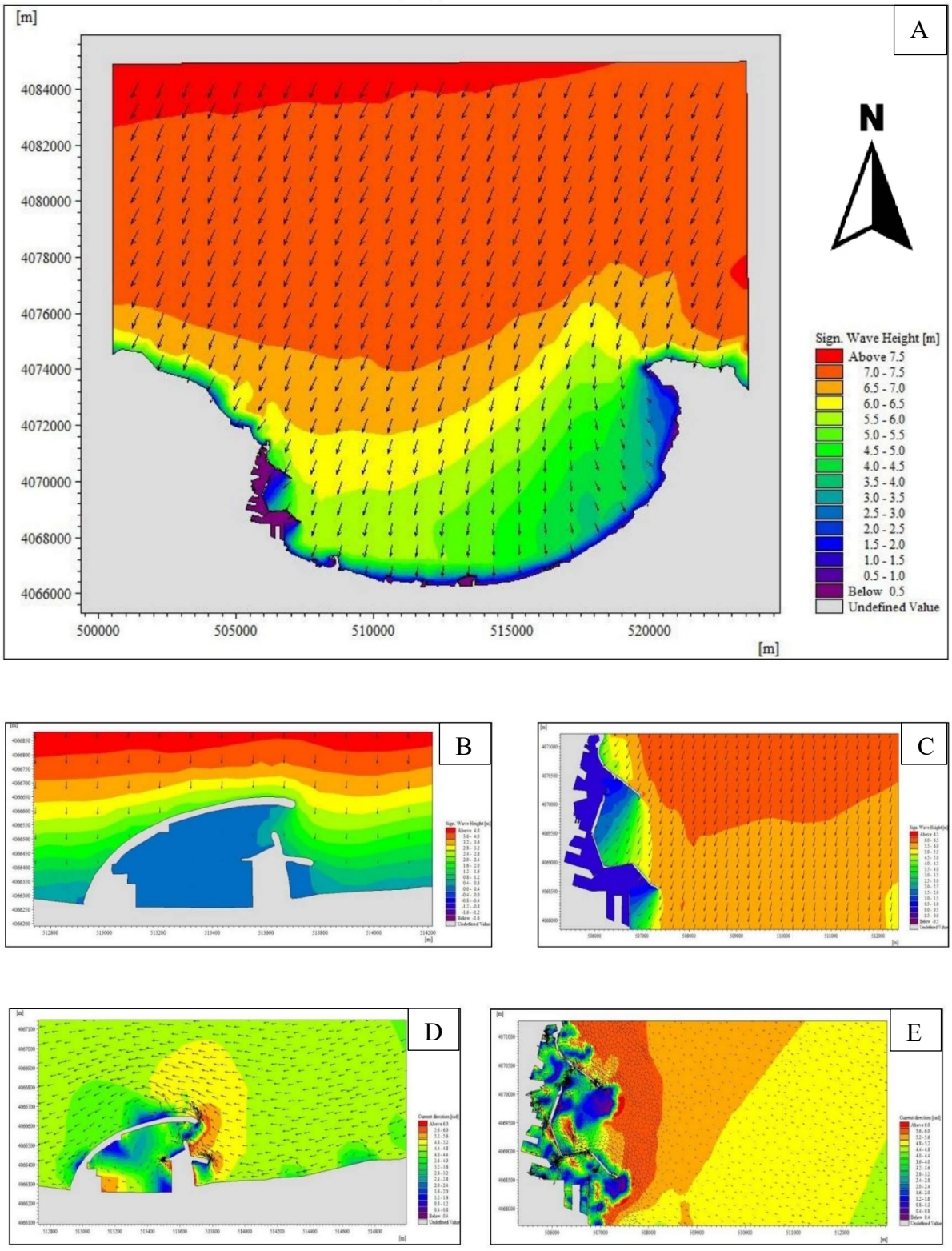

Figure III-9 Wave fields and current directions for the NNE direction in the Bay of Algiers (For 100 years return period)

A. Overview of wave fields for the NNE direction in the Bay of Algiers
B. Wave fields for the NNE direction in Algiers Marina
C. Wave fields for the NNE direction in Algiers Port
D. Current directions for the NNE direction near the Marina in Algiers Marina
E. Current directions for the NNE direction near Algiers Port

III.6. Conclusion

In conclusion, our numerical modeling has allowed us to the most unfavorable wave directions: North-Northwest, North, North-Northeast, and Northeast. Our observations highlight the significant role played by the morpho-bathymetry of the bay of Algiers in effectively reducing wave heights that impact coastal structures.

At the Marina, there has been a remarkable reduction of over 55% in wave heights for large-amplitude waves. Furthermore, the interaction between waves and the seafloor predominantly directs wave propagation towards the north in the Marina area.

In contrast, the reduction in wave heights at the Port has been less pronounced, reaching approximately 20% for large-amplitude waves.

Regarding the current patterns, it appears that extreme events do not significantly affect the local current velocities, which remain consistent across various simulated climate scenarios. However, the incident wave direction plays a significant role in shaping the current patterns, resulting in multiple flow directions and generated channels. The most notable impact is observed from waves coming from the North-Northeast, which generate circular currents on either side of the Marina and the Port. The recorded current velocities range from 0.3 m/s to 0.45 m/s.

The simulations demonstrate that both the Marina and the Port of Algiers are well-protected, as even during the most extreme events, wave heights remain significantly reduced at the entrance of the channel. In the Port, wave heights range between 0.3 m and 0.6 m for all return periods, while at the entrance of the channel in the Marina, they range between 0.4 m and 0.7 m.

Chapter IV. Design of rubble mounds breakwater

IV.1. Introduction

Coastal protection structures have the principal function of protecting the shoreline from erosion, reducing the intensity of wave action in inshore waters, and thereby providing safe harborage.

Two different formulas will be used for the design of coastal protection structures: the Hudson formula and the Van Der Meer formula.

In our case, we will design the rubble mound breakwaters.

IV.2. Rubble mound breakwaters

Rubble mound breakwaters are structures built of quarried rock or artificial concrete blocks in the shape of a trapezium. Breakwaters generally serve the purpose of providing calm water for vessel anchorage or mooring, protecting them from attack by waves and/or currents.

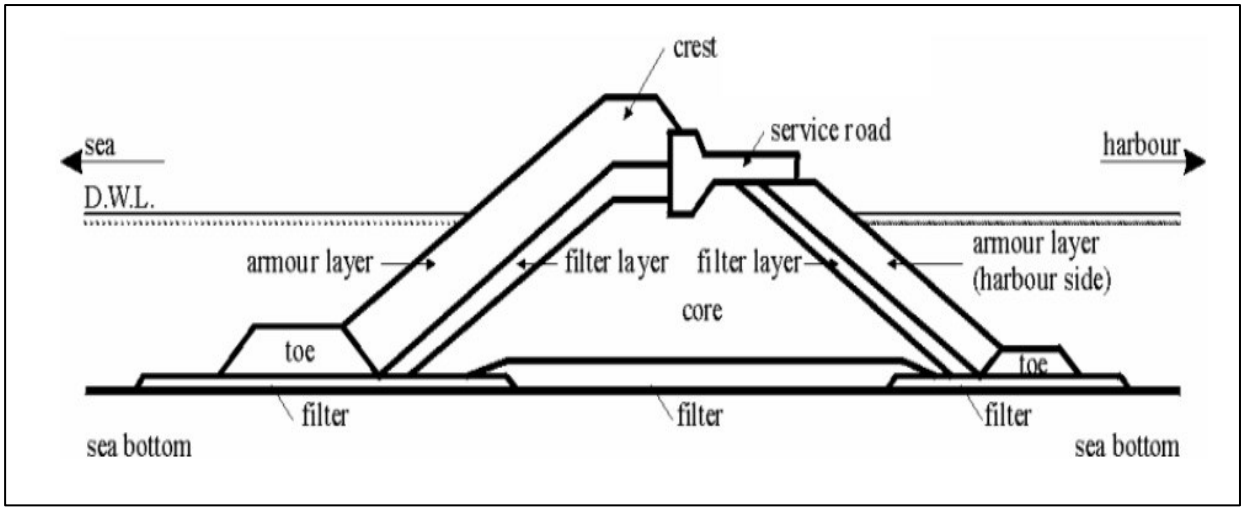

Figure IV-1 Typical cross section of a rubble mound breakwater (Troch, P. 2001).

The size of the blocks of the different materials used decreases from the outside inward, according to the constraints of the elements composing each layer, which must respect grain size range aspects (SHARP, N and al 1997).

Rubble mound breakwaters are made up of several distinct layers that work together to dissipate wave energy and maintain stability. The key components of a rubble mound breakwater include:

- **Core:** Its main function is to form the basis for the upper layers and to reduce the transmitted energy. Most of the times consist of quarry run (stones 1 to 500kg) with relatively large gradation (Papadopoulos D. 2012).
- **Filter layer (under-layer/secondary armor layer):** They are used as an interface between core and armor layer in order to prevent the core material to be washed out through the pores of the armor layer (Papadopoulos D. 2012).
- **Armor layer:** This layer is responsible for withstanding the forces imposed by the wave action during design conditions. Here, in case that natural stones are used, the gradation is lower. Apart from natural stones, when the design conditions are very demanding (high design wave height) or when there is a lack of natural material concrete armor units are used (Papadopoulos D. 2012).
- **Toe bund:** It serves as a lower wedge for the armor layer, limiting the risk of slipping of this layer, and offers of the latter, and it offers additional security against scouring at the toe of the structure (SHARP, N and al 1997).
- **Bedding layer**: In some cases, when constructing breakwaters in deep areas, a bedding layer may be required to provide a stable foundation for the breakwater structure. The bedding layer consists of low-cost materials chosen based on the hydrodynamic conditions and stability requirements of the breakwater. The weight and composition of the bedding layer are determined to ensure proper support and stability for the breakwater (SHARP, N and al 1997).

By combining these layers, rubble mound breakwaters effectively dissipate wave energy, protect coastal areas, and maintain stability over time. The specific design and composition of each layer depend on various factors such as wave conditions, site-specific requirements, and available construction materials. Proper design and construction practices are crucial for the effective performance and longevity of rubble mound breakwaters.

IV.3. Design of rubble mounds breakwaters

The design of maritime structures requires the definition of criteria that give the expected behavior of the structure. Many empirical methods for the prediction of the size of armor stone required for stability under wave attack have been proposed one of them the stability formulae developed by Hudson (1953), Van der Meer (1988b).

For both formulas we will determine:

- Weight, thickness and number of blocks per square meter for the breakwater.

- Weight and thickness of filters.

- Design of Toe bund.

IV.3.1. Hudson formula

Hudson derived a formula using the results of physical model experiments conducted using regular waves, Rubble mound breakwaters can either be protected against waves by natural armour stone or artificial concrete units.

Case of natural armour stone

Table IV-1 The Hudson formula for median mass and weight of natural armorstone

Formula	variables
The median mass of armour stone: $\boldsymbol{M_{50}} = \frac{\mathbf{1}}{\mathrm{K}_d} \frac{\rho_s H_b^3}{\Delta 3 \cot \alpha}$ The median weight of armour stone: $\boldsymbol{W_{50}} = \frac{\mathbf{1}}{\mathrm{K}_d} \frac{\rho_s g H_b^3}{\Delta 3 \cot \alpha}$	$\mathbf{K_d}$*:* stability coefficient. $\boldsymbol{\alpha}$ *:* the slope angle (°). $\mathbf{H_b}$ *:* wave height at the toe of the structure. $\Delta = \frac{\boldsymbol{\rho_s}}{\boldsymbol{\rho_w}} - \mathbf{1}$the relative buoyant density of the stone. $\boldsymbol{\rho_s}$: the apparent rock stone (kg/m³). $\boldsymbol{\rho_w}$: the apparent water density (kg/m³). $\boldsymbol{g}$: acceleration of Gravity.

Case of artificial concrete units

Previously, in the 1950s, the breakwaters were built in relatively shallow waters, and the natural stones were used as armour units. The need for heavy armour weights kept rising as the constructions moved into deeper waters, and such large stones were uneconomical to quarry and transport. As a result, concrete blocks in a wide variety of shapes were created as armour units for rubble structures.

Table IV-2 The Hudson formula for median mass and weight of concrete units.

Formula	variables
The median mass of armour units: $\boldsymbol{M_{50}} = \frac{\mathbf{1}}{\mathrm{K}_d} \frac{\rho_c H_b^3}{\Delta 3 \cot \alpha}$ The median weight of armour units: $\boldsymbol{W_{50}} = \frac{\mathbf{1}}{\mathrm{K}_d} \frac{\rho_c g H_b^3}{\Delta 3 \cot \alpha}$	$\mathbf{K_d}$: stability coefficient. $\boldsymbol{\alpha}$: the slope angle (°). $\mathbf{H_b}$: wave height at the toe of the structure. $\Delta = \frac{\boldsymbol{\rho_r}}{\boldsymbol{\rho_w}} - \mathbf{1}$the relative buoyant density of armour bloc. $\boldsymbol{\rho_c}$: the apparent concrete density (kg/m³). $\boldsymbol{\rho_w}$: the apparent water density (kg/m³). $\boldsymbol{g}$: acceleration of Gravity.

The Hudson formula offers simplicity as its main advantage for estimating wave forces on coastal structures. However, it has limitations:

- Limited to regular waves: It assumes regular waves and cannot account for irregular wave conditions commonly found in coastal areas.
- Ignores wave period and storm duration: The formula does not consider variations in wave period or the duration of storms, which are crucial factors influencing wave forces.

- No description of damage level: The formula focuses solely on estimating wave forces and does not provide information about the potential level of damage caused by waves.
- Limited to specific structures: It is designed for non-overtopped and permeable structures only, excluding overtopping waves and impermeable structures like breakwaters.

Given these limitations, caution must be exercised when using the Hudson formula, especially in complex coastal engineering situations. More advanced methods that consider specific wave characteristics, storm duration, structure type, and potential damage levels are recommended for accurate assessments.

Van der Meer formulae

The Van der Meer approach, introduced in 1988, is a formula widely used for determining the diameter of armour stones in coastal structures. This approach takes into account multiple parameters such as wave characteristics, wave breaking type, permeability, and other factors. By considering these variables, the Van der Meer formula provides a comprehensive method for selecting armour stone sizes that can effectively withstand the powerful forces generated by ocean waves. A crucial component of the approach is the surf similarity parameter **ξ**, which plays a significant role in determining the type of wave breaking present in the coastal area. By accurately assessing wave breaking, the formula ensures that the calculated armour stone diameter is appropriate for the specific conditions.

Deep water conditions

Table IV-3 Plunging and Surging Waves Van der Meer Formulae for Deep Water Conditions.

<table>
<tr><th colspan="2">Van der Meer formulae</th></tr>
<tr><th>Deep water</th><th>Variables</th></tr>
<tr><td>For plunging waves ($\xi_m<\xi_{cr}$):
$\frac{H_s}{\Delta D_{n50}} = c_{pl} P^{0.18} (\frac{S_d}{\sqrt{N}})^{0.2} \xi_m^{-0.5}$
and for surging waves ($\xi_m \geq \xi_{cr}$):
$\frac{H_s}{\Delta D_{n50}} = c_{pl} P^{-0.13} (\frac{S_d}{\sqrt{N}})^{0.2} \sqrt{cot\alpha}\, \xi_m^{p}$
Where:
$\xi_m = \frac{tan\alpha}{\sqrt{\frac{2\pi H_s}{g T_m^2}}}$
$\xi_{cr} = (\frac{c_{pl}}{c_s} P^{0.31} \sqrt{tan\alpha})^{\frac{1}{P+0.5}}$
For $\xi_m<\xi_{cr}$ waves are plunging
For $\xi_m \geq \xi_{cr}$ waves are surging</td><td>$\boldsymbol{N}$: number of incident waves at the toe, which depends on the duration of the wave conditions.
$\mathbf{H_s}$: significant wave height, H1/3 of the incident waves at the toe of the structure (m).
$\boldsymbol{\xi_m}$: surf similarity parameter using the mean wave period, Tm (s), from time domain analysis.
$\boldsymbol{\xi_{cr}}$: critical value of the surf similarity parameter.
$\boldsymbol{\alpha}$: the slope angle (°).
$\boldsymbol{\Delta}$: relative buoyant density.
$\mathbf{D_{n50}}$: nominal diameter.
P: notional permeability of the structure.
$\mathbf{c_{pl}}$: 6,2
$\mathbf{c_s}$: 1</td></tr>
<tr><td colspan="2">**Conditions**: deep water (water level at the toe, i.e., $h > 3H_{s-toe}$)
NOTE: For slope angles gentler than 1:4 ($cot\alpha \geq 4$) only Equation for plunging waves should be used, irrespective of whether the surf similarity parameter, ξm, is smaller or larger than the transition value, ξ_{cr}. **(Rock Manual. CETMEF, 2007)**</td></tr>
</table>

The surf similarity parameter**ξ** has often been used to describe the form of wave breaking on abeach or structure. (Figure IV-2)

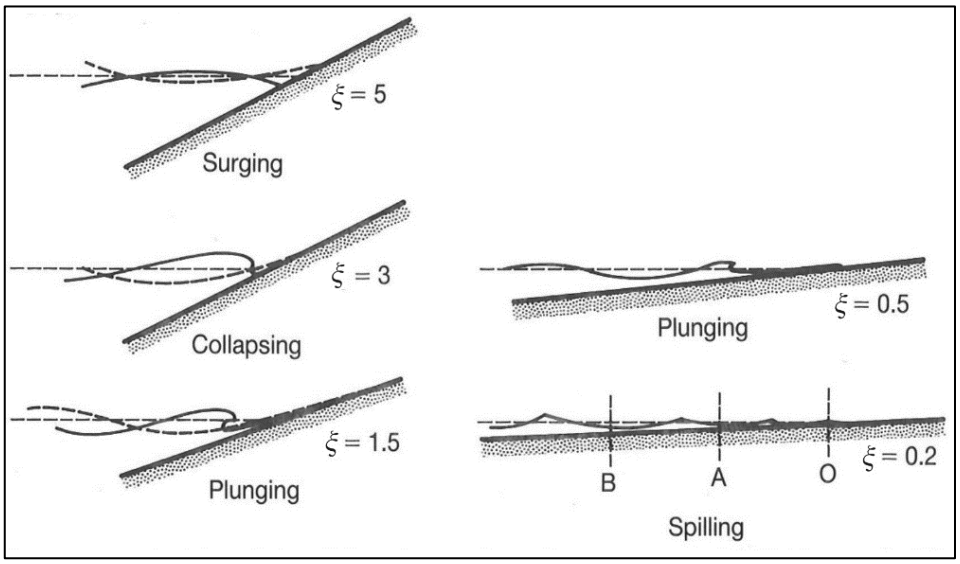

Figure IV-2 Breaker types as a function of the surf similarity parameter, ξ (Battjes, 1974).

The notional permeability (P) was empirically determined by Van der Meer for three different standard situations, to be exact the P=0.1, P=0.5 and P=0.6. The fourth one with a filter layer and a core is determined by interpolation of the tested configurations (P=0.4). The figure below shows these four standard situations (Kik R. and al 2012).

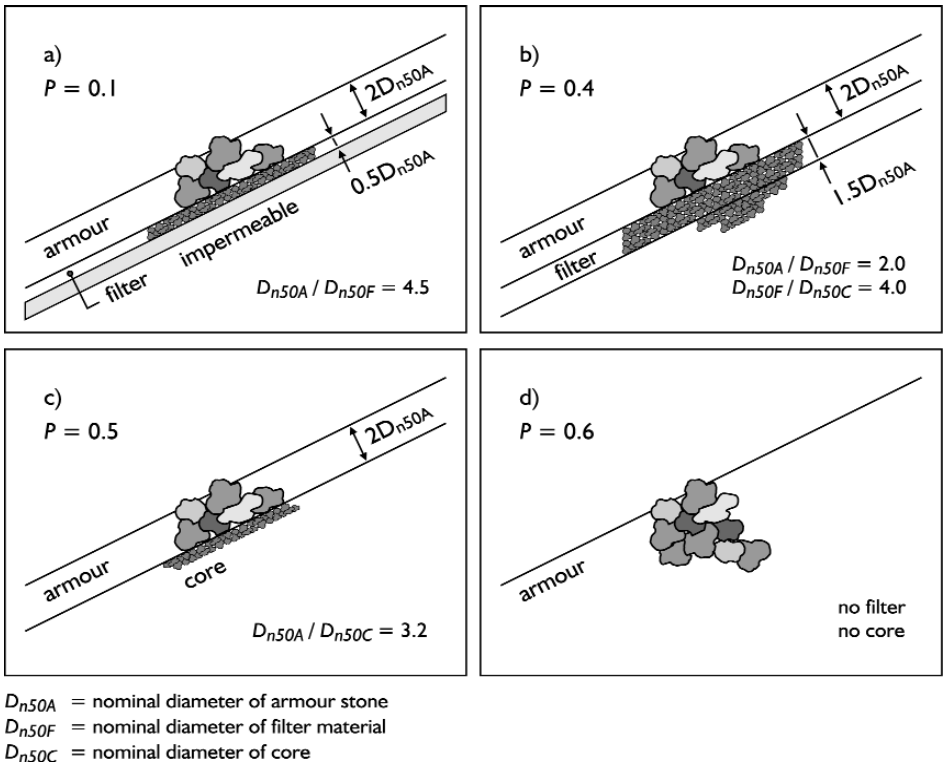

Figure IV-3 Notional permeability factor P for the formulae by Van der Meer (1988b)

shallow water conditions:

Table IV-4 Plunging and Surging Waves Van der Meer Formulae for shallow Water Conditions.

Van der Meer formulae	
shallow water	**Variables**
For plunging waves ($\xi_{s-1,0}<\xi_{cr}$): $\frac{H_s}{\Delta D_{n50}}= c_{pl}P^{0.18}(\frac{S_d}{\sqrt{N}})^{0.2}(\frac{H_s}{H_{2\%}})\xi_{s-1,0}^{-0.5}$ and for surging waves ($\xi_{s-1,0} \geq \xi_{cr}$): $\frac{H_s}{\Delta D_{n50}}= c_{pl}P^{-0.13}(\frac{S_d}{\sqrt{N}})^{0.2}(\frac{H_s}{H_{2\%}})\sqrt{cot\alpha}\xi_{s-1,0}^{p}$ where: $\xi_{s-1,0} =\frac{tan\alpha}{\sqrt{\frac{2\pi H_s}{gT_{s-1,0}^2}}}$ $\xi_{cr} = (\frac{c_{pl}}{c_s}P^{0.31}\sqrt{tan\alpha})^{\frac{1}{P+0.5}}$ For $\xi_{s-1,0}<\xi_{cr}$ waves are plunging For $\xi_{s-1,0} \geq \xi_{cr}$ waves are surging	$\boldsymbol{N}$: number of incident waves at the toe, which depends on the duration of the wave conditions. $\mathbf{H_s}$: significant wave height, H1/3 of the incident waves at the toe of the structure (m). $\boldsymbol{H_{2\%}}$: wave height exceeded by 2 per cent of the incident waves at the toe (m). $\boldsymbol{\xi_m}$: surf similarity parameter using the mean wave period, Tm (s), from time domain analysis. $\boldsymbol{\xi_{cr}}$: critical value of the surf similarity parameter. α: slope angle (°). Δ: relative buoyant density. P: notional permeability of the structure. $\boldsymbol{T_{s-1,0}}$: the (spectral) mean energy wave period (s). $\mathbf{c_{pl}}$: 8,4 $\mathbf{c_s}$: 1,3
Conditions: shallow water (water level at the toe, i.e., h < $3H_{s-toe}$) at which H_{s-toe}< 70 % of the deep-water wave height, H_{s0} (offshore significant wave height). **NOTE**: the locally determined values of H2% and $T_{m-1,0}$ should be used; a numerical wave propagation model.	

Geometric parameters of the armour stone

The geometric parameters of the armour stone in the design of coastal protection structures include the volume of a block, nominal diameter of the block, armour stone thickness, and the number of blocks per square meter. These parameters are determined based on the median mass of the armour stone and the layer coefficient.

Table IV-5: The formulas and variables used to calculate geometric parameters of the armorstone.

Formula	variables
Volume of a block: $V = \frac{M_{50}}{\rho_r}$	$\boldsymbol{M_{50}}$: the median mass of armour stone. $\boldsymbol{\rho_r}$: the apparent rock density (kg/m³). n: number of layers. $\boldsymbol{k_\Delta}$: layer coefficient.
Nominal diameter of bloc: $\boldsymbol{D_{n50} = \sqrt[3]{V}}$	
Armourstone thickness: $\boldsymbol{e = nk_\Delta D_n}$	
Number of blocks per square meter: $\boldsymbol{N_{s=}\frac{n}{D_n^2}}$	

Design of under-layer

The design of the under-layer involves determining the size and thickness of the smaller rocks or stones based on certain parameters. The formulas mentioned in the upcoming table are used to calculate the dimensions of the under-layer blocks. These dimensions include the median mass, volume, nominal diameter, and thickness.

Table IV-6 The formulas and variables used to calculate the dimensions of the under-layer

Formula	variables
The median mass of under-layer blocs: $\mathbf{M_{sc}} = \frac{\mathbf{M_{50}}}{\mathbf{10}}$	$\boldsymbol{M_{50}}$: the median mass of armourstone. $\boldsymbol{\rho_r}$: the apparent rock density (kg/m³). n: number of layers. $\boldsymbol{k_\Delta}$: layer coefficient.
Volume of a block: $\boldsymbol{V = \frac{M_{sc}}{\rho_r}}$	
Nominal diameter of bloc: $\boldsymbol{D_{n50} = \sqrt[3]{V}}$	
Armourstone thickness: $\boldsymbol{e = nk_\Delta D_n}$	
NOTE: the underlayer should normally not exceed 15% of the armour unit mass as accurate placement of armour units requires a relatively smooth surface of the underlayer. the underlayer armourstone (in mass) should not be less than 5 per cent of the armour unit mass in order to prevent armourstone material from being washed out through the pores of the armour layer. (Rock Manual. CETMEF, 2007)	

Design of transition filter and core

In coastal or shoreline structures, the transition filter and core are important components that play a crucial role in maintaining stability and protecting against erosion. They are typically placed between the armour layer and the underlying soil or sediment.

The design of the transition filter and core involves determining their masses based on the median mass of the armourstone.

Table IV-7 The formulas used to calculate the mass of the transition filtre and the core

Formulae	variables
The median mass of transition filter: $\boldsymbol{M_{sc50} = \frac{M_{50}}{200}}$	$\boldsymbol{M_{50}}$: the median mass of armourstone
Mass of core: $\boldsymbol{M_{n50} = \frac{M_{50}}{4000}}$	
NOTE: For the mass of the core and filter, we take a weight limited to 50% and 150%.	

Design of Toe bund:

The design of a toe bund involves careful consideration of various factors to ensure its effectiveness in protecting against wave forces and erosion. engineers take into account parameters such as the stability coefficient, slope angle, wave height at the toe, apparent density of the stone, and apparent water density. These parameters are utilized in specific formulas to calculate crucial dimensions.

Table IV-8 The formulas used to calculate the median mass, thickness and width of a toe bund

Formulae	variables
The median mass of bloc: $\boldsymbol{M_{b50} = \frac{0.1}{k_d}\left(\frac{\rho_r H_b^3}{\Delta^3 cot\alpha}\right)\frac{H_b}{d}}$	$\mathbf{K_d}$: stability coefficient. $\boldsymbol{\alpha}$: the slope angle. $\mathbf{H_b}$: wave height at the toe of the structure. $\boldsymbol{\Delta = \frac{\rho_r}{\rho_w} - 1}$: the relative density of the stone. $\boldsymbol{\rho_r}$: the apparent rock density (kg/m³). $\boldsymbol{\rho_w}$: the apparent water density (kg/m³). n: number of layers. $\boldsymbol{k_\Delta}$: layer coefficient.
Thickness and width of the armourstone: $\boldsymbol{e, l = nk_\Delta \sqrt[3]{\frac{M_b}{\rho_r}}}$	

The different types of blocks used in Algiers Port and Marina

In Algiers Port and Marina, different types of blocks are utilized for construction and stabilization purposes. Each type of block is selected based on its specific characteristics and intended application within the port and marina.

Table IV-9 Characteristics of Blocks Used in Algiers Port and Marina

Blocks	Shapes	Characteristics
Naturel block		$\mathbf{K_d}$stability coefficient: Current section: 4; Roundhead: 3.8 apparent rock density: ρ: 2.65 t/ m³
Grooved cube (antifer type)		$\mathbf{K_d}$stability coefficient: Current section: 6.8; Roundhead: 5 apparent rock density: ρ: 2.4 t/ m³
Parallelepiped block	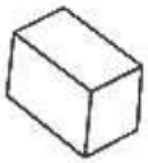	$\mathbf{K_d}$stability coefficient: Current section:8; Roundhead: 6 apparent rock density: ρ: 2.4 t/ m³
Cubipod	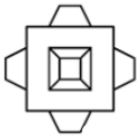	$\mathbf{K_d}$stability coefficient: Current section: 28; Roundhead: 7 apparent rock density: ρ: 2.4 t/ m³

IV.4. Results of the design calculations:

The results obtained in Table IV-10 for the Marina and in Table IV-11 for the Port highlight the use of different formulas for each type of riprap and each part of the jetty during these calculations. To facilitate comparison, the Hudson and Van der Meer formulas are used for the same types of armor and the same wave height at the base of the structure.

Van der Meer's formula suggests an increase of approximately 70% in the block mass compared to the results obtained with Hudson's formula for the armor layer. For example, in the Marina's main jetty, the average block mass for the trunk armor layer calculated using Hudson's formula is 1.6 t, while Van der Meer's formula yields an average block mass of 3.6 t. This increase is due to Van der Meer considering more variables that could influence the stability of the breakwater.

It should be noted that the results obtained for the head of the main jetty confirm those obtained for the current section. However, the dimensions of the under-layer and core are not significantly affected by the results of the armor layer obtained with each formula.

The application of Van der Meer's formula provides a higher level of stability against wave actions compared to the results obtained with Hudson's formula. For instance, in the Khireddine jetty, the average block mass for current section armor layer calculated using Hudson's formula is 11.4 t, while Van der Meer's formula yields a significantly higher value of 20 t. Furthermore, it is important to highlight that the obtained results are consistent with those obtained in the previous chapter, where the weight of the blocks constituting Khireddine jetty is higher than that of the blocks constituting the main jetty of Marina. This is due to the fact that Marina is naturally protected against wave impacts.

In summary, the calculations using Van der Meer's formula indicate a higher level of stability and require larger block masses compared to those obtained with Hudson's formula. These results demonstrate the importance of considering additional variables in the design process, especially for critical structures like breakwaters.

Table IV-10 Summary of Calculations for the Design of Marina's Main Jetty.

Block type		**Naturel rock**		**Cubipod**	
Part in the main jetty		**Trunk**		**Current section**	**Roundhead**
Design Wave (m)		2.34		5	
Formula used		Hudson	Van Der Meer	Hudson	
Armor Layer	Average Block Mass (t)	1.6	3.6	2.9	11.96
	Layer Thickness (m)	1.9	2.6	2.37	3,76
under-layer	Average Block Mass (t)	0.16	0.36	0.29	1.2
	Layer Thickness (m)	0.9	1.18	1.11	1.76
Core	Weight of TVC materials (t)	< 0.1			
Toe bund	Average Block Mass (t)	1.81			
	Thickness and Length (m)	2.03			

Table IV-11 Summary of Calculations for the Main Jetty Design at Khireddine Port in Algiers.

Block type		**Parallelepiped**		**Grooved cube (antifer type)**			
Part in the main jetty		**Trunk**		**Current section**		**Roundhead**	
Design Wave (m)		3.82		4.88		5.9	
Formula used		Hudson	Van Der Meer	Hudson	Van Der Meer	Hudson	Van Der Meer
Armor Layer	Average Block Mass (t)	4.7	9.7	11.4	20	27.5	35
	Layer Thickness (m)	2.75	3.5	3.86	4.31	4.96	5.2
under-layer	Average Block Mass (t)	0.47	0.97	0.114	2	2.75	3.5
	Layer Thickness (m)	1.29	1.64	1.74	2.09	2.33	2.52
Core	Weight of TVC materials (t)	< 0.1					
Toe bund	Average Block Mass (t)	6.3					
	Thickness and Length (m)	3					

IV.5. Conclusion

In conclusion, the comparison of design calculations using the Hudson and Van der Meer formulas for rubble mound breakwaters has provided important insights for the design of the main jetty of Marina and Khireddine Port in Algiers. It is worth noting that the weight of the blocks in Khireddine Port's jetty is higher than that of Marina's due to the natural protection provided by the location. This study emphasizes the significance of considering the specific characteristics of the study area and selecting appropriate design formulas to ensure effective and resilient breakwater designs. Further research and validation of these findings are necessary to enhance the understanding and application of design methodologies for rubble mound breakwaters.

Chapter V. Hydraulic performance

V.1. Introduction

The interaction between rubble mound breakwaters and waves has been the subject of intensive research. The majority of experimental studies have concentrated on the estimation of the hydraulic responses of breakwaters based on the main hydrodynamic parameters representing the wave and structure characteristics. The main concern was to propose optimizations leading to a better hydraulic stability. This chapter will examine the various hydraulic responses exerted on the structures.

The important hydraulic interactions between waves and hydraulic structures are wave Run-up, wave Run-down, Overtopping, transmission and reflection, illustrated in Figure V-1 (CETMEF,2009). These interactions play a significant role in our case study, we will focus on Run-up, wave Run-down and Overtopping.

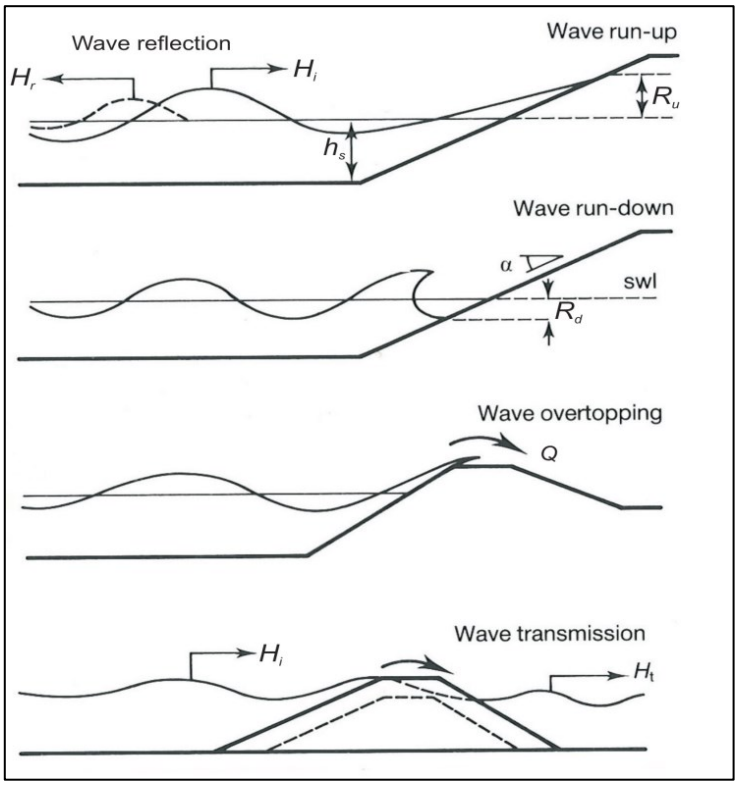

Figure V-1 Hydraulic interactions related to waves and governing parameters (CETMEF, 2009).

Table V-1 shows the wave parameters (derived from modeling) specific to the scenarios considered for the calculation of the hydraulic performance of the main dike in the marina of Algiers, including:

- β: Angle of incidence of the wave with respect to the normal in degrees.
- H_{mo}: Calculated using the formula proposed by Kamphuis (2001) for estimating the significant wave height for long waves at the structure.

$$\frac{(H_{m0})}{H_{s,b}} = 0.11\left[\frac{H_{s,b}}{g\,T_P^2}\right]^{-0.24} \qquad \textbf{Equation V-1}$$

where $H_{\mathrm{s,b}}$: the significant wave height at the breaking point.

Table V-1 Wave Parameters for Return Periods in Algiers Marina and Port

Study area	Penalizing direction	Return period (year)	Hs (m)	Hmo (m)	Tp (s)	Tm0 (s)
Marina	NNE	2	1.97	0.9	8.74	6.64
		10	2.21	1.12	11.4	8.66
		50	2.24	1.13	11.48	8.72
		100	2.30	1.18	11.99	9.11
Port	NNE	2	3.37	1.36	8.76	6.66
		10	3.88	1.72	11.43	8.69
		50	4.16	1.82	11.51	8.75
		100	4.28	1.89	12.01	9.13

V.2. Run-up

Wave Run-up is defined as the extreme level of the water reached on a structure slope by wave action. Prediction of run-up, R_u, may be based on simple empirical equations obtained from model test results, or on numerical models of wave/structure interaction. All calculation methods require parameters to be defined precisely. Run-up is defined vertically relative to the still water level (SWL) and will be given positive if above SWL (CETMEF,2009), as shown in Figure V-1.

Unlike regular waves, which result in a single value of maximum wave run-up, irregular waves produce a run-up distribution. This necessitated the run-up formulae determining are presentative parameter of the wave run-up distribution. The most common irregular wave run-up parameter is $R_{u2\%}$ (CETMEF,2009).

The general relationship between the 2 per cent run-up level, $R_{u2\%}$ and the slope angle (through tanα in ξ)and the wave height and periods is presented in Equation V-2

$$\frac{R_{u2\%}}{H_s} = A\xi + B$$ **Equation V-2**

Where:

$R_{u2\%}$: the run-up exceeded by 2% of waves.

ξ : the surf similarity parameter, also known as the Iribarren number $\xi = \frac{\tan\alpha}{\sqrt{s_0}}$

s_0 : the fictitious wave steepness. $s_0 = \frac{H}{L_0} = \frac{2\pi}{g}\frac{H}{T^2}$

$H\ (m)$: the local wave height.

L_0 : the theoretical wavelength of the offshore wave.

T : the period of wave.

TAW (2002a) presents equations for the determination of wave run-up in which the breaker parameter, $\xi_{\mathrm{m}-1,0}$, is applied, calculated by using the spectral significant wave height ($H_s = H_{m0}$)

Table V-2 TAW (2002) Approach Equations for Calculating Wave Run-Up2%

Formulae	Parameters
For the mean energy wave period,$T_{\mathrm{m}-1,0}$: $\frac{R_{u2\%}}{H_{m0}} = A\gamma_b\gamma_f\gamma_\beta\xi_{\mathrm{m}-1,0}$ And with a maximum or upper boundary for larger values of $\xi_{m-1,0}$ of: $\frac{R_{u2\%}}{H_{m0}} = \gamma_f\gamma_\beta(B - C/\sqrt{\xi_{\mathrm{m}-1,0}})$	H_{m0}: the spectral significant wave height. γ_b: the berm factor. γ_f: the roughness factor. γ_β: the correction factor for oblique waves. $\xi_{\mathrm{m}-1,0}$: the breaker parameter where: $\xi_{\mathrm{m}-1,0} = \frac{\tan\alpha}{\sqrt{s_{\mathrm{m}-1,0}}} = \frac{\tan\alpha}{\sqrt{\frac{2\pi}{g}\frac{H_s}{T^2_{\mathrm{m}-1,0}}}}$ $T_{\mathrm{m}-1,0}$: the mean energy wave period. H_s: the significant wave height at the toe of the structure. g: acceleration of Gravity.

The values for coefficients A, B and C in the two equations above that are presented in Table V-3

Table V-3 The values for coefficients A, B and C in the two TAW (2002a) equations

Coefficients	Values with safety margin	Values without safety
A	1.75	1.65
B	4.3	4.0
C	1.6	1.5

Run-up Calculation Results

The results of the Run-up level that the dikes will have to face according to the different wave scenarios defined are presented in Table V-4 for Marina Algiers Case and Table V-5 for Port Algiers Case.

In the proximity of the marina, the run-up of the majority of waves breaking on the dike slope (Ru2%) varies between 3.12 m and 3.76 m; for the same conditions, some waves can reach a run-up height (Ru99/100%) varying between 4.81and 5.79 m. The variation in run-up under these conditions between Ru2% and Ru99/100% averages about 1.98 m. It can also be seen that all waves have a run-up height lower than the level of the current section, which is 6 m.

In the Port of Algiers, near the Khireddine jetty, the run-up of most waves breaking on the dike slope (Ru2%) varies between 5.03 m and 6.69 m. For the same conditions, some waves can reach a run-up level (Ru99/100%) between 7.75 m and 10.31 m. On average, the run-up range under these conditions, between Ru2% and Ru99/100%, is 3.28 m.

It can also be seen that all waves have a submersion level below the level of the current section, which is 8.5m.

Table V-4 Run-up Calculation Results for Algiers Marina Case

Return period (year)	H_{mo} (m)	A	B	Ru2% (m)	Ru99/100% (m)	Extent Run-up (m)
2 years	0.90	-0.20	4.50	3.12	4.81	1.69
10 years	1.12	-0.20	4.50	3.60	5.55	1.95
50 years	1.13	-0.20	4.50	3.65	5.62	1.97
100 years	1.18	-0.20	4.50	3.76	5.79	2.03

Table V-5 Run-up Calculation Results for Algiers Port Case

Return period (year)	H_{mo} (m)	A	B	Ru2% (m)	Ru99/100% (m)	Extent Run-up (m)
2 years	1.36	-0.20	4.50	5.03	7.75	2.72
10 years	1.72	-0.20	4.50	6.07	9.34	3.28
50 years	1.82	-0.20	4.50	6.47	9.96	3.49
100 years	1.89	-0.20	4.50	6.69	10.31	3.61

V.3. Run-Down

The Run-down is often less important compared to the wave run-up. it defined asthe lower extreme water level reached by a wave on a sloping structure is known as wave run-down, *Rd*. Run-down is defined vertically relative to SWL and will be given as positive if below SWL(CETMEF,2009). as shown in Figure V-1.

Run-down can be calculated with formulas in Table IV-8

Table V-6 Formulas for Calculating Wave Run-Down

Formulas	Paramaters
On straight smooth slopes: $\frac{R_{d2\%}}{H_s}$=0.33ξ_p for 0<ξ_p<4 $\frac{R_{d2\%}}{H_s}$=1.5 forξ_p ≥4	$R_{d2\%}$: the run-down exceeded by 2% of waves. $R_{d1\%}$: the run-down exceeded by 1% of waves. H_s : Significant wave height at the toe of the structure. ξ_p : breaker parameter based on s_p P : notional permeability of the structure. s_{om}: wave steepness with Lo, based on Tm T_m : the mean energy wave period. α : the slope angle (°).
On porous rubble slopes: By Thompson and Shuttler (1975): $\frac{R_{d1\%}}{H_s}$=0.34ξ_p −0.17 By Van der Meer (1988b) : $\frac{R_{d2\%}}{H_s}$=2.1$\sqrt{tan\alpha}$ − 1.2$P^{0.15}$+1.5 $e^{(-60s_{om})}$	

Run-down Calculation Results

The results from Table V-7 and Table V-8 show that on average, the run-down height for the Marina is 1.63 m, while it is 2.5 m for the Port. Considering that the toe of the main dike in the Marina is located at a depth of 3 m, and the toe of the Khireddine jetty is at a depth of 10 m, we can observe that for both main dikes, all run-down heights remain below the toe level ensuring their protection.

By calculating the minimum extensions, we were able to identify the specific areas where wave forces are exerted. It is noteworthy that the Marina's dikes typically experience wave forces within a range of 6.2 m, whereas the port's dikes encounter forces over a distance of approximately 10.4 m.

The cumulative impact of these forces and their application may pose risks to the stability of the structure, primarily manifesting as internal erosion of the dike.

Table V-7 Run-down Calculation Results for Algiers Port Case

Return period (year)	H_{mo} (m)	T_p (s)	ξ_p	Rd2% (m)	E (m)
2 years	1.36	8.76	3.98	2.04	8.50
10 years	1.72	11.43	4.83	2.58	10.39
50 years	1.82	11.51	4.70	2.72	11.05
100 years	1.89	12.01	4.84	2.84	11.46

Table V-8 Run-down Calculation Results for Algiers Marina Case

Return period (year)	H_{mo} (m)	T_p (s)	ξ_p	Rd2% (m)	E (m)
2 years	0.90	8.74	5.19	1.35	5.38
10 years	1.12	11.40	6.39	1.68	6.35
50 years	1.13	11.48	6.39	1.70	6.43
100 years	1.18	11.99	6.59	1.77	6.65

V.4. Overtopping

The overtopping discharge is mostly related to the wave run-up, which represent the average amount of water that is discharged per linear meter by waves over a protection structure (e.g., breakwater, dike) whose crest is higher than the still water level (SWL). (Dan S. et al 2020). usually expressed as a specific discharge per meter run along the crest, q (m^3/s per m length or l/s per m length). (CETMEF, 2009).

Table V-9 The mean overtopping discharge and damage to rubble mounds breakwaters established by (Allsop et al, 2005).

Risks and damages	q mean overtopping discharge (m^3 /s per m length)
Unsafe for unaware pedestrians, no clear view of the sea, relatively easily upset or frightened, narrow walkway or proximity to edge	$q > 3\times 10^{-5}$
Unsafe for aware pedestrians, clear view of the sea, not easily upset or frightened, able to tolerate getting wet, wider walkway	$q > 1\times 10^{-4}$
Unsafe for trained staff, well shod and protected, expected to get wet, overtopping flows at lower levels only, no falling jet, low danger of fall from walkway	$q > 1\times 10^{-3}$- 0.01
Sinking of small boats set 5–10 m from wall, damage to larger yachts	$q > 0.01$
Significant damage or sinking of larger yachts	$q > 0.05$
No damage	$q < 2\times 10^{-3}$
Damage if crest not protected	$2\times 10^{-3} < q < 0.02$
Damage if back slope not protected	$0.02 < q < 0.05$
Damage even if fully protected	$q > 0.05$

Overtopping can be analyzed in different empirical formulae or by physical and numerical models. they're conditioned by the wave climate and the geometry of the structure.

Mean overtopping discharge, q, is function of the parameters below:

$$q = F(H_s ; T ; \beta; R_c; h ; g) \qquad \textbf{Equation V-3}$$

Where:

H_s : the significant wave height at the toe of the structure.
T : the mean wave period at the toe of the structure.
β : the angle wave attack.
R_c : the crest freeboard of structure.
h : the water depth at toe of structure.
g : the acceleration due to gravity.

In general, mean overtopping discharge is expressed by two typical forms shown in equations below, **A** and **B** are tabled coefficients that vary depending on the geometry of the structure. Overtopping discharge and freeboard are described by the dimensionless parameters **Q** and $\boldsymbol{R_c}$, respectively.

$$q = A \exp(BR_c) \qquad q = AR^{-B} \qquad \textbf{Equation V-4}$$

Table V-10 Formulas for Calculating mean overtopping discharge q

Formulas	Parameters
Owen's method (1980): $\frac{q}{gH_sT_m} = aexp(-b\frac{R_c}{H_s}\sqrt{\frac{s_0}{2\pi}}\frac{1}{\gamma_f})$	q: mean overtopping discharge. R_c : crest freeboard of structure. g: acceleration due to Gravity. s_0 : the fictitious wave steepness. T_m : the mean energy wave period. $\xi_{m-1,0}$: breaker parameter based on$s_{m-1,0}$ ξ_m : breaker parameter based on s_m H_{m0} : Significant wave height from the spectral analysis. H_s : Significant wave height at the toe of the seawall. γ_b: the berm factor. γ_f: the roughness factor. γ_β: the correction factor for oblique waves. γ_v: correction factor for a vertical wall on the slope.
TAW method (2002a): For breaking waves ($\gamma_b \cdot \xi_{m-1,0} \leq 2$): $\frac{q}{\sqrt{gH_{m0}^3}} = \frac{A}{\sqrt{\tan\alpha}}\gamma_b\xi_{m-1,0}\exp(-B\frac{R_c}{H_{m0}}\frac{1}{\xi_{m-1,0}\gamma_b\gamma_f\gamma_\beta})$ with a maximum (for non-breaking waves generally reached when $\gamma_b \cdot \xi_{m-1,0} \geq 2$): $\frac{q}{\sqrt{gH_{m0}^3}} = Cexp(-D\frac{R_c}{H_{m0}}\frac{1}{\gamma_f\gamma_\beta})$	
EurOtop (2007): $\frac{q}{\sqrt{gH_s^3}} = \frac{0.067}{\sqrt{\tan\alpha}} \cdot \gamma_b \cdot \xi_m \exp(-4.75\frac{R_c}{\xi_m H_s \gamma_b\gamma_f\gamma_\beta\gamma_v})$	

Results of calculations

Table V-11 and Table V-12 show the results of overtopping discharge on the main dikes.

In the case of Marina Algiers, for the 2-year return period, overtopping by pulsating flows at low levels can only be dangerous when occur at low speed; this overtopping of waves presents no risk to Pedestrians, but could cause sinking of small boats moored 5-10 meters from the breakwater, and some damage to larger boats, and may also cause damage to sloped dikes if the rear berm is unprotected. For periods ranging from 10 to 100 years, overtopping could be dangerous for dikes with slopes, causing damage even if the protection is complete, and could cause major damage to larger boats, even shipwreck.

Table V-11 Overtopping discharge Calculation Results for Algiers Marina Case

Return period (year)	Rc (m)	ξ_m	H_s (m)	q ($m^3/s/m$)
2 years	6	3.94	1.97	0.071
10 years	6	4.85	2.21	0.29
50 years	6	4.86	2.24	0.30
100 years	6	5.01	2.30	0.38

In the case of Port Algiers, for the 2-year return period, overtopping by pulsating flows at low levels only could be dangerous when carried out at low speed; it could result in the sinking of small boats moored 5-10 meters from the wall, and some damage to larger boats, and may also cause damage to sloped dikes if the back slope is not protected. However, this wave overflow does not present a risk to Pedestrians.

For return periods of 10 to 100 years, wave overtopping could be dangerous for sloped dikes, causing damage even if protection is complete. The overtopping results obtained for the different wave scenarios show that, from a structural point of view, the main dikes are fairly resistant to overtopping, which poses no major risk to their structural stability in the face of the sea's hydraulic forces, since the values are relatively low.

Table V-12 Overtopping discharge Calculation Results for Port Algiers Case

Return period (year)	Rc (m)	ξ_m	H_s (m)	q ($m^3/s/m$)
2 years	8.5	3.02	3.37	0.09
10 years	8.5	3.67	3.88	0.42
50 years	8.5	3.57	4.16	0.51
100 years	8.5	3.68	4.28	0.64

V.5. Conclusion

The calculations conducted in this chapter demonstrate that the current sections of the main dikes in Marina and Port of Algiers are sufficiently well protected and capable of withstanding various extreme conditions. It can also be concluded that the results for overtopping on rubble mound breakwater are consistent, confirming their resistance and low risk to stability against hydraulic forces from the sea.

In the next chapter, we will explore a new approach for calculating overtopping. This method will be based on real tests conducted by multiple laboratories on various sloping dikes.

Chapter VI. Machine Learning

VI.1. Introduction

Machine Learning (ML) is a subfield of Artificial Intelligence (AI) that enables machines to learn from data without explicit programming, similar to how humans learn. Its objective is to develop models capable of solving problems by identifying underlying correlations within data, thereby facilitating accurate predictions. Through ML, data processing enables the identification of correlations across diverse aspects, enabling the system to anticipate their likely consequences. The utilization of machine learning techniques has gained significant traction across various engineering domains, including coastal engineering.

VI.2. Machine Learning

The steps below represent the general ones for creating a machine learning model. The workflow is illustrated in the Figure VI-1.

1. Definition of the problem.
2. Data Gathering.
3. Data Preparation.
4. Model Selection.
5. Model Training.
6. Model evaluation.
7. Model Deployment
8. Model monitoring and maintenance.

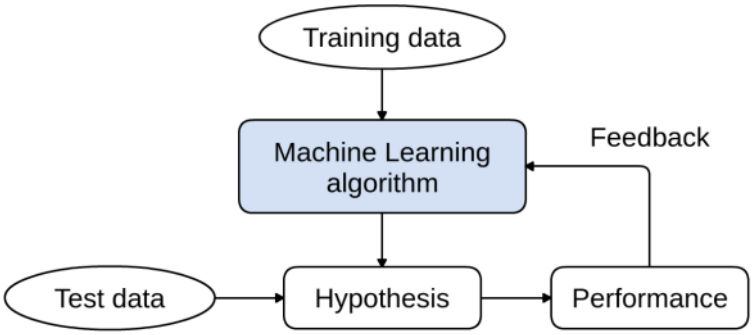

Figure VI-1 Machine Learning workflow diagram

There are two main classes of machine learning supervised and unsupervised. The difference between them lies in the way they are trained and the types of data they are used for. The first one is based on labeled data, while the second one is based on unlabeled data.

VI.2.1. Supervised Learning

In supervised learning, the algorithm is trained on labeled data, where the correct output is provided for each input. The goal of supervised learning is to learn a function that can accurately map inputs to outputs based on the labeled data. There are three main types of supervised Learning:

- **Classification:** This involves predicting a categorical label or class for new input data based on the patterns learned from labeled data.
- **Regression:** This involves predicting a continuous numerical output for new input data.
- **Forecasting:** This is a special type of regression where the focus is on predicting values over time.

VI.2.2. Unsupervised Learning

The unsupervised learning algorithm trained on unlabeled data where the correct output is not provided. The goal of unsupervised learning is to discover patterns or relationships in the data without any prior knowledge of what the patterns might be. Clustering and dimensionality reduction are common tasks in unsupervised learning.

VI.3. Supervised Learning algorithms

There are several popular machine learning algorithms that are commonly used in supervised learning. Here are some of the most common ones.

VI.3.1. Linear regression

Linear regression is a supervised learning algorithm used for predictive modeling. It involves finding a linear relationship between the dependent variable and the independent variables. It fits a straight line to the data points, minimizing the distance between the predicted values and the actual values. The general formula for linear regression is shown on the Table VI-2

Table VI-1 Machine learning terminology

$y = f(\boldsymbol{x})$		
Symbol	***Math***	***Machine Learning***
y	Dependent variable	Target (Predicted variable)
$f(\cdot)$	Function	Model (Hypothesis)
$\boldsymbol{x}$	Independent variables	Features

Table VI-2 Linear regression formula

$y = w_1x_1 + w_2x_2 + b$		
Symbol	***Math***	***Machine Learning***
w	Slopes	Weights
b	Intercept	Bias
$[w, b]$	Coefficients	Parameters

VI.3.2. Polynomial regression

Polynomial regression extends the concept of linear regression and allows for the modeling of nonlinear relationships between variables. In polynomial regression, the relationship between the dependent variable and the independent variables is expressed as an nth degree polynomial equation. Although the equation itself is nonlinear, polynomial regression can be treated as a linear problem by transforming the features appropriately.

Table VI-3 presents an example of a second-order polynomial regression model with two features, illustrating how polynomial regression can be applied to capture complex relationships between variables.

Table VI-3 Example of converting a polynomial problem to a linear regression

Example: 2 features with a second order polynomial

$$y = \omega_0 + \omega_1x_1 + \omega_2x_2 + \omega_3x_1x_2 + \omega_4x_1^2 + \omega_5x_2^2$$

$$\Longrightarrow y = \omega_0 + \omega_1x_1 + \omega_2x_2 + \omega_3x_3 + \omega_4x_4 + \omega_5x_5$$

Where:

$x_3 = x_1x_2; x_4 = x_1^2; x_5 = x_2^2;$

So, a second polynomial problem of two features become a linear problem of five features.

VI.3.3. Decision Trees

The construction of a Decision Tree involves the creation of a tree-like model to predict and classify data. It begins with a single node known as the root node, which represents the entire dataset (Figure VI-2). The algorithm then evaluates the available features and selects the most informative one to split the data into two or more branches. This splitting process is repeated recursively for each resulting branch, creating additional nodes and branches until a stopping criterion is met. The stopping criterion could be reaching a maximum depth, achieving a minimum number of samples in a leaf node, or reaching a specific level of impurity reduction. At each node, the algorithm makes decisions based on the selected features, aiming to maximize the separation of classes or minimize impurity. The construction process continues until all the data is accurately classified or until the stopping criterion is satisfied.

VI.3.4. Random Forest

Random Forest is a powerful supervised learning algorithm utilized for various tasks such as classification, regression, and more. It functions by constructing multiple decision trees during the training phase. The algorithm's essence lies in creating an ensemble of decision trees Figure VI-2, forming a forest. This implies that numerous trees contribute to the forest's creation, serving as the fundamental principle behind the random forest algorithm. The prediction is determined by aggregating the predictions of all the trees.

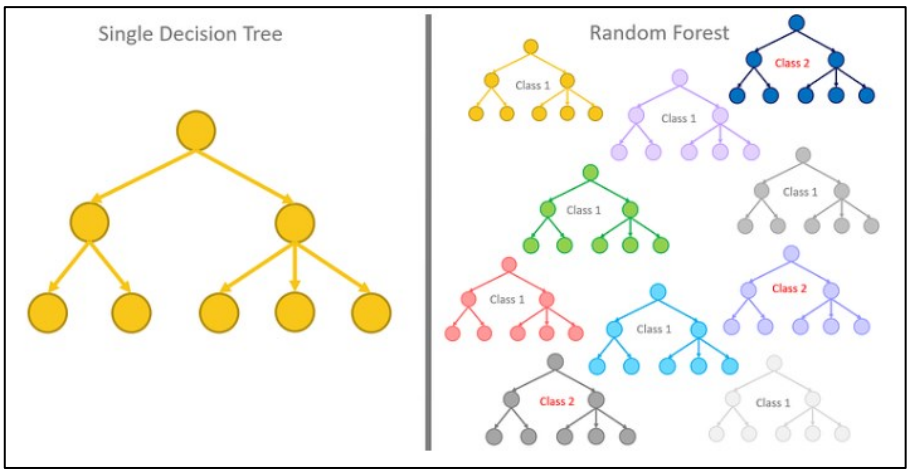

Figure VI-2 The random forest algorithm relies on multiple decision trees that are all trained slightly differently.

VI.3.5. Gradient Boosting

Gradient Boosting Machines, or GBMs for short, are classified as sequential ensemble models, meaning they build predictive models by combining multiple weak learners in a sequential manner. GBMs excel in various tasks such as regression, classification, and ranking, and are highly favored by data scientists and practitioners due to their ability to boost model accuracy and performance.

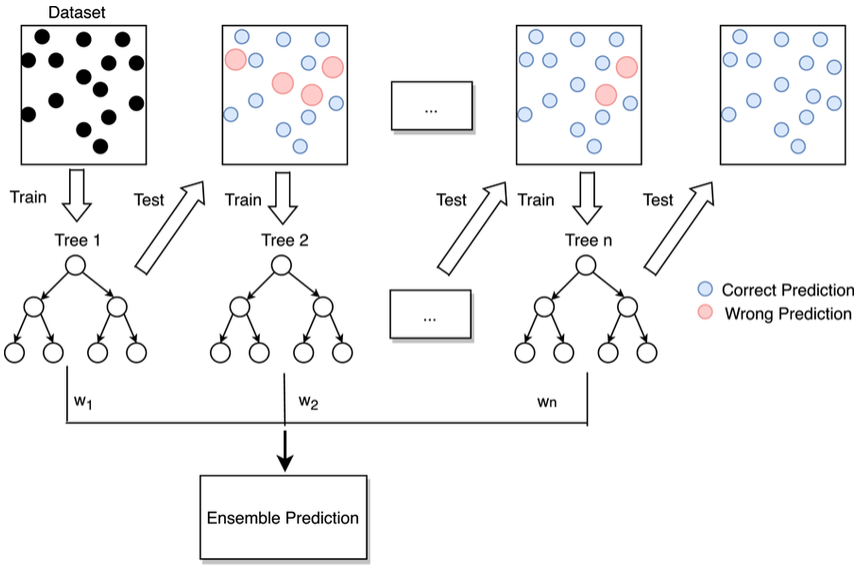

Figure VI-3 Flow diagram of gradient boosting machine learning method.

VI.3.6. Extreme Gradient Boosting (XGBoost)

Much like the previously discussed Random Forest algorithm in our study, Gradient Boosting is an ensemble technique that constructs the final model by combining a series of weak learners, primarily decision trees. By utilizing the gradient, it aims to minimize the loss function, which bears resemblance to how gradient descent optimizes weights in deep learning (neural networks). XGBoost, as a gradient boosting algorithm, takes into account more precise estimates when determining the accuracy of models Figure VI-4.

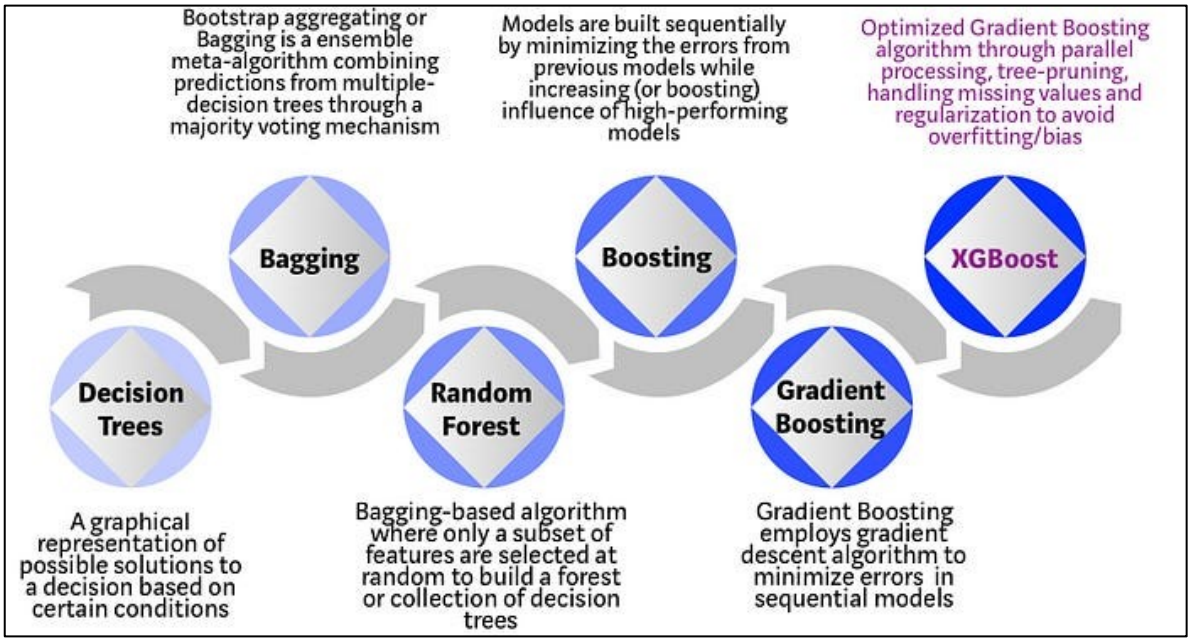

Figure VI-4 Evolution of XGBoost Algorithm from Decision Trees.

VI.3.7. Artificial Neural Networks

Artificial Neural Networks (ANN) are a powerful class of machine learning algorithms that have gained popularity due to their ability to model complex patterns and relationships in data. They draw inspiration from the structure and function of biological neural networks found in the human brain. ANN typically consist of three types of nodes: input nodes, hidden layer nodes, and output nodes.

The input nodes are responsible for receiving various input features. These features could be numerical values or categorical variables. Each input node represents a specific feature, and the values assigned to these nodes act as the initial information fed into the network.

The output nodes represent potential results or predictions based on the input data. These nodes provide the final output of the network, which could be in the form of a classification or regression task. The number of output nodes depends on the specific problem being solved.

The hidden layer nodes serve as intermediaries between the input and output nodes. These nodes are responsible for merging the inputs and transforming them into a higher-dimensional

representation that captures complex relationships and patterns within the data. Each hidden layer typically consists of multiple nodes, and the number of hidden layers can vary depending on the complexity of the problem. The information flow through the hidden layers allows the network to learn and extract meaningful features from the input data.

The connections between nodes in an ANN are represented by weights. These weights determine the strength and direction of the signal transmitted between nodes. During the training process, the network adjusts these weights iteratively based on the available input-output pairs.

Activation functions in Artificial Neural Networks (ANN) are crucial for introducing non-linearity and enabling complex decision-making. They determine the output of nodes or neurons based on the weighted sum of inputs, adding flexibility and adaptability to the network. Popular activation functions include the sigmoid function for binary classification, the rectified linear unit (ReLU) for efficient learning and addressing the vanishing gradient problem, and variants like Leaky ReLU and PReLU. Other functions like tanh and softmax also find applications in ANNs. The choice of activation function depends on the problem and desired behavior of the network, allowing ANNs to effectively model intricate relationships in data and achieve higher performance across various domains of machine learning and artificial intelligence.

In conclusion, Artificial Neural Networks are a type of machine learning algorithm that mimic the structure and function of biological neural networks. By utilizing input nodes, hidden layer nodes, and output nodes, they can learn complex patterns and relationships in data. ANN have become a fundamental tool in the field of machine learning, enabling the development of intelligent systems capable of making predictions and decisions (Axelsson T. 2018).

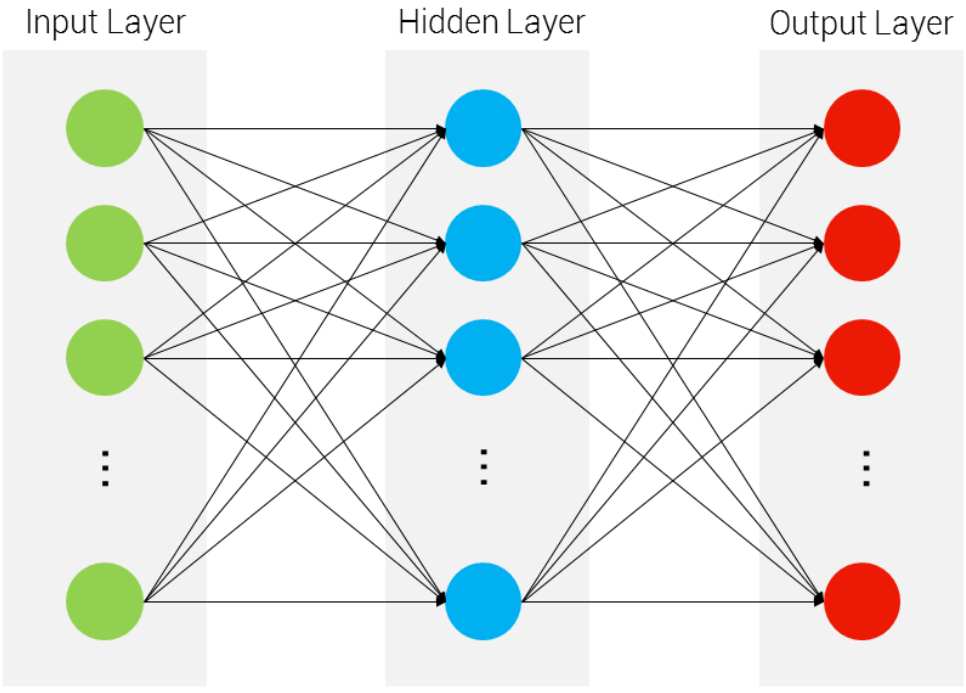

Figure VI-5 Articificial Neural Network Architecture.

VI.4. Description of the database

The CLASH (Crest Level Assessment of Coastal Structures by full scale monitoring, neural network prediction and Hazard Analysis on permissible wave overtopping) database is a comprehensive collection of data on wave overtopping of coastal structures that was developed as part of the CLASH project. One of the main objectives of this project was to develop a prediction model for wave overtopping on a wide variety of coastal structures (De Rouck et al. 2002). This database consists of measurements collected from various laboratories worldwide and is described in detail in Verhaeghe et al. (2003) and Steendam et al. (2004). The database contains 10,532 entries, each described by 31 parameters. These parameters are divided into three groups: 3 general parameters, 11 hydraulic parameters, and 17 structural parameters. The records have also been evaluated in terms of reliability factor (RF) and complexity factor (CF). The RF values range from 1, indicating all parameters are available and tests are highly reliable, to 4, indicating unreliable tests with unacceptable parameter estimates and high uncertainty. Similarly, the CF is assigned based on the complexity of the tested structure, ranging from 1 for "very simple" structures to 4 for "very complex" structures that cannot be precisely described by the chosen parameters.

Contents of the database

In order to describe the characteristics of the wave field, three parameters have been taken into account: the significant wave height at the base of the structure (H_{m0}) determined through spectral analysis, the average wave period at the base of the structure ($T_{\mathrm{m-1,0}}$) also obtained from spectral analysis, and the direction of wave attack (E). Concerning the geometric configuration of the structure, twelve parameters have been considered: the water depth in front of the structure (h), the water depth at the base of the structure (h_t), the width of the base berm (B_t), the structure's roughness or permeability (γ_f), the slope of the structure below the berm ($\cot \alpha$d), the slope of the structure above the berm ($\cot \alpha$u), the width of the berm (B), the water depth on the berm (h_b), the slope of the berm ($\tan \alpha$B), the vertical distance between the crest and the water level (R_c), the vertical distance between the armor crest and the water level (A_c), and the width of the crest (G_c). Figure VI-6 illustrates the fifteen parameters utilized as input for the NN model.

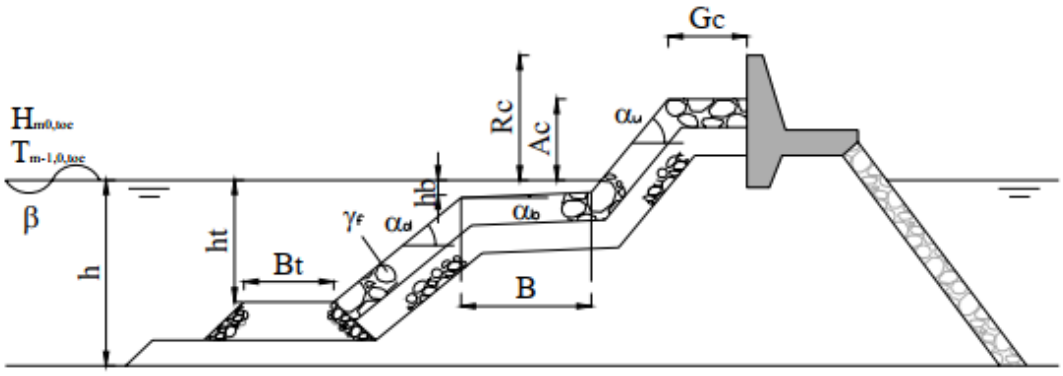

Figure VI-6 Feature definitions, adapted from Van Gent et al. (2007).

Table VI-4 General, hydraulic, and structural parameters are included in the database.

No	Parameter	Min.	Max.	Description
				General parameters
1	Name			This parameter assigns a unique name to each test. It is just meant to recognize each test but has no further meaning.
2	RF [-]	1	4	The 'Reliability Factor' gives an indication of the reliability of the test. It can adopt the values 1, 2, 3 or 4.
3	CF [-]	1	4	This parameter, called the 'Complexity Factor' gives an indication of the complexity of the test structure. It can adopt the values 1, 2, 3 or 4.
				Hydraulic parameters
4	$H_{\mathrm{m0\,deep}}$ [m]	0.003	5.92	Significant wave height from spectral analysis = 4 m 0, determined at deep water
5	$T_{\mathrm{p\,deep}}$ [s]	0.545	15	Peak period from spectral analysis at deep water
6	$T_{\mathrm{m\,deep}}$ [s]	0.454	12.5	Mean period either from spectral analysis =m2/m0 or from time domain analysis (zero-down crossing) at deep water
7	$T_{\mathrm{m-1,0\,deep}}$[s]	0.495	13.636	Mean period from spectral analysis at deep water = m 1/m0 -
8	β [°]	0	80	Angle of wave attack relative to the normal on the structure
9	$H_{\mathrm{m0\,toe}}$ [m]	0.003	3.8	Significant wave height from spectral analysis = 4 m 0 at the toe of the structure.
10	$T_{\mathrm{p\,toe}}$ [s]	0.545	16.4	Peak period from spectral analysis at the toe of the structure
11	$T_{\mathrm{m\,toe}}$ [s]	0.454	11.881	Mean period either from spectral analysis =m2/m0 or from time domain analysis (zero-down crossing) at the toe of the structure.
12	$T_{\mathrm{m-1,0\,toe}}$ [s]	0.495	10.64	Mean period from spectral analysis at the toe of the structure = m_{-1}/m_0.
13	q $[m^3/s.m]$	0	0.165	Overtopping discharge per second per meter width
14	Pow [-]	0	81	Percentage of the waves resulting in overtopping
				Structural parameters
15	h_{deep} [m]	0	100	Water depth at deep water
16	m [-]	6	1000	Slope of the foreshore
17	h [m]	0.029	9.32	Water depth at the toe of the structure
18	h_{t} [m]	0.025	7.78	Water depth on the toe of the structure
19	B_{t} [m]	0	10	Width of the toe of the structure
20	γ_{f} [-]	0.35	1	Roughness/permeability factor for the structure
21	$cot_{\alpha d}$ [-]	0	7	Cotangent of the slope of the structure downward of the berm
22	$cot_{\alpha u}$ [-]	-5	9.706	Cotangent of the slope of the structure upward of the berm
23	$cot_{\alpha \mathrm{excl}}$ [-]	-1.533	8.144	Mean cotangent of the slope of the structure, without contribution of the berm
24	$cot_{\alpha \mathrm{incl}}$ [-]	-1.533	12.821	Mean cotangent of the slope of the structure, with contribution of the berm
25	R_{c} [m]	0	8.345	Crest freeboard of the structure
26	B [m]	0	8	Width of the berm
27	h_{b} [m]	-0.208	1.175	Water depth on the berm
28	tanαB [-]	0	0.125	Tangent of the slope of the berm
29	B_{h} [m]	0	8	Width of the horizontally schematized berm
30	A_{c} [m]	0	7.87	Armour crest freeboard of the structure
31	G_{c} [m]	0	5.6	Width of the structure crest

VI.5. Data preprocessing

Table 1 presents the Data Type and Missing Values for each column in the database. It is important to note that there are missing values requiring a cleaning phase.

Table VI-5 Parameter characteristics of CLASH database.

Column Number	Column Name	Data Type	Missing Values
1	Name	object	0
2	$H_{mo\ deep}$ (m)	float64	435
3	$T_{p\ deep}$ (s)	float64	379
4	$T_{m\ deep}$ (s)	float64	379
5	$T_{m-1,0\ deep}$ (s)	float64	379
6	$h_{\ \mathrm{deep}}$ (m)	float64	1
7	m (-)	float64	54
8	$\beta(°)$	float64	24
9	h (m)	float64	2
10	$H_{m0\ toe}$ (m)	float64	35
11	$T_{p\ toe}$ (s)	float64	59
12	$T_{m\ toe}$ (s)	float64	59
13	$T_{m-1,0\ toe}$ (s)	float64	25
14	h_t (m)	float64	1
15	B_{t} (m)	float64	0
16	γ_f (-)	float64	16
17	$cot_{\alpha d}$ (-)	float64	0
18	$cot_{\alpha \mathrm{u}}$ (-)	float64	0
19	$cot_{\alpha \mathrm{excl}}$ (-)	float64	26
20	$cot_{\alpha \mathrm{incl}}$ (-)	float64	26
21	R_c (m)	float64	1
22	B (m)	float64	0
23	h_b (m)	float64	0
24	$tan_{\alpha B}$ (-)	float64	0
25	B_h (m)	float64	0
26	Ac (m)	float64	0
27	Gc (m)	float64	0
28	RF (-)	int64	0
29	CF (-)	int64	0
30	q $(m^3/s/m)$	object	7
31	P_{ow}	float64	9792
32	Remark	object	10023
33	Reference	object	2816

VI.5.1. Database cleaning

Given that erroneous data can significantly compromise the performance of the models to be built, the initial database was reduced by eliminating data classified as "unreliable" tests (RF=4) or data where the cross-section was considered "very complex" (CF=4). Clear inconsistencies within the database were detected and removed. All rows with missing values were deleted, resulting in a reduced database containing 8091 tests.

	Name	Beta	h	Hm0 toe	Tm-1,0 toe	ht	Bt	gf	cotad	cotau	Rc	B	hb	tanaB	Bh	Ac	Gc	q
0	380-026	0	1.014	0.114	1.437	0.400	0.143	0.38	2.0	2.0	0.300	0.00	0.00	0.0	0.00	0.186	0.514	4.830000e-09
1	030-339	0	0.160	0.050	0.846	0.160	0.000	1.00	4.0	4.0	0.120	0.40	0.00	0.0	0.40	0.120	0.000	2.020000e-09
2	380-007	0	1.014	0.112	1.437	0.366	0.143	0.38	2.0	2.0	0.220	0.00	0.00	0.0	0.00	0.129	0.523	1.060000e-08
3	352-055	0	0.280	0.118	1.650	0.193	0.070	0.38	1.5	2.0	0.228	0.63	0.07	0.0	0.63	0.228	0.162	1.160000e-08
4	380-033	0	1.014	0.114	1.437	0.400	0.143	0.38	2.0	2.0	0.220	0.00	0.00	0.0	0.00	0.186	0.514	1.450000e-08
...	...	...	...	...	...	...	...	...	...	...	...	...	...	...	...	...	...	...
8086	102-022	0	0.800	0.127	1.775	0.800	0.000	1.00	4.0	4.0	0.000	0.00	0.00	0.0	0.00	0.000	0.000	1.040000e-02
8087	102-023	0	0.800	0.128	2.166	0.800	0.000	1.00	4.0	4.0	0.000	0.00	0.00	0.0	0.00	0.000	0.000	1.320000e-02
8088	102-019	0	0.800	0.086	2.203	0.800	0.000	1.00	4.0	4.0	0.000	0.00	0.00	0.0	0.00	0.000	0.000	8.000000e-03
8089	102-018	0	0.800	0.083	1.775	0.800	0.000	1.00	4.0	4.0	0.000	0.00	0.00	0.0	0.00	0.000	0.000	7.650000e-03
8090	102-020	0	0.800	0.077	3.033	0.800	0.000	1.00	4.0	4.0	0.000	0.00	0.00	0.0	0.00	0.000	0.000	9.020000e-03

Figure VI-7 Overview of the cleaned Database

VI.5.2. Application of Froude Similarity

Froude similarity is a method used to resize hydraulic parameters in order to achieve similar behaviors between reduced-scale prototypes and real-world conditions. It is based on the ratio of inertial and gravitational forces to maintain the same proportions and characteristics. The Froude similarity law was employed to provide the best generalization of large-scale applications. The equations (Equation VI-1, Equation VI-2, Equation VI-3 and Equation VI-4) give the necessary laws for Froude similarity scaling.

$$n_L = 1/\mathrm{H}_{\mathrm{mo,toe\ observed}} \qquad \textbf{Equation VI-1}$$

$$[n_{\mathrm{Hm0}}, n_{\mathrm{h}}, n_{\mathrm{ht}}, n_{\mathrm{Bt}}, n_{\mathrm{B}}, n_{\mathrm{hb}}, n_{\mathrm{Rc}}, n_{\mathrm{Ac}}, n_{\mathrm{Gc}}] = n_L \qquad \textbf{Equation VI-2}$$

$$n_{\mathrm{T}} = {n_L}^{0.5} \qquad \textbf{Equation VI-3}$$

$$n_q = {n_L}^{1.5} \qquad \textbf{Equation VI-4}$$

After performing the equations (Equation VI-1, Equation VI-2, Equation VI-3 and Equation VI-4) on the database, the statistical outcomes were consolidated in Table VI-6. It can be observed that the obtained results are almost identical to those published Table VI-7 by (Gosse, J. S., Jentsje Wouter, v. d., et al. (2004).

Table VI-6 Summary of statistics obtained after applying the Froude scale.

	Mean	Standard Deviation	Maximum	Minimum
$H_{mo}{}'$	1.00	1.00	1.00	1.00
$T_{m-1,0}{}'$	5.04	2.79	69.46	2.72
β ’	3.3	11.4	79.00	0.0
h’	3.72	2.75	32.22	0.90
$h_t{}'$	3.28	2.58	25.93	0.49
$B_t{}'$	0.78	1.55	19.05	0.00
$\gamma_f{}'$	0.70	0.28	1.00	0.33
$cot_{\alpha d}{}'$	2.00	1.43	7.00	0.00
$cot_{\alpha u}{}'$	1.90	1.70	9.71	-5.00
Rc’	1.42	0.64	6.42	0.00
B’	0.70	2.13	38.46	0.00
h_b’	0.05	0.41	7.89	-1.21
$tan_{\alpha B}$’	0.00	0.01	0.10	0.00
Ac’	1.32	0.65	6.24	0.00
Gc’	0.95	1.32	13.24	0.00
q’	$8.03.10^{-3}$	$2.03.10^{-2}$	$4.22.10^{-1}$	$1.25.10^{-7}$

Table VI-7 Summary of statistics obtained by the article after applying the Froude scale.

Parameter	*Mean*	*Standard Deviation*	*Maximum*	*Minimum*
H_{m0}’ (m)	1.0	0.0	1.0	1.0
$T_{m-1,0}$’ (s)	5.0	2.8	69.5	2.7
β’	3.4	11.3	80.0	0.0
h’ (m)	3.7	2.8	32.2	0.9
h_t’ (m)	3.3	2.7	25.9	0.5
B_t’ (m)	0.7	1.5	19.0	0.0
γ_f’	0.7	0.2	1.0	0.3
$cot\ \alpha_d$’	1.9	1.4	7.0	0.0
$cot\ \alpha_u$’	1.8	1.7	9.7	-5.0
B’ (m)	0.7	2.1	38.5	0.0
h_b’ (m)	0.1	0.4	7.9	-1.2
$tan\ \alpha_b$’	0.0	0.01	0.13	0.0
R_c’ (m)	1.4	0.6	6.4	0.0
A_c’ (m)	1.3	0.6	6.2	0.0
G_c’ (m)	0.9	1.3	13.2	0.0
q’ (m^3/s/m)	$8{\cdot}10^{-3}$	$2{\cdot}10^{-2}$	$4{\cdot}10^{-1}$	$1{\cdot}10^{-7}$

VI.6. Analysis and Validation of the ANN Algorithm

In this section, the neural network (NN) model developed by Gent, M. R., Boogaard, H. F., et al. (2007) is replicated. The features used by this algorithm are displayed in the Table VI-8 .

Table VI-8 Features used for the development of the NN model.

Name	Symbol	Unit	NN	*Fr* Scaled
Mean wave overtopping discharge	q	$m^3/s/m$	✓	✓
Water depth, toe	h	m	✓	✓
Spectral significant wave height, toe	$H_{m0,toe}$	m	✓	-
Spectral wave period, toe	$T_{m-1,0,toe}$	s	✓	✓
Angle of wave attack	β	°	✓	-
Roughness factor of the structure	γ_f	-	✓	-
Cotangent of the lower slope	$\cot \alpha_d$	-	✓	-
Cotangent of the upper slope	$\cot \alpha_u$	-	✓	-
Crest freeboard	R_c	m	✓	✓
Armour crest freeboard	A_c	m	✓	✓
Difference between crest and armour crest freeboard	dA_c	m	-	✓
Crest width	G_c	m	✓	✓
Width of the berm	B	m	✓	✓
Water depth above the berm	h_b	m	✓	✓
Tangent of berm slope	$\tan \alpha_B$	-	✓	-
Water depth above the toe structure	h_t	m	✓	✓
Thickness of the toe structure	t_t	m	-	✓
Width of the toe structure	B_t	m	✓	✓
Complexity factor	CF	-	✓	-
Reliability factor	RF	-	✓	-

After reproducing this model as described in Gent, M. R., Boogaard, H. F., et al. (2007), the obtained results are illustrated in Figure VI-8. The R^2 score indicates a value of 0.84 for the training ensemble and 0.82 for the test ensemble. These scores demonstrate a good correlation between the measured and predicted values, as supported by the scatter plot.

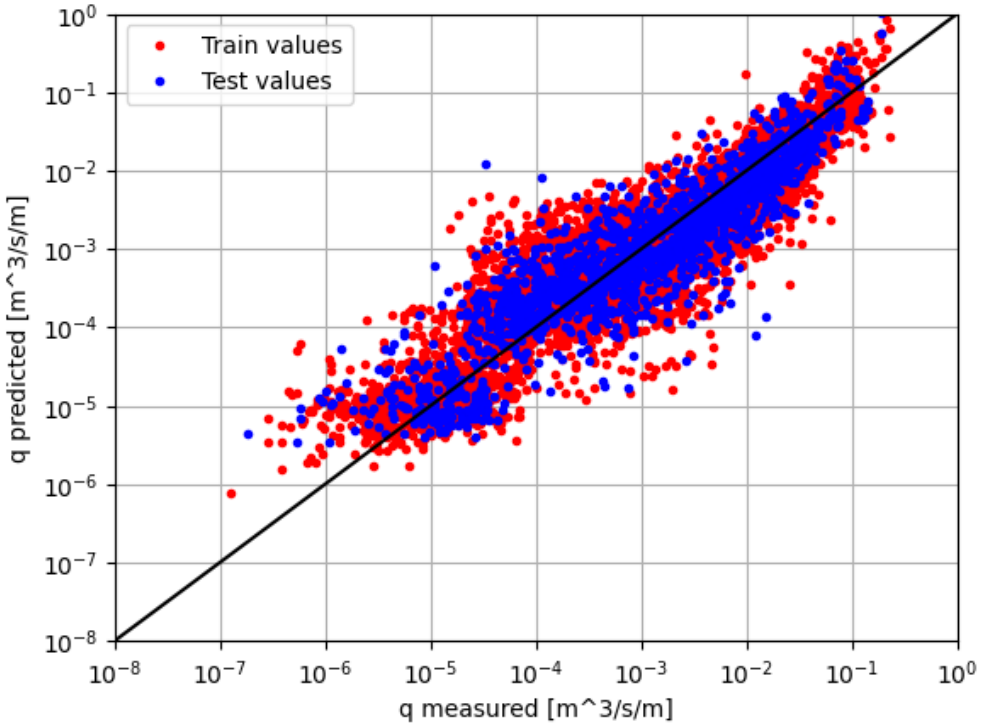

Figure VI-8 Predictions of the replicated ANN method.

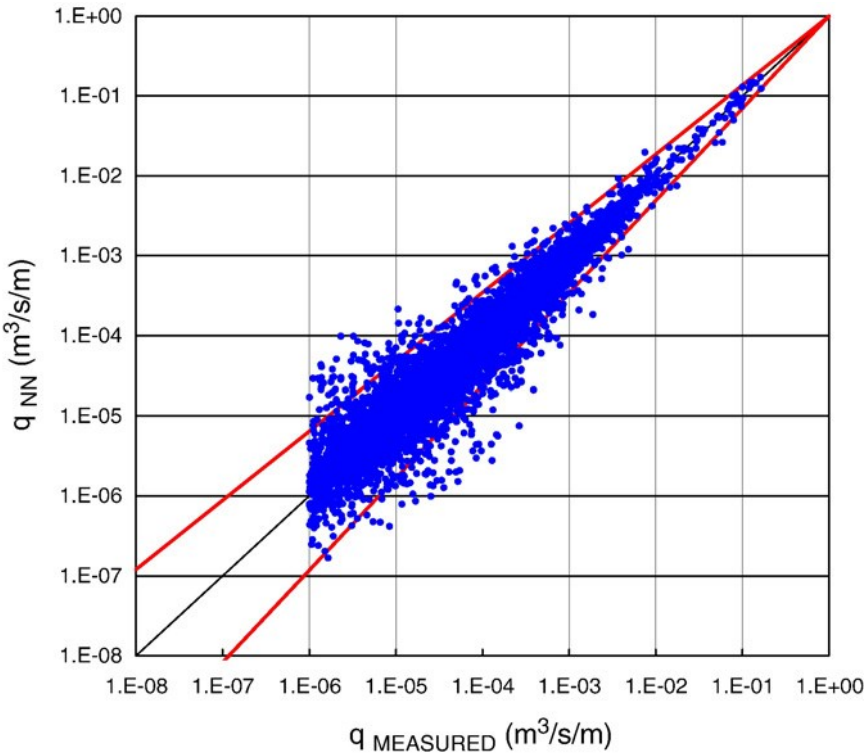

Figure VI-9 Predictions of the published ANN method (2007).

VI.7. Analysis and Validation of the XGBoost Algorithm

The XGBoost algorithm, originally published in 2020 by Bieman, J. P., et al., is replicated in this section. The features utilized by this algorithm are displayed in the Table VI-9.

Table VI-9 Features used for the development of the XGBoost model.

Name	Symbol	Unit	XGB	*Fr* Scaled
Mean wave overtopping discharge	q	$m^3/s/m$	✓	✓
Water depth, toe	h	m	✓	✓
Spectral significant wave height, toe	$H_{m0,toe}$	m	✓	-
Spectral wave period, toe	$T_{m-1,0,toe}$	s	✓	✓
Angle of wave attack	β	°	✓	-
Roughness factor of the structure	γ_f	-	✓	-
Cotangent of the lower slope	$\cot\alpha_d$	-	✓	-
Cotangent of the upper slope	$\cot\alpha_u$	-	✓	-
Crest freeboard	R_c	m	✓	✓
Armour crest freeboard	A_c	m	-	✓
Difference between crest and armour crest freeboard	dA_c	m	✓	✓
Crest width	G_c	m	✓	✓
Width of the berm	B	m	✓	✓
Water depth above the berm	h_b	m	✓	✓
Tangent of berm slope	$\tan\alpha_B$	-	✓	-
Water depth above the toe structure	h_t	m	-	✓
Thickness of the toe structure	t_t	m	✓	✓
Width of the toe structure	B_t	m	✓	✓
Complexity factor	CF	-	✓	-
Reliability factor	RF	-	✓	-

The python implementation of the algorithm, as outlined in the article, is utilized to replicate the results. The Figure VI-10 presents a visual representation of the obtained outcomes. The training ensemble yields an R^2 score of 0.95, while the test ensemble achieves a score of 0.89. These scores establish a strong association between the predicted and observed values, which is further supported by the scatter plot.

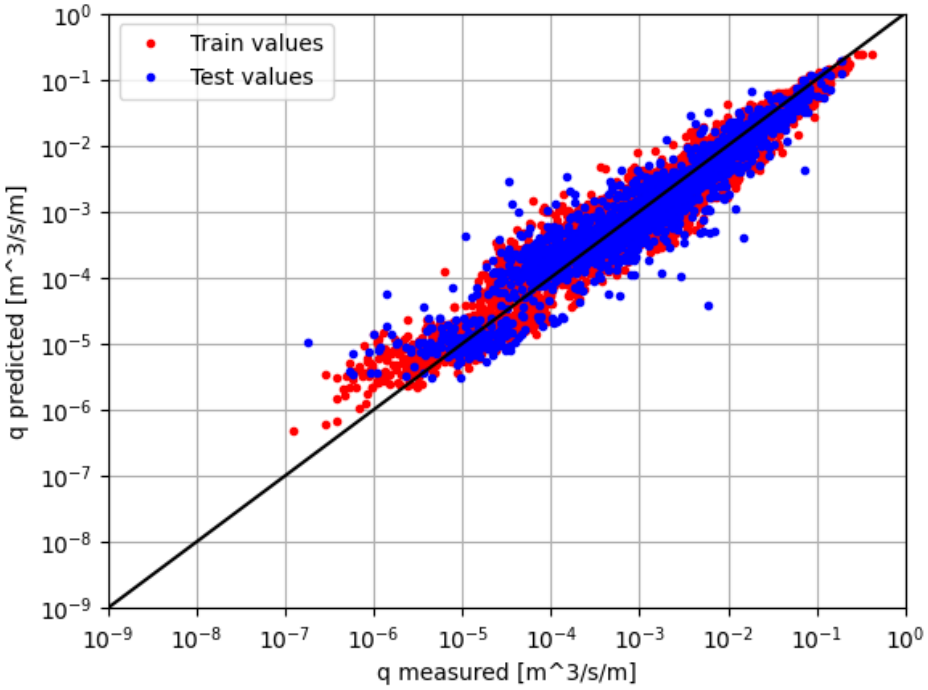

Figure VI-10 Predictions of the replicated XGBoost method.

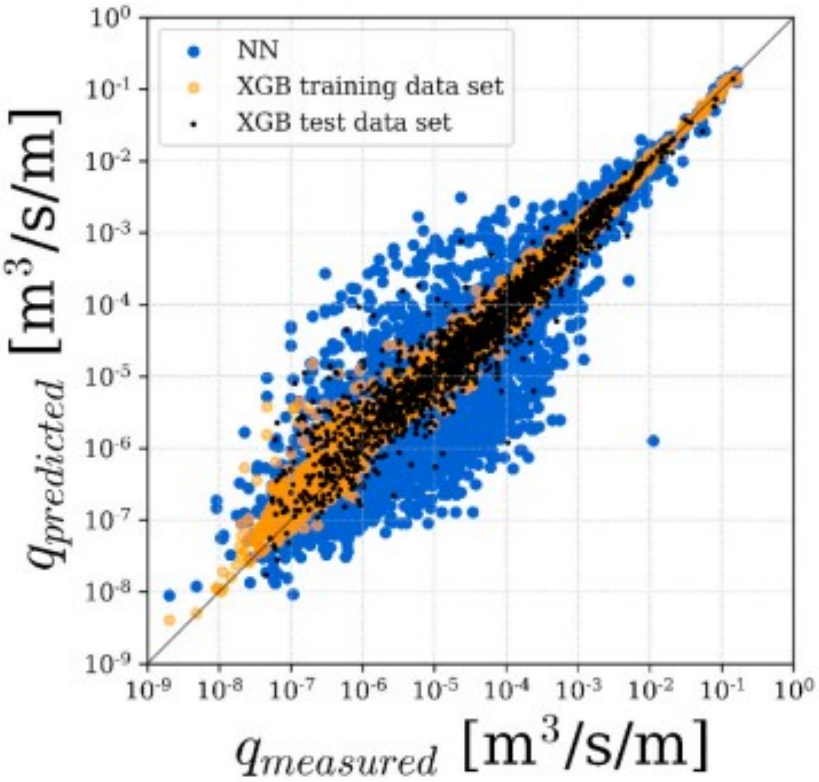

Figure VI-11 Predictions of the published XGBoost method (2020).

VI.8. Model developed for rubble mound breakwater

The cleaned database, containing 8091 entries with different types of structures, was reduced by selecting only the structures most similar to the rubble mound breakwater implemented at Marina and Port of Algiers. Furthermore, the data was filtered based on their reliability factor, with tests having reliability levels 1, 2, and 3 being chosen.

In order to improve the prediction performance of wave overtopping and achieve a good score, the least influential features are eliminated. The hydraulic parameters of deep waters were not considered to avoid redundancy, as they are strongly related to the parameters at the base of the structure. However, tests corresponding to overtopping with $q = 0\ m^3/\mathrm{s/m}$ were included. The resulting database now have 848 entries, and the number of parameters has been reduced from 31 to 13 parameters. The Figure VI-12 provides an overview of the database used during the model development.

	m	h	Hm0 toe	Tp toe	Tm toe	Tm-1,0 toe	ht	Bt	gf	cotaincl	Rc	Ac	Gc
0	50	0.405	0.129	1.388	1.157	1.262	0.405	0.0	0.38	2.00	0.259	0.101	0.149
1	50	0.405	0.129	1.388	1.157	1.262	0.405	0.0	0.38	1.33	0.259	0.101	0.149
2	50	0.405	0.129	1.388	1.157	1.262	0.405	0.0	0.40	2.00	0.223	0.142	0.250
3	50	0.405	0.129	1.388	1.157	1.262	0.405	0.0	0.40	1.33	0.240	0.101	0.250
4	50	0.405	0.129	1.388	1.157	1.262	0.405	0.0	0.40	1.33	0.259	0.101	0.250

Figure VI-12 Overview of the Rubble mound breakwater database.

Firstly, this database was divided into two parts, with 80% of the data used for training and 20% for testing. Then, the features were subjected to a polynomial transformation of degree 4 (Amara, L, Chalal, Y. (2022)), which generated a new feature vector.

Various methods, such as polynomial regression, support vector regression, neural network (ML Regressor), and XGBoost, were tested on the database. Unfortunately, the obtained results were not satisfactory.

Afterwards, the XGBoost model using scikit-learn was applied with the following parameters.

- max_depth: 6. This parameter controls the maximum depth of a tree. A higher value can result in a more complex model, which may lead to overfitting.
- min_child_weight: 5. This parameter specifies the minimum sum of instance weight (hessian) needed in a child. It is used to control over-fitting. A higher value makes the algorithm more conservative.
- learning_rate: 0.05. This parameter controls the step size shrinkage during each boosting iteration. A lower value makes the model more robust but requires more iterations to converge.

We have obtained very satisfactory results; ($R2\ score\ for\ the\ training\ set\ =\ 0.97$) and ($R2\ score\ for\ the\ test\ set\ =\ 0.92$). It is clear from the figure that the model's performance is very high when flow rates are significant (> 0.01 liter). The correlation diagram is shown in the (Figure VI-13), where we observe a strong correlation between the measured and predicted results within the mentioned interval.

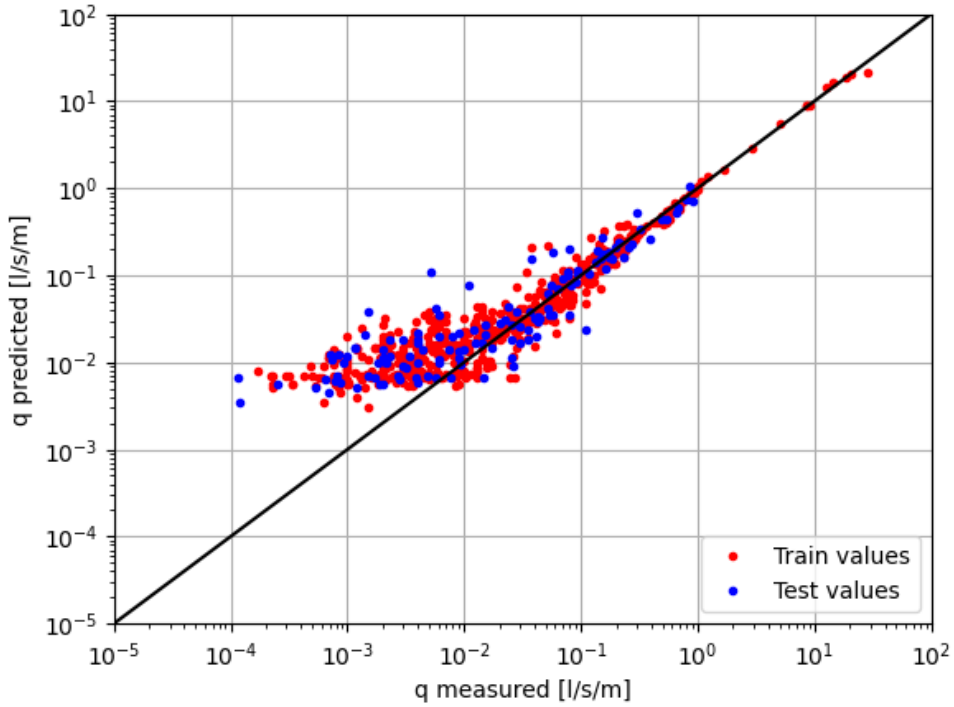

Figure VI-13 Predictions of the developed model for rubble mound breakwater Database.

VI.9. Conclusion

In conclusion, the CLASH (Crest Level Assessment of Coastal Structures by Full-Scale Monitoring, Neural Network Prediction, and Hazard Analysis on Permissible Wave Overtopping) database serves as a valuable resource for studying wave overtopping of coastal structures. This database was utilized to develop models aimed at predicting the overtopping rate. Specifically, two models were published on this topic: a Neural Network model in 2007 and an XGBoost algorithm model in 2020. In this chapter, these two models were replicated and analyzed. Additionally, a new model was developed specifically for rubble mound breakwaters, which utilizes polynomial features in conjunction with the XGBoost algorithm. All the models demonstrated good correlations between measured and predicted values, indicating their effectiveness in wave overtopping prediction.

Chapter VII. Wave flume

VII.1. Introduction

The wave flume is an important tool in coastal engineering research, allowing for the creation of scaled-down models that simulate the characteristics of natural waves. In this chapter, we study the first order wave generation theory, which serves as the foundation for understanding wave generation in wave flumes. By exploring the principles behind wavemaker design and operation, we can gain valuable insights into the behavior of waves and their impact on coastal areas.

VII.2. 2D Waves generator

we focus on the 2D problem of wave propagation in a wave flume. the latter is a controlled laboratory setting where researchers investigate wave characteristics and their interactions with different structures. By studying the 2D problem, we aim to understand the fundamental principles that govern wave behavior in a simplified yet representative environment. For further information, refer to the book "Physical Models and Laboratory Techniques in Coastal Engineering" (Steve,1993).

VII.2.1. Description of the Flap-Type Wavemaker

The flap-type wavemaker is a commonly employed configuration in wave flumes for precise wave generation. It consists of a wave board (flap) positioned at one end of the flume, which rotates around a pivot point. The flap's motion is controlled by an actuator system, typically comprised of hydraulic or electric motors and linkages. This scheme allows for the generation of waves with specific amplitudes, frequencies, and shapes by manipulating the motion of the flap. The flap shape minimizes disturbances in the water, ensuring efficient wave generation. Through careful calibration and adjustment of parameters, such as flap motion amplitude and speed, the flap-type wavemaker can simulate a wide range of wave conditions, making it a versatile tool for coastal engineering research. In the following, we will refer to the sketch shown in Figure VII-1.

The flap-type wavemaker assumes a sinusoidal motion for the wave board, given by Equation VII-1.

$$X_0 = X(0,t) = \frac{S_0}{2}\sin(\omega t) \qquad \textbf{Equation VII-1}$$

This motion describes the displacement of the wave board at a position $z = 0$ and time t, where S represents the amplitude of the motion and ω represents the angular frequency.

By implementing this sinusoidal motion, the wavemaker can generate waves with controlled amplitudes and frequencies, enabling precise simulation of various wave conditions in a wave flume.

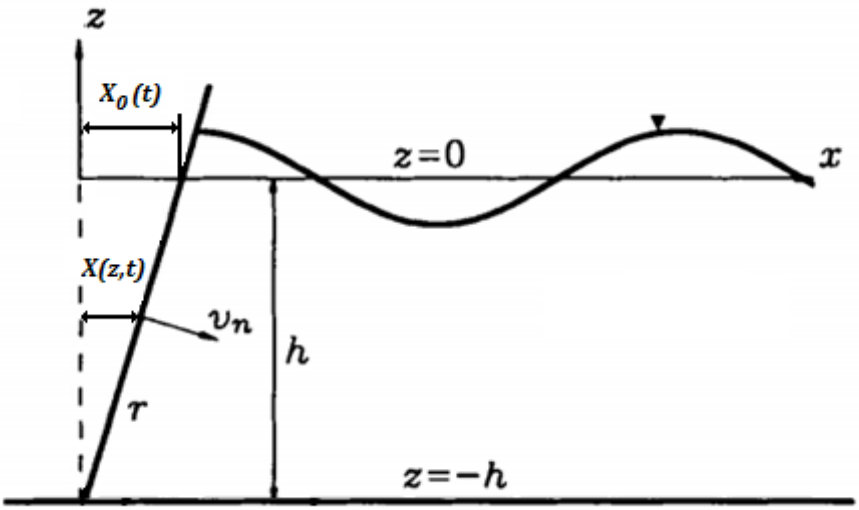

Figure VII-1 Two-Dimensional Wave Flume Definition Sketch.

VII.2.2. Mathematical model

The problem can be formulated mathematically as a set of five equations considering an inviscid and irrotational fluid flow (Steve,1993). These equations are the Laplace equation (Equation VII-2), along with four auxiliary boundary conditions. These conditions include the bottom boundary condition (Equation VII-3) , the kinematic and dynamic free surface conditions (Equation VII-4,Equation VII-5), and the boundary condition at the wavemaker board (Equation VII-6).

The primary equation used in the mathematical model is the Laplace equation, which governs the velocity potential (ϕ) in the fluid domain.

$$\frac{\partial^2 \varphi}{\partial x^2} + \frac{\partial^2 \varphi}{\partial z^2} = 0 \qquad \textbf{Equation VII-2}$$

$$\frac{\partial \varphi}{\partial z} = 0, \quad at \;\; z = -h \qquad \textbf{Equation VII-3}$$

$$\frac{\partial \eta}{\partial t} + \frac{\partial \varphi}{\partial x}\frac{\partial \eta}{\partial x} - \frac{\partial \varphi}{\partial z} = 0, \quad at\ z = \eta$$ **Equation VII-4**

$$\frac{\partial \varphi}{\partial t} + \frac{1}{2}\left[\left(\frac{\partial \varphi}{\partial x}\right)^2 + \left(\frac{\partial \varphi}{\partial z}\right)^2\right] + g\eta = 0, \quad at\ z = \eta$$ **Equation VII-5**

$$\frac{\partial \varphi}{\partial x} = \left(1 + \frac{z}{h}\right)\frac{\partial x_0(t)}{\partial t}, \quad at\ x = X(z,t)$$ **Equation VII-6**

The last condition requires that the angle θ be very small, $\theta \leq 10^{\circ}$, and that the wavemaker be flat, solid, and impermeable.

To solve the problem mentioned above, the perturbation method is employed. This method is a mathematical technique used to approximate solutions to problems by expanding the unknown functions in a series of terms based on a small parameter ε. In this case, we are interested in the generation of first-order waves, so the unknown functions are expressed as

$$\varphi = \sum_{n=1}^{\infty} \varepsilon^n \varphi_n = \varepsilon\varphi_1 + O(\varepsilon^2)$$ **Equation VII-7**

$$\eta = \sum_{n=1}^{\infty} \varepsilon^n \eta_n = \varepsilon\eta_1 + O(\varepsilon^2)$$ **Equation VII-8**

$$\theta = \sum_{n=1}^{\infty} \varepsilon^n \theta_n = \varepsilon\theta_1 + O(\varepsilon^2)$$ **Equation VII-9**

$$X_0 = \sum_{n=1}^{\infty} \varepsilon^n X_n = \varepsilon X_1 + O(\varepsilon^2)$$ **Equation VII-10**

In summary, the wavemaker problem with the first-order approximation can be described by the following equations

Laplace equation

$$\frac{\partial^2 \varphi_1}{\partial x^2} + \frac{\partial^2 \varphi_1}{\partial z^2} = 0$$ **Equation VII-11**

Bottom boundary condition for horizontal bottom

$$\frac{\partial \varphi_1}{\partial z} = 0, \quad at \;\; z = -h$$ **Equation VII-12**

Kinematic and dynamic free surface boundary condition

$$\frac{\partial^2 \varphi_1}{\partial t^2} + g\frac{\partial \varphi_1}{\partial z} = 0, \quad at\; z = 0$$ **Equation VII-13**

General wave board boundary condition

$$\frac{\partial \varphi_1}{\partial x} = \left(1 + \frac{z}{h}\right)\frac{dX_1}{dt} \quad at \quad x = 0$$ **Equation VII-14**

Using the method of separation of variables, we can obtain the final solution for the surface elevation $\eta(x,t)$ in terms of the wave parameters. The solution is given by

$$\eta_1(x,t) = \frac{\sigma A}{g}\cosh(k_1 h)\cos(k_1 x - \sigma t) + \sin(\sigma t)\sum_{n=1}^{\infty}\frac{\sigma C_n}{g}e^{-k_{3_n}x}\cos(k_{3_n}h)$$ **Equation VII-15**

where σ is defined as

$$\sigma^2 = gk_1\tanh(k_1 h) = -gk_3\tanh(k_3 h)$$ **Equation VII-16**

and A is given by:

$$A = \frac{2\sigma S_0}{k(sinh\ 2kh + 2kh)}\left[\sinh kh\,\frac{(1-\cosh kh)}{kh}\right]$$ **Equation VII-17**

The second term in Equation VII 15 becomes negligible after the distance x = 3h. This simplifies the equation to:

$$\eta_1(x,t) = \frac{\sigma A}{g}\cosh(k_1 h)\cos(k_1 x - \sigma t)$$ **Equation VII-18**

Therefore, the final expression for $\eta_1(x,t)$ is:

$$\eta_1(x,t) = \frac{H}{2}\cos(k_1 x - \sigma t)$$ **Equation VII-19**

Where the amplitude H is given by:

$$H = \frac{\sigma A}{g}\cos(k_1 h) \qquad \textbf{Equation VII-20}$$

from the Equation VII-1 we find that $\sigma = \omega$.

By substituting the expression for A into the expression for H and using the dispersion relationship to determine σ^2, we can derive the solution for a general first-order wavemaker.

$$\frac{H}{S_0} = \frac{4\sinh kh}{sinh\ 2kh+2kh}\left[\sinh kh\,\frac{(1-\cosh kh)}{kh}\right] \qquad \textbf{Equation VII-21}$$

VII.3. Wave flume synthesis

The sketch illustrated in the Figure VII-2 will be referred to during the synthesis. It should be noted that the water is present only on one side.

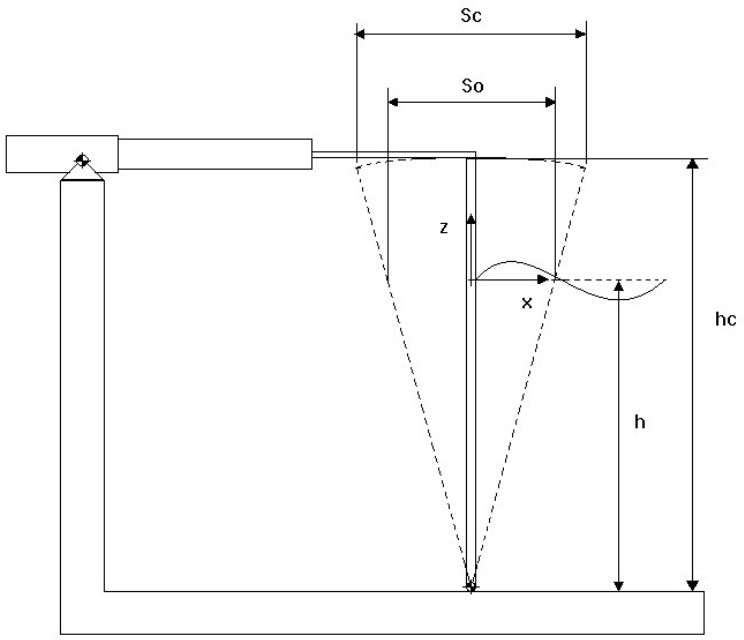

Figure VII-2 Wave flume sketch (Mario, 2019).

The dimensions of the target wave flume and the quantities mentioned in the Figure VII-2are detailed in the Table VII-1.

Table VII-1 System dimensions summary.

$30\ m\ x\ 2.2\ m\ x\ 0.88\ m$	Wave flume dimensions
$T\ =\ 0.5\ s\ -\ 2.5\ s$	Wave period range of interest
$h\ =\ 0.7\ m$	Water depth
$h_{\ c}\ =\ 1.1\ m$	Height of the link between flap and electro cylinder

First, we need to assess the wave generation capability of the flume. According to the linear water wave theory. We can then determine the maximum expected wave height for each wave period within the specified range. However, this assessment is subject to certain constraints that affect the system. Therefore, the following limits need to be considered.

VII.3.1. Wave Break Limit

If the wave height exceeds the limit $\left(\frac{H}{L} < \frac{1}{7}\right)$, the wave will not maintain a regular shape and is likely to break. To avoid this phenomenon and maintain the regular aspect of the wave, Equation VII-22 is used to calculate the value of $S_{0,wb}max$, which is a constant related to the regularity of the wave.

$$S_{0,wb}max = \frac{\pi h}{14 \sinh kh} \frac{\sinh 2kh + 2kh}{kh \,.\sinh kh - \cosh kh + 1} \qquad \textbf{Equation VII-22}$$

VII.3.2. Maximum wave height in the flume

Referring to the sketches Figure VII-2, the maximum attainable wave height is set at $H_{max} = 0.4$ meters. This means that the waves generated within the system won't go through this height. This yields to Equation VII-23.

$$S_{0,wh}max = 0.4 \cdot \frac{\sinh 2kh + 2kh}{4 \cdot \sinh kh \left[\sinh kh + \frac{1 - \cosh kh}{kh}\right]} \qquad \textbf{Equation VII-23}$$

VII.3.3. Ballscrew maximum acceleration

The acceleration a of the Ballscrew must be taken into consideration, as it directly depends on the stroke S_c. In the following we assume $a_{max} = g$ which gives us the Equation VII-24.

$$a(t) = -\frac{S_c}{2}\omega^2 \sin \omega t \implies S_{c,B}max = \frac{g}{2\pi^2}T^2 \qquad \textbf{Equation VII-24}$$

VII.3.4. Maximum actuator stroke

From the boundary condition at the wavemaker board (Equation VII-6), the maximum recommended angle excursion is set to 10°. Taking advantage of this information, a new limit of Sc is obtained (Equation VII-25).

$$S_c max = 2h_c \tan\theta = 0.46\, m \rightarrow S_c max = 0.5\, m \qquad \textbf{Equation VII-25}$$

VII.3.5. Wave number determination

Before plot the limits, we need to solve the dispersion relation (Equation VII-26) in order to determine the wave number k corresponding to each period of range.

$$\sigma^2 = gk\tanh(kh)$$ **Equation VII-26**

For a fixed period and a constant water depth, there is only one k that satisfies Equation VII-26; This value is determined by employing an iterative process (Table VII-2) to solve the equation.

Table VII-2 Iterative process for solving the dispersion equation.

For each period of range do.

1. Calculate the angular frequency σ for the period.
2. Choose an initial value for k.
3. Calculate the angular frequency $\bar{\sigma}$ corresponding to the value of k.
4. Evaluate the difference $\sigma^2 - \bar{\sigma}^2$.
5. If the difference is greater than the desired tolerance, increment k by ***STEP*** and go to step3.
6. Else, save the value of k as the wave number of the considered period and go to the next period (go to step1).

The ***STEP*** is evaluated by $STEP = difference \times \frac{dk}{d(\sigma^2)}\Big|_{k=current\ value\ of\ k}$. It's clear from the Figure VII-3 that $for\ all\ values\ of\ k, \frac{dk}{d(\sigma^2)} = 0.1$

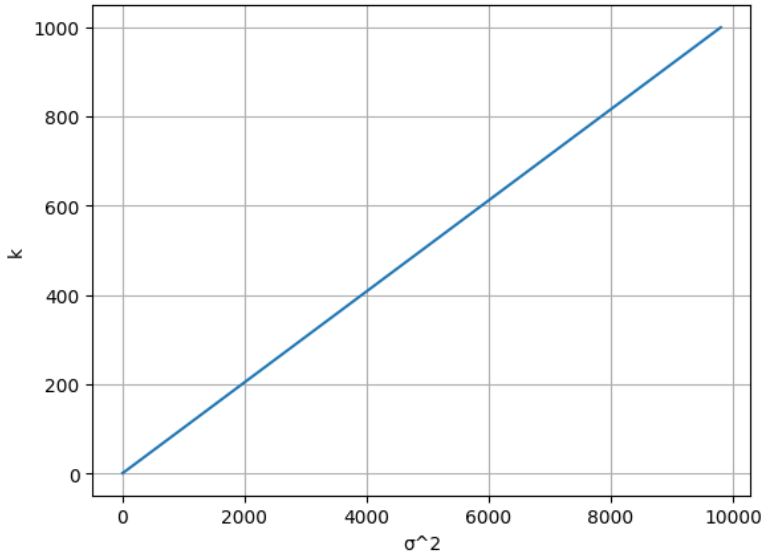

Figure VII-3 Plot of k as a function of σ^2.

To visualize the different limits of actuator stroke, the equations (Equation VII-22, Equation VII-23, Equation VII-24 and Equation VII-25) are plotted after applying the transformation $S_c = \frac{h_c}{h} \times S_0$.

From the graph illustrated in Figure VII-4, it is evident that the maximum extent of actuator strokes, represented as $S_c max$, is initially constrained by the wave break limit $S_{c,wb} max$ until $T = 1.23\ s$. Afterward, its limitation shifts to the physical capacity of the actuator.

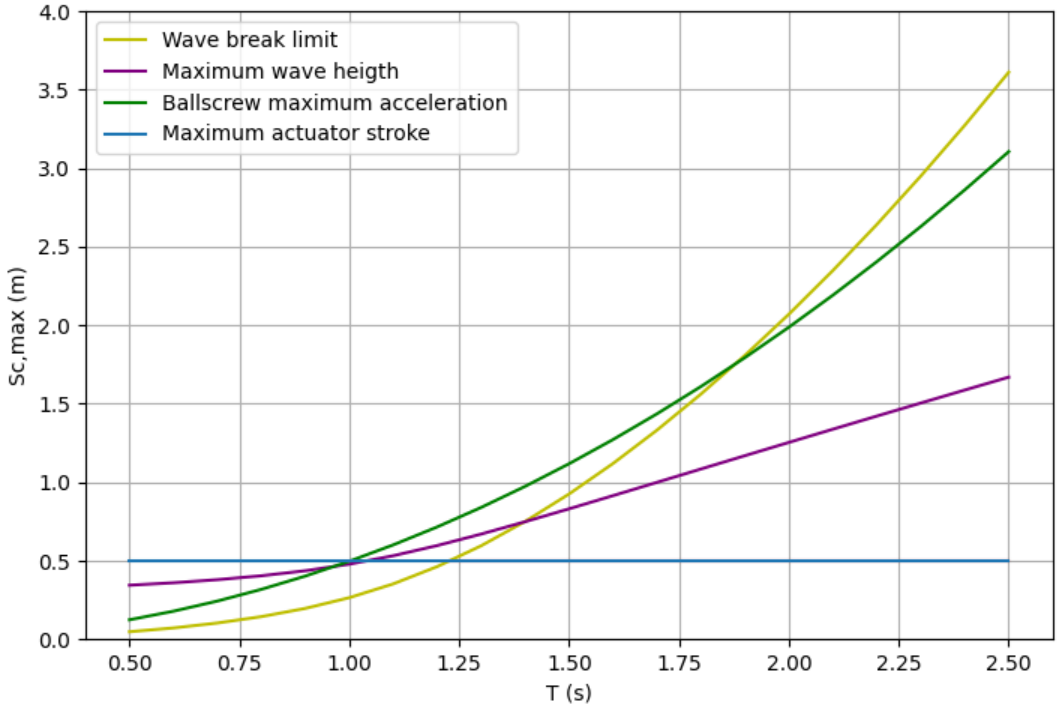

Figure VII-4 Plot of different actuator strokes limits.

By examining the limitations described in terms of actuator strokes, we can determine the maximum allowable actuator strokes (Figure VII-5) that can be utilized for each period.

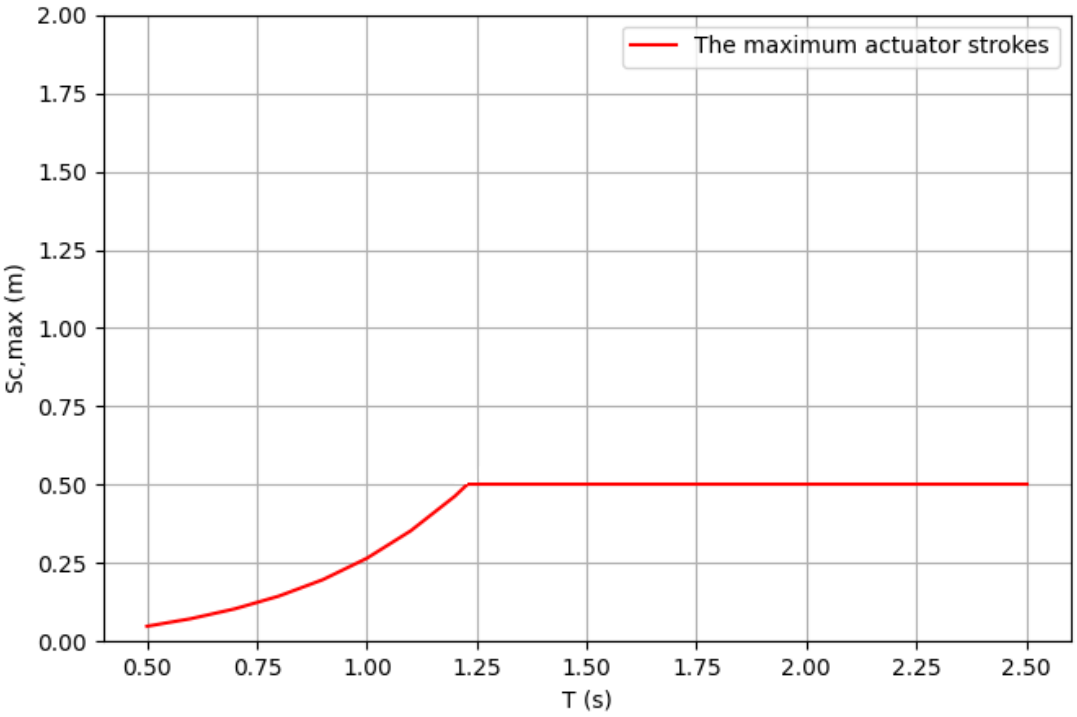

Figure VII-5 Plot of the result maximum actuator strokes limit.

Example

- For $T = 1s$, the maximum actuator stroke is about $0.25m$.
- For $T = 2s$, the maximum actuator stroke is $0.5m$.

VII.4. Conclusion

In conclusion, this chapter provides an overview of 2D wave flume analysis and synthesis. The focus is on the problem of wave propagation, specifically studying the flap-type wavemaker configuration for precise wave generation. The mathematical model is presented, which includes the Laplace equation and various boundary conditions governing the velocity potential and wave behavior. The perturbation method is employed to approximate solutions for the first-order wave generation problem. The synthesis of the wave flume is discussed, considering its dimensions and limitations such as wave break limit, maximum wave height, ballscrew acceleration, and actuator stroke. The dispersion relation is solved iteratively to determine the wave number corresponding to each period of interest. Finally, the maximum allowable actuator strokes are determined for different wave periods. Overall, this chapter provides valuable insights into the theory and practical aspects of wave flumes.

Conclusions

Coastal engineering is a multidisciplinary field focused on understanding the complex interactions between waves, coastal structures, and the shoreline. It plays a crucial role in designing ports, shore protection measures, and coastal defense structures, with waves shaping coastal environments. Predicting and comprehending overtopping, where waves exceed coastal structure crests and flow onto protected areas, is essential to mitigate risks to personnel, vessels, infrastructure, erosion, and disruptions in port operations.

In our study, the analysis conducted on the wind and wave climate in Algiers Bay has provided significant findings regarding the environmental conditions of the area. This study revealed that the significant wave height in Algiers Bay ranges from 0.03m to 7.48m over a 30-year period, with an average of 1.16m. The prevailing wave directions were from the North-East and West, with North-East winds dominating in summer and West winds more frequent in winter.

Understanding the wind and wave climate is crucial in designing effective coastal protection measures. By analyzing extreme events, the likelihood of rare marine phenomena can be understood, enabling the creation of models representing their probability distributions (Stander, C. (2015)), This knowledge plays a pivotal role in designing reliable coastal defense structures and mitigating the impact of such events.

The findings from our numerical modeling emphasize the importance of considering the morpho-bathymetry of Algiers Bay in reducing wave heights that affect coastal structures. Notably, the Marina experienced a significant reduction of over 55% in wave heights for large-amplitude waves, primarily due to the interaction between waves and the seafloor directing wave propagation northwards in the Marina area. Conversely, the Port witnessed a less pronounced reduction in wave heights, reaching approximately 20% for large-amplitude waves.

Regarding current patterns, extreme events did not have a significant impact on local current velocities, which remained consistent across various simulated climate scenarios. However, the incident wave direction played a significant role in shaping the current patterns, resulting in multiple flow directions and generated channels. Waves from the North-Northeast were particularly influential, generating circular currents on either side of the Marina and the Algiers Port. The recorded current velocities ranged from 0.3 m/s to 0.45 m/s.

Comparing design calculations using the Hudson and Van der Meer formulas for rubble mound breakwaters (Rock Manual. CETMEF, 2007) provided valuable insights for the design of the main jetty of the Marina and Khireddine jetty in Algiers Port. Notably, the weight of the blocks in Mairna main jetty was smaller due to the natural protection offered by its location. This study emphasizes the significance of considering the specific characteristics of the study area and selecting appropriate design formulas to ensure effective and resilient breakwater designs.

The CLASH (Crest Level Assessment of Coastal Structures by Full-Scale Monitoring, Neural Network Prediction, and Hazard Analysis on Permissible Wave Overtopping) was utilized to develop models aimed at predicting the overtopping rate. Two models, a Neural Network model in 2007 (Gent, M. R., Boogaard, H. F., et al. (2007)) and an XGBoost algorithm model in 2020 (Bieman, J. P., al, J. M. (2020), were replicated and analyzed. Additionally, a new model specifically for rubble mound breakwaters was developed, which utilizes polynomial features in conjunction with the XGBoost algorithm. All the models exhibited good correlations between measured and predicted values, indicating their effectiveness in wave overtopping prediction.

The last chapter provided an overview of 2D wave flume analysis and synthesis, focusing on the problem of wave propagation and studying the flap-type wavemaker configuration (Steve, H. (1993)). The mathematical model included the Laplace equation and various boundary conditions govern the wave behavior. The perturbation method was employed to approximate solutions for the first-order wave generation problem. The synthesis of the wave flume provides the maximum allowable actuator strokes for different wave periods (Mario, B. (2018-2019)). This chapter provided valuable insights into the theory and practical aspects of wave flumes.

The conclusions drawn from this work offer promising prospects for the integration of machine learning techniques in the field of coastal engineering. Additionally, wave flume simulations can be explored in order to construct a database which will be a solid foundation for the establishment of comprehensive databases on overtopping. This advancement can significantly contribute to the design and evaluation of resilient coastal defense systems. These databases can support research and assist students in their work, enabling them to access valuable data and contribute to the development of innovative solutions in coastal engineering. Furthermore, universities can focus on the realization of advanced wave flumes to facilitate real-life experiments, fostering a deeper understanding of wave behavior and its interaction with coastal structures. Such facilities would provide a valuable resource for researchers and students, encouraging further advancements in the field of coastal engineering.

References

A, J. P., Gent, M. R. (2021). Wave overtopping predictions using an advanced machine. *journal homepage*, 12. doi:103830

Alem. A., Saf. B., (2021), « Etude hydrodynamique et d'agitation portuaire – Cas du port d'Alger », mémoire d'ingénieur. Gestion et protection du Littoral. Dely-Ibrahim: ENSSMAL, p-p. 46-880.

Amara, Lounis, et Yahia Chalal. (2022), *Machine learning pour l'étude de la performance hydraulique des ouvrages portuaires, cas Marina d'Alger.Gestion et Protection du Littoral.* Dely brahim: ENSSMAL.

Andersson, K. ***A (2020).*** *comparative study of VaR and ES using extreme value theory.*

Antoine, Crochet-Damais. *Journaldunet.* 02 Fevier (2022). https://www.journaldunet.fr/web-tech/guide-de-l-intelligence-artificielle/1501311-apprentissage-supervise/.

Axelsson, T. (2018) *Using supervised learning algorithms to model the behavior of Road Weather Information System sensors.*

Bhattarai, M. (2022). *Use of supervised machine learning algorithms for predictions of values theoretically.*

Bieman, J. P., al, J. M. (2020). Prediction of Mean Wave Overtopping Discharge. *Water 2020, 12, 1703*, 13. doi:10.3390/w12061703

Bonnfille. R., (2010), « Mouvements de la mer et leurs risques ». Techniques de l'ingénieur Les aménagements des voies de transport [en ligne]. [Consulté le 20/02/2023]. T. base documentaire : TIB550DUO. No ref. Article : c4610. Publisher : Editions T.I. Type. Disponible sur le site Web :https://www.techniques-ingenieur.fr/base-documentaire/construction-et-travaux-publics-th3/les-amenagements-des-voies-de-transport-42550210/mouvements-de-la-mer-et-leurs-risques-c4610/

Center, C. E. (1984). *Shore protection manual.* Washington DC: Département of the army Waterways Experiment Station, Corps of Engineers.

Ciria, C.Cetmef. (2007). *the rock manual. the use of rock in hydraulic engineering. Publicação, (C683).*

CIRIA, CUR, CETMEF. (2009). *Guide Enrochement - L'utilisation des enrochements dans les ouvrages hydrauliques - version française du rock manuel.* Compiègne: CETMEF.

Ciria, Cur, Cetmef. (2006). *The Rock Manual. The use of rock in hydraulic engineering.*

Coles, S., Bawa, J., Trenner, L., & Dorazio, P. (2001). *An introduction to statistical modeling of extreme values (p. 208).* London: Springer.

Dan, S.; Altomare, C.; et al (2020). Reduction of Wave Overtopping and Force Impact at Harbor Quays Due to Very Oblique Waves. 8. [en ligne]. [Consulté le 20/04/2023]. Disponible sur le web :https://doi.org/10.3390/jmse8080598

DHI., (2014). MIKE 21/3 Couple Model FM.
DHI., (2014). MIKE 21 Spectral Wave Module.
DHI., (2014). MIKE ZERO: Creating 2D Bathymetries. Bathymetry Editor & Mesh Generator.

Esther, Gómez-Martín, et Ramon Josep. (2016). «Cupipod manual.» *BOOK* (Université polytechnique de Valencia).

Etemad-Shahidi, Amir, et Saeeed Shaeri. (2016). «Prediction of wave overtopping at vertical structures.» *Coastal Engineering*

Gent, M. R., Boogaard, H. F., et al. (2007). Neural network modelling of wave overtopping at coastal structures. 8. Récupéré sur https://www.sciencedirect.com/science/article/abs/pii/S0378383906001918

Gent, M. V., Pozueta, B., et al. (2004, 12). Prediction method Neural network modelling of wave overtopping at coastal structures. *54*. Récupéré sur https://doi.org/10.1016/j.coastaleng.2006.12.001

Gosse, J. S., Jentsje Wouter, v. d., et al. (2004). The international database on wave overtopping. 15. doi:10.1142/9789812701916_0347

Guler, H. G., Ergin, A., et al. (2014). A comparative study on the stability formulas of rubble mound breakwaters. Coastal Engineering, 2.

Hogeveen, K. (2021). *Climate Adaption of Rubble Mound Breakwaters :A study to the accuracy of overtopping formulas for combination of solutions.* University of Technology of Delf, 2021.

Jacob, Maria, Cláudia Neves, Danica Vukadinović Greetham. (2020). *Forecasting and Assessing Risk of Individual Electricity Peaks.* Vol. 1.

Jungkyu, Ahn, et Na Yeji. (2014). «Development of Two-Dimensional Inundation Modelling Process.» *Civil Engineering*.

Kik, R., Van den Bos, J. P., Maertens, J., Verhagen, H. J., & Van der Meer, J. W. (2012). *Notional permeability. COASTAL ENGINEERING, 2.*

Mario, Beneduce. (2019). *Design of a wavemaker for the water tank at the Politecnico di Torino.* Torino: Politecnico Di Torino.

Moretto, M. (2020) *An efficient numerical approach to model wave overtopping of rubble mound breakwaters.* Université de Delf.

Papadopoulos, D. (2012). *Scour below the toe of breakwaters: Investigation of scour formation through a geometrically open filter configuration located at the toe of a rubble mound breakwater lying upon sand.*

Sharp, B. N. (1996). *CONSOLIDATION SETTLEMENT OF QUAY WALLS, QUAY APRONS AND CRANE RAILS INVOLVING ROCKFILL. Proceedings of the Institution of Civil Engineers-Water Maritime and Energy, 118(3),p.p. 177-188.*

***Shore protection manual (Vol. 1). (1984)**. Department of the Army, Waterways Experiment Station, Corps of Engineers, Coastal Engineering Research Center.* (US), Coastal Engineering Research Center.

Stander, C. (2015). *Analysis of extreme events in the coastal engineering environment (Doctoral dissertation, Stellenbosch:.* Stellenbosch University, 2015.

Steve, Hughes. (1993). *Physical Models and Laboratory Techniques in Coastal Engineering.* USA: Coastal Engineering Research Center, 1993.

Stuart, Coles. (2001). *An Introduction to Statistical Modeling of Extreme Values.* London: Springer Series in Statistics, 2001.

Symonds, A. M., Vijverberg, T., et al. (2017). COMPARISON BETWEEN MIKE 21 FM, DELFT3D AND DELFT3D FM FLOW MODELS OF WESTERN PORT BAY, AUSTRALIA. Coastal Engineering Proceedings, 1(35), currents.11. https://doi.org/10.9753/icce.v35.currents.11

Thompson, Paul, Dominic et al Reve. (2009). «Automated threshold selection methods for extreme wave analysis.» *Coastal Engineering*.

Troch, P. (2001). *Experimental study and numerical modelling of pore pressure attenuation inside a rubble mound breakwater. PIANC bulletin, 109, 1-27*.

Verhaeghe, H., Meer, J. W., et al. (2003). Wave overtopping database as the starting point for a neural network prediction method. doi:10.1061/40733(147)35

Winkel, S. (2020). *Improving the breakwater design process by using a design automation tool.* Pays-Bas: Delft University of Technology.

Annex A Business model canvas

The Business Model Canvas (BMC) helps to understand and communicate the fundamental logic of businesses in a structured manner. This tool reveals the key components of the economic model and stimulates a deeper reflection on stakeholders, revenues, costs, competitive advantages, and growth opportunities. It is used in strategic planning and the development of new products and services. In this section of our thesis, we provide a detailed explanation of the BMC for our startup, describing all its components.

This strategic management tool is a visual framework that consists of nine key elements. The figure illustrates these key elements.

A.1 Value proposition

This component focuses on the unique products, services, or solutions that the company offers to its customers. The objective is to determine what sets the company's offering apart from that of its competitors. It involves identifying specific features that make the company's products or services unique and appealing to customers, giving it a competitive advantage in the market.

Our company will distinguish itself from the competition by providing a unique combination of expertise in Coastal Engineering and AI-based Cartography. This approach is a new and unprecedented approach in our market. The company also aims to provide customizable training programs and technological surveillance solutions. This innovative and attractive approach will be particularly appealing to customers looking for cutting-edge risk management and coastal development solutions.

Our value propositions for customers include the following:

- The proposition of advanced solutions based on artificial intelligence (AI) for coastal engineering and coastal risk management.

- Accurate prediction and modeling of coastal processes.
- Offering cost-effective and efficient solutions for coastal planning and infrastructure development.
- Enhancing the assessment of coastal risks and risk reduction strategies.
- Improving the efficiency of finding solutions within optimal timeframes.
- These value propositions meet our customers' needs by enabling them to make informed decisions and take preventive measures to mitigate coastal risks.

A.2 Key activities

- Key activities refer to the essential actions and processes that a company must undertake to deliver its value proposition. The key activities of our company include:
- Creating predictive models for coastal issues such as wave overtopping, coastal flooding, and marine storms.
- Identifying and mapping high-risk coastal areas.
- Forecasting future extreme sea conditions. • Processing large databases. • Creating maps for various applications.
- Offering programming training using Python and specialized software in mapping and Geographic Information System (GIS) both in-person and online.
- Providing high-performance computer rentals for complex operational simulations.

The figures illustrate the results of the applications carried out in the Bay of Algiers, which have resulted in the following prototypes.

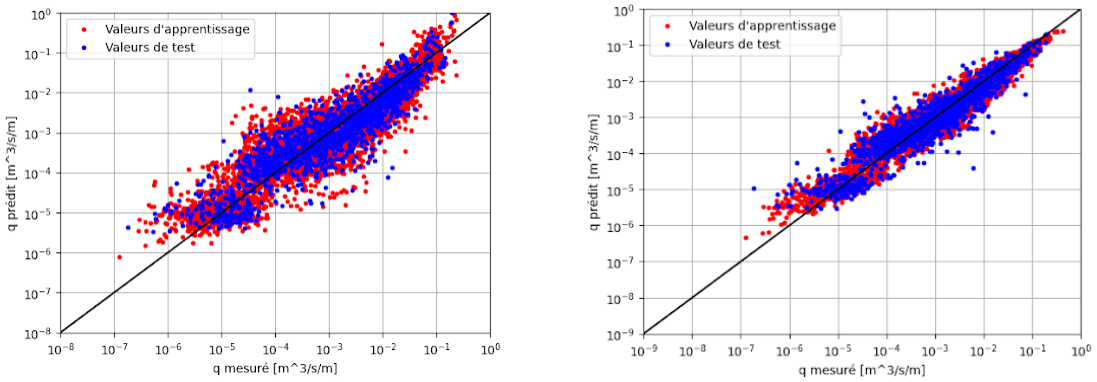

Figure 1 Application of Machine Learning for predicting wave overtopping on rubble mound breakwater

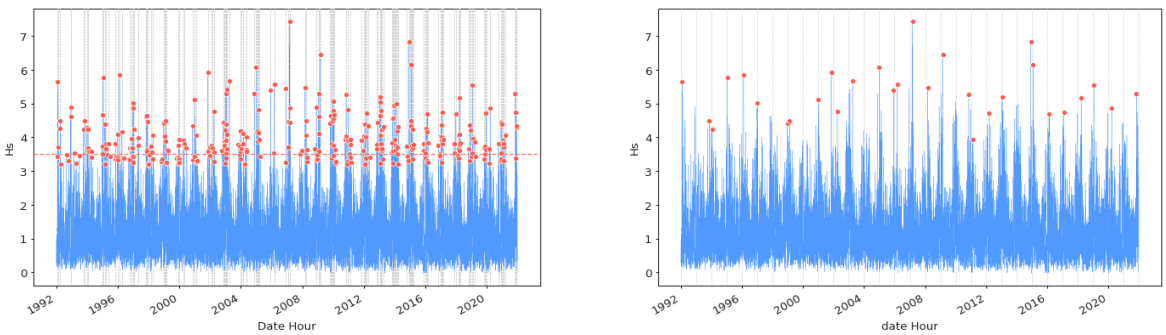

Figure 2 Prediction of extreme events using the Python programming language.

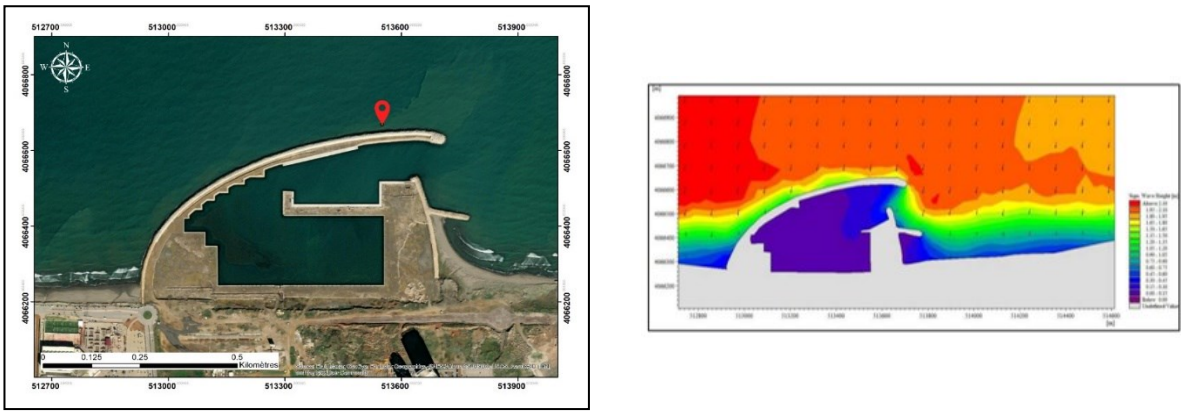

Figure 3 Mapping of the Algiers Marina and modeling of the hydrodynamics in that area.

Table 1 The projected production by year

Période	Etude	Formation	Vente de cartes	Location d'un PC puissant
1ère année	6 Etudes	5	15	5
2èmeannée	8 Etudes	15	30	10
3ème année	12 Etudes	20	45	15

A.3 Key partners

These are the strategic partnerships and alliances that the company establishes as part of its goal to create, distribute, and optimize the value proposition. Our company aims to establish partnerships with:

- Government coastal management agencies: By providing them with services, we aim to enhance their coastal management capabilities using predictive models for coastal issues. This would also help improve the safety of coastal zones, enable informed decision-making in planning and risk reduction, and better protect communities living along the coast.
- Environmental organizations for coastal preservation and protection: These organizations would be interested in purchasing our services to access mapping and modeling tools for high-risk coastal areas. This would enable them to better understand the effects of climate change on coastal zones, develop strategies for preserving the coastal ecosystem, and promote awareness for better management of these areas.
- Construction and coastal development companies: These companies would be interested in our services to benefit from AI-based solutions for accurate prediction and modeling of coastal processes. This would assist them in planning and executing their construction and coastal development projects more efficiently, reducing risks, optimizing resources, and improving the sustainability of infrastructure.

A.4 Customer segments

This element involves describing the different groups of customers that the company aims to reach and serve. It includes identifying the demographic characteristics, needs, behaviors, and

preferences of each customer segment. After conducting a market study, the following target customers have been selected:

- Agence Nationale des Changements Climatiques: They would be interested in our services to access predictive models and data on wave breaking and marine submersions related to climate change. Furthermore, this would enable them to assess the future impacts of climate change on coastal areas, develop adaptation strategies, and provide recommendations for the sustainable management of coastal ecosystems.
- Délégation Nationale aux Risques Majeurs: They would be interested in our services to strengthen national capacities for coastal risk prevention and management. This will enhance preparedness for emergency situations, coordinate response measures, and reduce human and economic losses caused by extreme coastal events.
- Office national de la météorologie: They would be interested in our services to improve the forecasting of extreme sea states. This would enable them to provide more accurate information about weather and oceanographic conditions, which is necessary for navigation management and ensuring safety at sea.
- Directions de travaux publics: They are interested in our services to improve the assessment of coastal risks in the planning and management of public infrastructure. This would also enable them to make informed decisions regarding the construction, maintenance, and repair of coastal structures. These decisions would help minimize the risks of flooding and damages caused by extreme coastal events.
- Students, researchers, and engineers: They will be interested in our services to enhance their programming skills using the Python language and gain access to specialized software in mapping and GIS (Geographic Information System). This will improve their expertise in the field of coastal engineering, coastal phenomena modeling, and risk management. These training programs will be beneficial for their professional careers and research projects.

A.5 Customer relations

This component refers to the types of relationships that the company establishes to maintain a long-term relationship with its clients.

In order to maintain a lasting relationship with our clients, our company focuses on close collaboration with them. We will offer personalized consultations to understand the specific needs of our clients and provide them with tailored solutions. Regular updates on new AI and mapping technologies in the field will be provided to keep clients informed of the latest advancements.

The relationships with our clients will be built through ongoing communication, feedback, and discounts on offered training programs.

A.6 Distribution channels

Distribution channels are the means through which a company communicates, distributes, and sells its products or services to its customers.

The distribution channels for the services offered by our company include:

- Utilizing an online platform as a sales channel for selling coastal engineering-specific AI models and tools.
- Direct sales and consultations with various businesses.
- Participating in conferences and trade shows to promote AI solutions in the field of coastal engineering.

A.7 Key resources

Key resources refer to the tangible and intangible assets required to operate the company. The resources necessary for the smooth functioning of our business are:

- Expertise in research and development of artificial intelligence (AI) techniques.
- Powerful and efficient computer hardware.
- Qualified personnel in mapping and programming.
- Distributors and wholesalers of necessary supplies (paper, pens, markers, etc.).
- Access to data on coastal engineering and the environment.

The () outlines the essential resources along with their costs to create and develop our business.

Table 2 List of requirements for starting a business

Besoins	Nombre	Prix
Local (50 m^2)	1	À partir de 1,200,000 DA/an
Matériel Informatique : PC Imprimante Scanner Logiciels	 5 1 /	 1,600,000 DA 46,000 DA 0 DA
Matériel Bureautique : Bureaux Chaises Armoires Tableau	 5 8 4 1	 105,000 DA 188,000 DA 100,000 DA 7,000 DA
Fourniture: Papiers Ancre Stylos/Marqeur/Registres	 6 Rames /an 48 Cartouches/an -	 4,500 DA/an 19,200 DA/an 12,000 DA/an
Autres : Climatiseur Electricité/Eau Abonnement internent	 1 / /	 70,000 DA En Moyenne 64,000 DA/an 34,000 DA/an
Ingénieur en programmation	1	Salaire Brut : 800,000 DA/an
Création de Plateforme pour vente de services Site web de l'entreprise Outil de E-payement (devise/dinars)	1 1 1	300,000 DA 400,000 DA 150,000 DA
Total	5,099,700 DA	

A.8 Revenue sources

This section pertains to the various sources of income for the company. These sources can be summarized as follows:

• Direct sales of predictive models for coastal issues to government agencies, construction companies, and environmental organizations.

• Sale of mapping and modeling services for high-risk coastal areas.

• Sale of programming and specialized software training in mapping and GIS.

• Rental of high-performance PCs for complex operation simulations.

• Sale of maps for various applications.

• Advertising revenue on the online platform.

A.9 Cost structure

This component relates to the costs associated with operating the business. This includes both fixed costs and variable costs.

Fixed costs:

- Rent.
- Insurance.
- Salaries and social security charges for personnel.
- Water and electricity.
- Internet.

Variable costs:

- Repair and maintenance of office and computer equipment.
- Advertising.
- Distribution.
- Supplies.
- Operating and maintenance expenses of the platform.

Table 3 Cost of services for a duration of one year.

Service	Prix	Nombre	Total de la 1ère année
Etude	200,000 DA	6	120,0000 DA
Formation	12,000 DA	5	60,000 DA
Carte	2000 DA	15	30,000 DA
Location	2000 DA	5	10,000 DA

A.10 Business model Canvas summary

The table summarizes our economic model on a single page.

Figure 4 Business Model Canvas

A.11 Conclusion

In conclusion, the creation of our Business Model Canvas (BMC) has provided us with a clear and comprehensive view of our entire economic model. Through this model, which encompasses the nine key components, we now have a structured and visual approach that serves as a powerful tool to understand, analyze, explain, and effectively communicate our startup idea. The BMC has allowed us to highlight the relationships and interactions among different parts of our business, assisting us in making informed decisions and identifying potential areas for improvement. By establishing strong connections between our unique value proposition, customer segments, distribution channels, revenue sources, and strategic partnerships, we have created a solid overall vision for our project. This process has also shed light on the opportunities and challenges we will face, enabling us to refine our approach and prepare for the success of our business. With this BMC in hand, we are ready to confidently and determinedly move on to the next stage of our entrepreneurial journey.

Annex B Extreme events results

Threshold selection and POT results

Mean residual life plot	Peaks Over Threshold (POT) extreme values
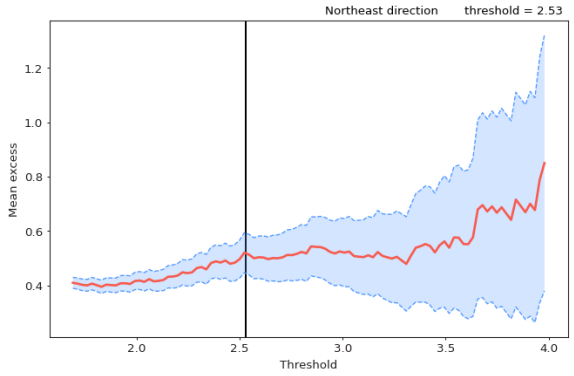	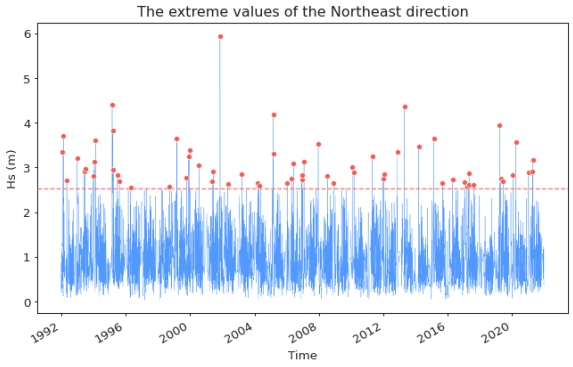
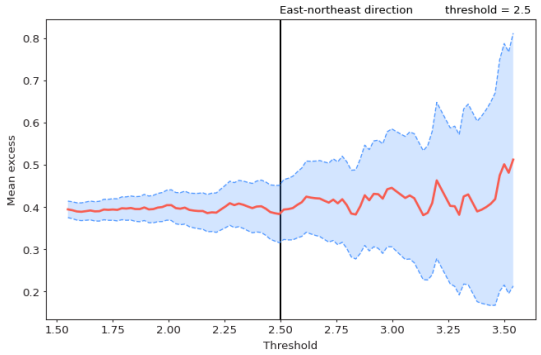	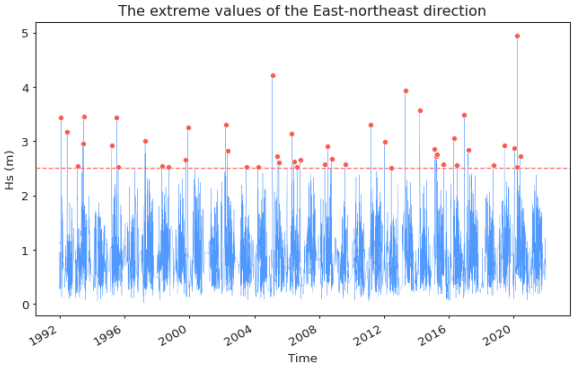
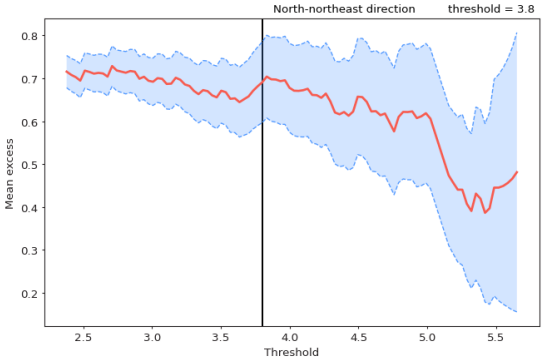	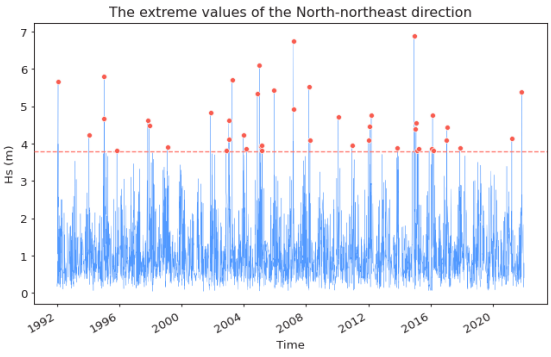
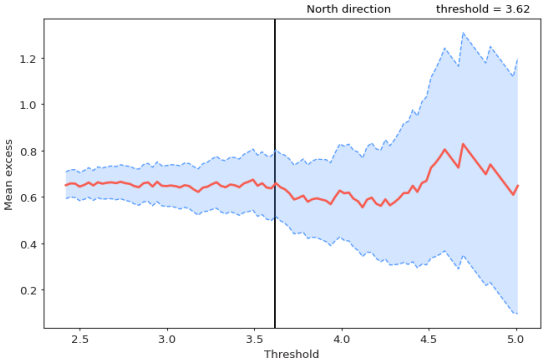	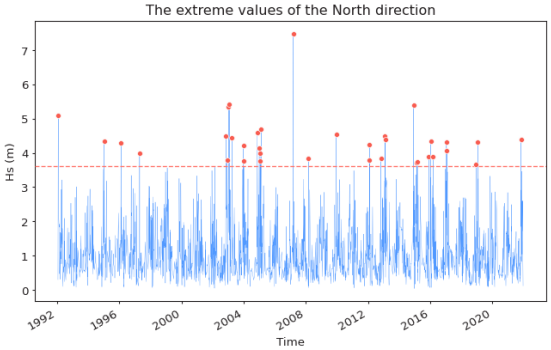

Mean residual life plot	Peaks Over Threshold (POT) extreme values
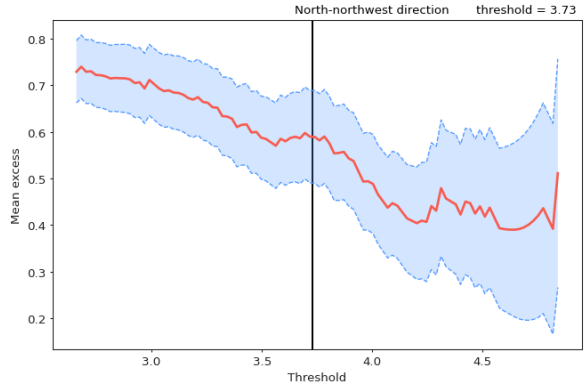	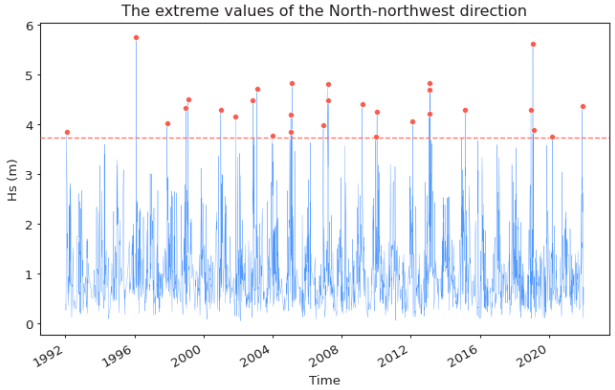
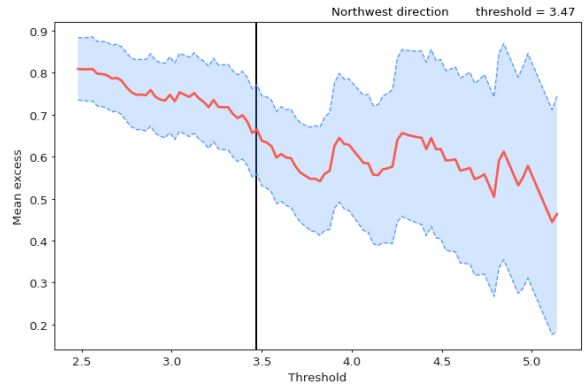	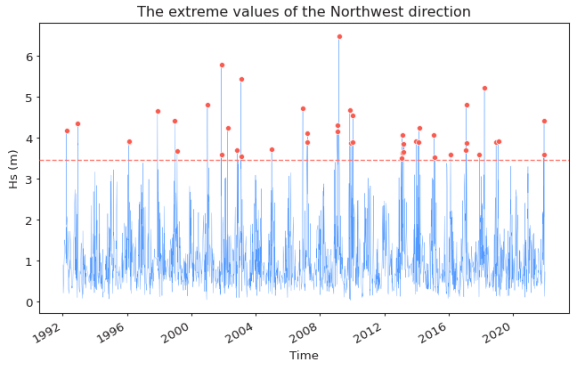
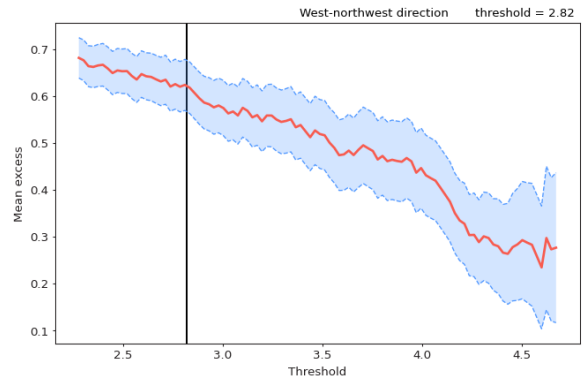	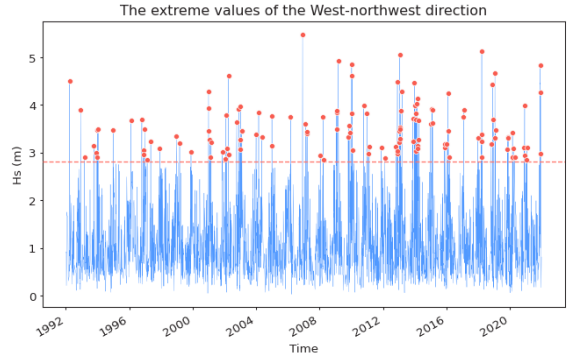
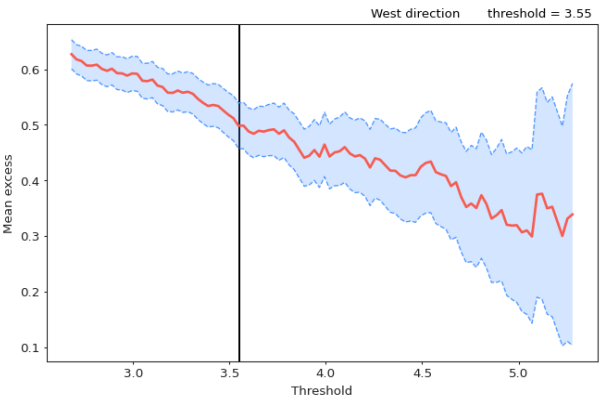	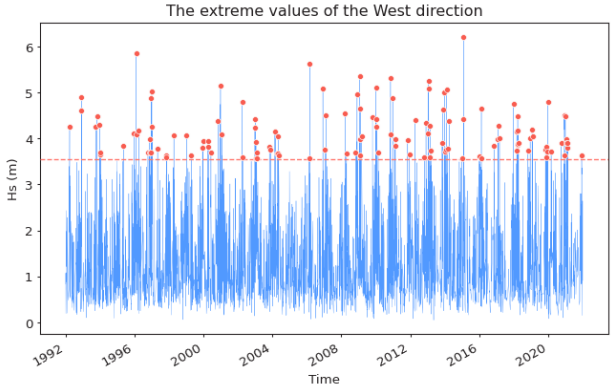

Annex C Numerical simulations results for 100 years return period

North direction

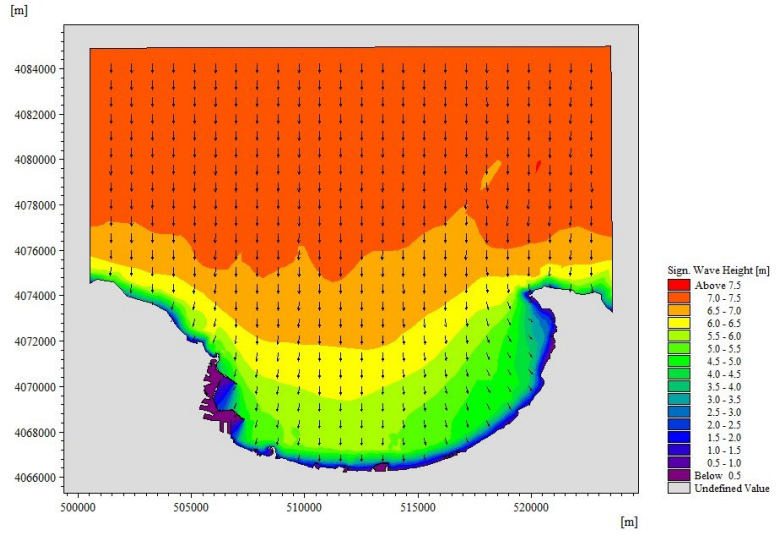

Northeast direction

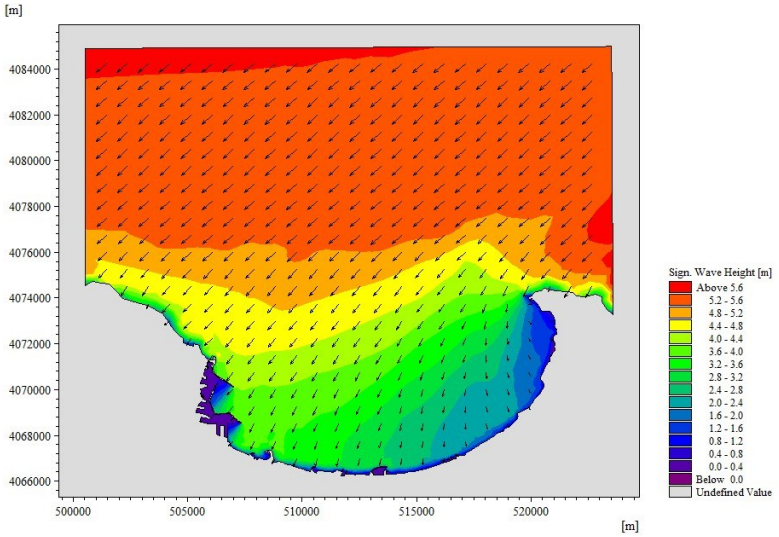

North Northwest direction

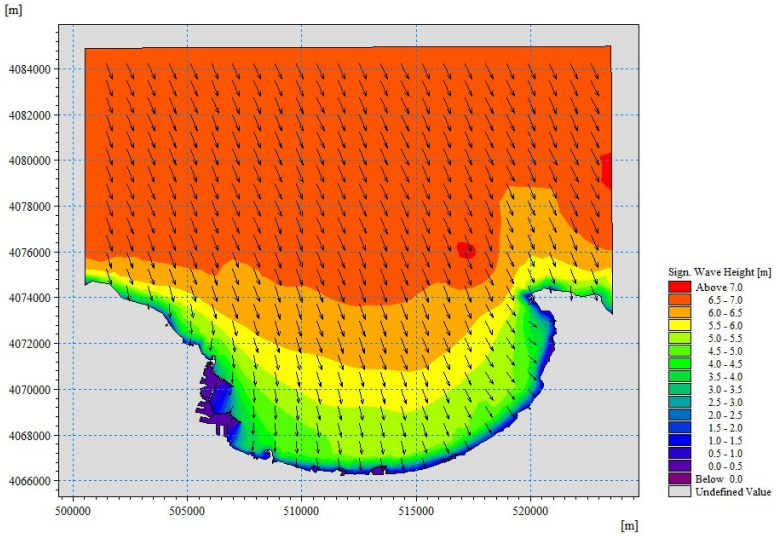

North direction

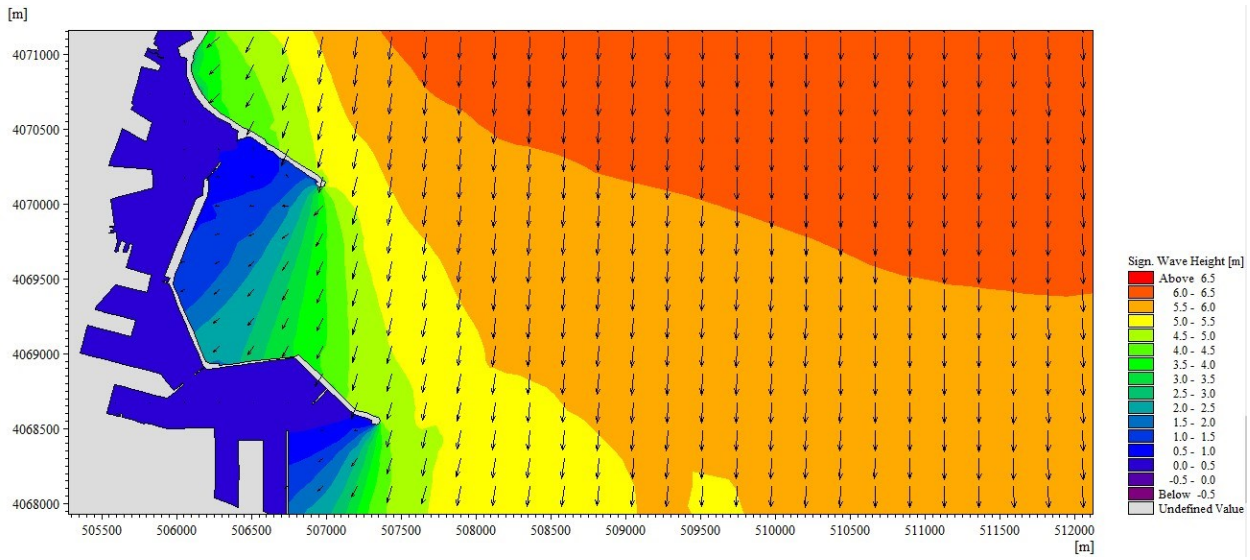

Northeast direction

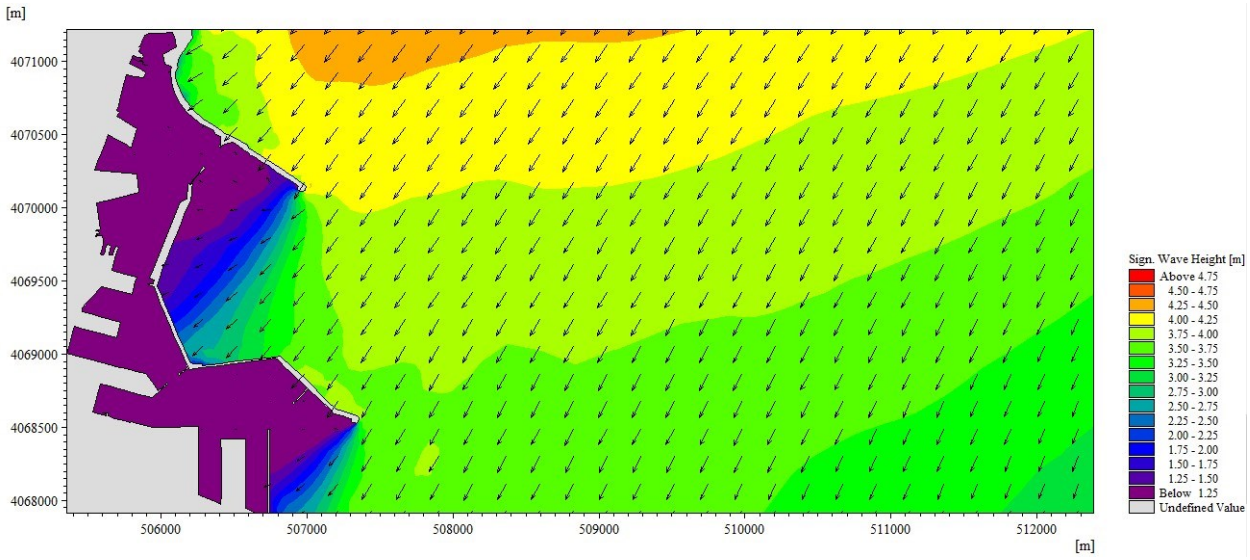

North Northwest direction

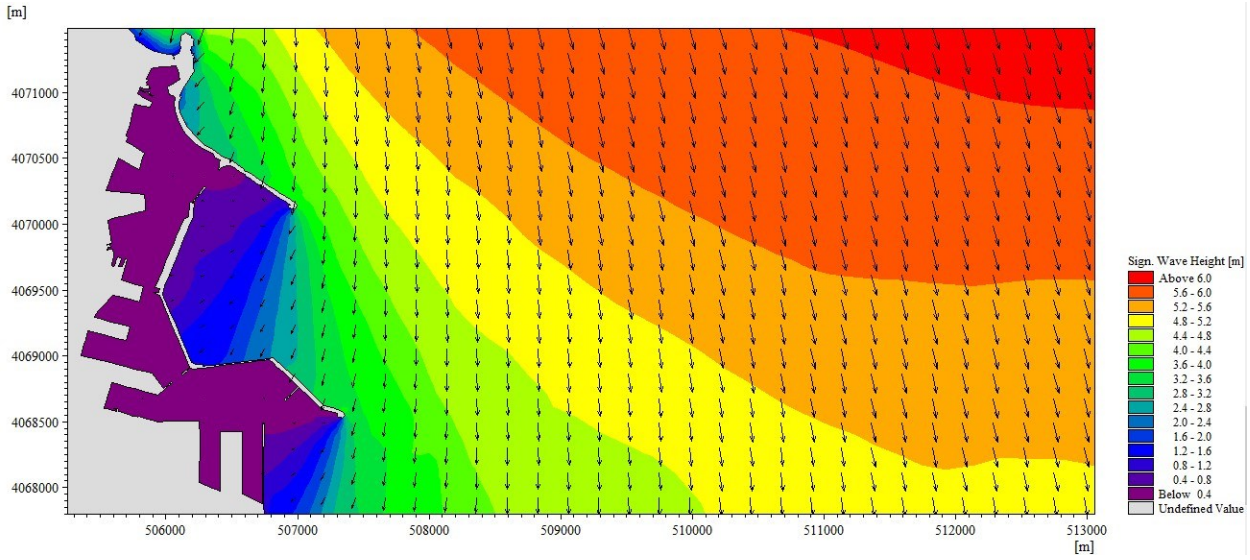

North direction

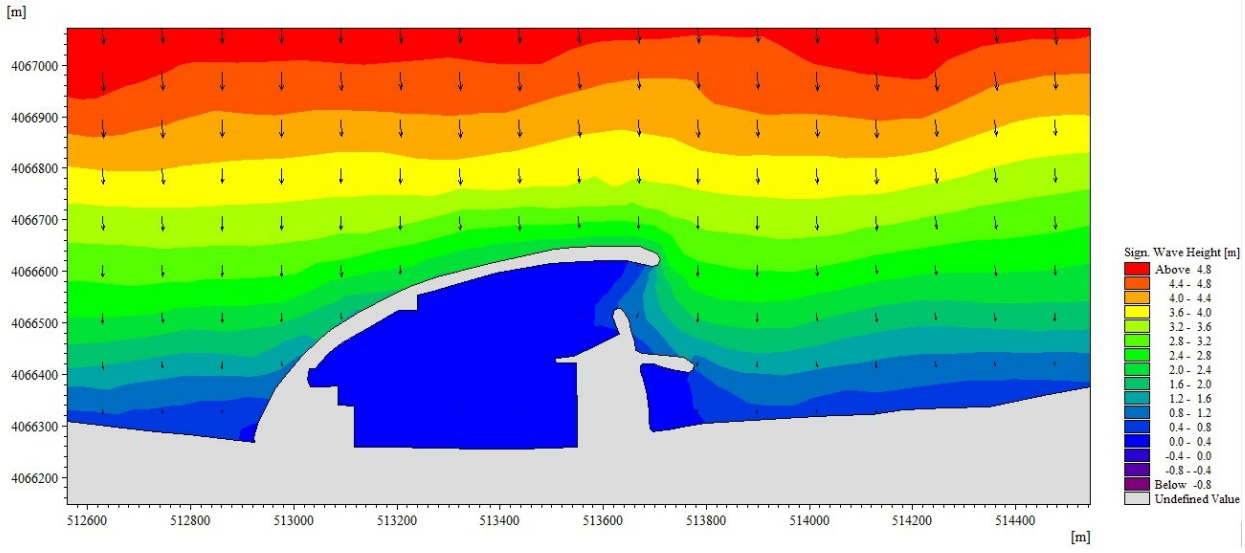

Northeast direction

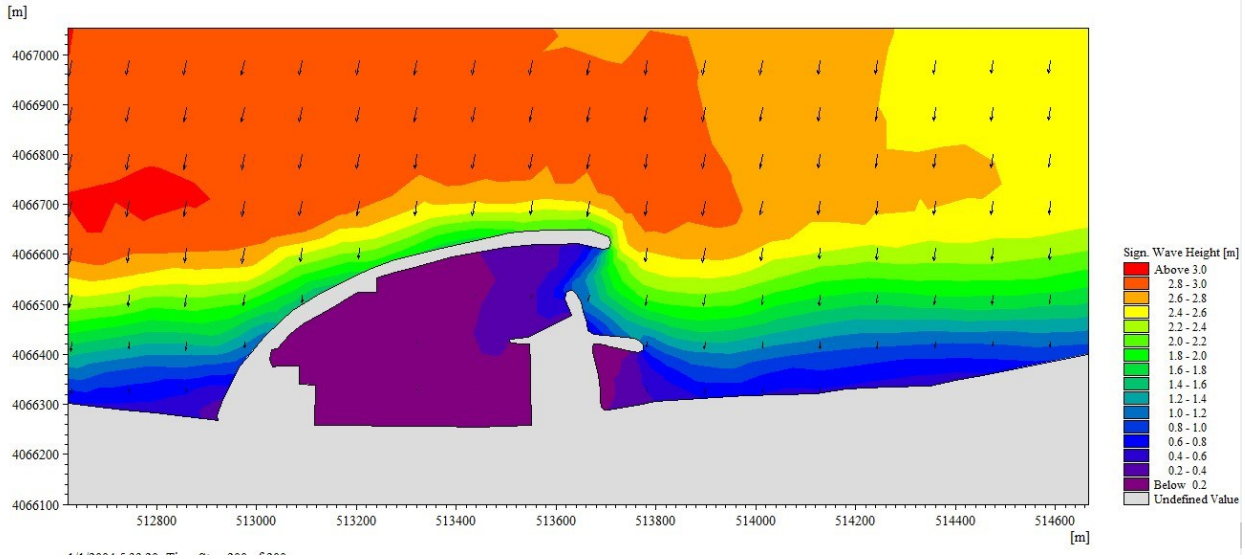

North Northwest direction

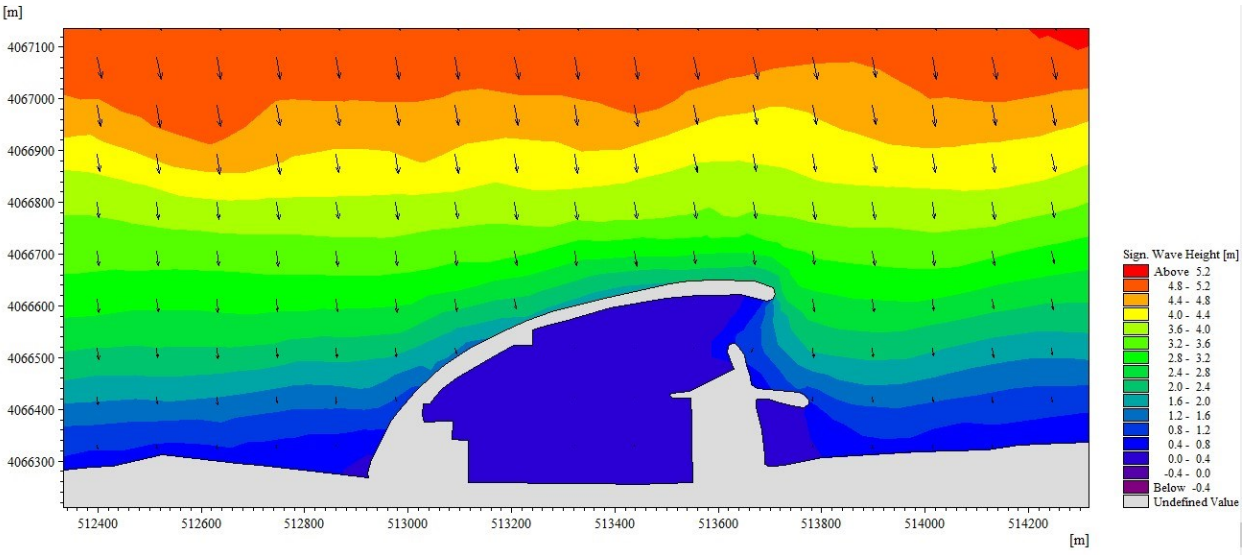

North direction

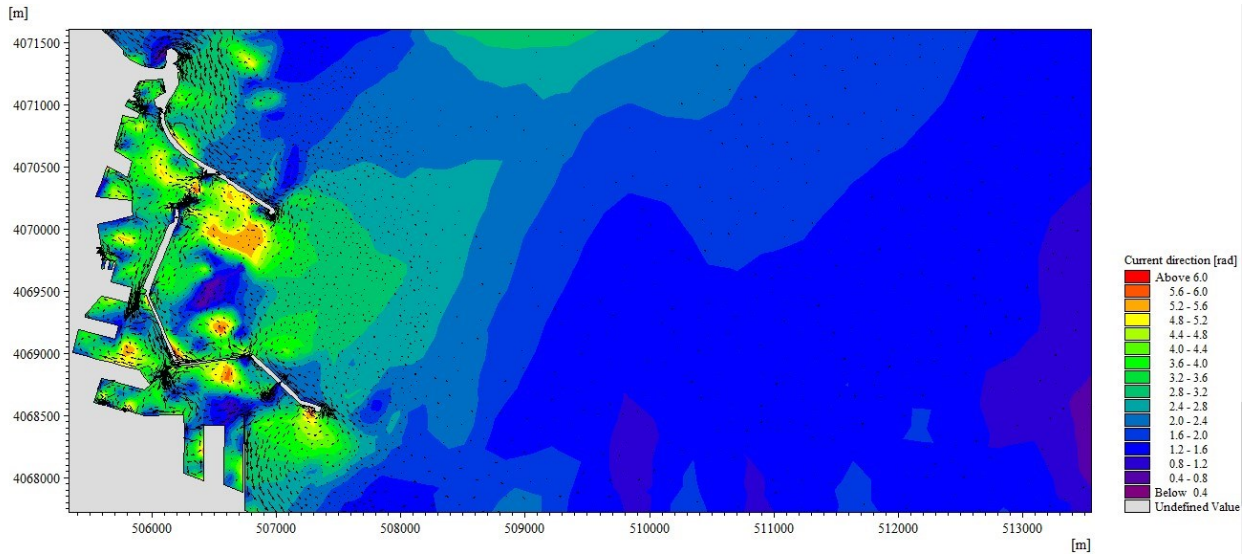

Northeast direction

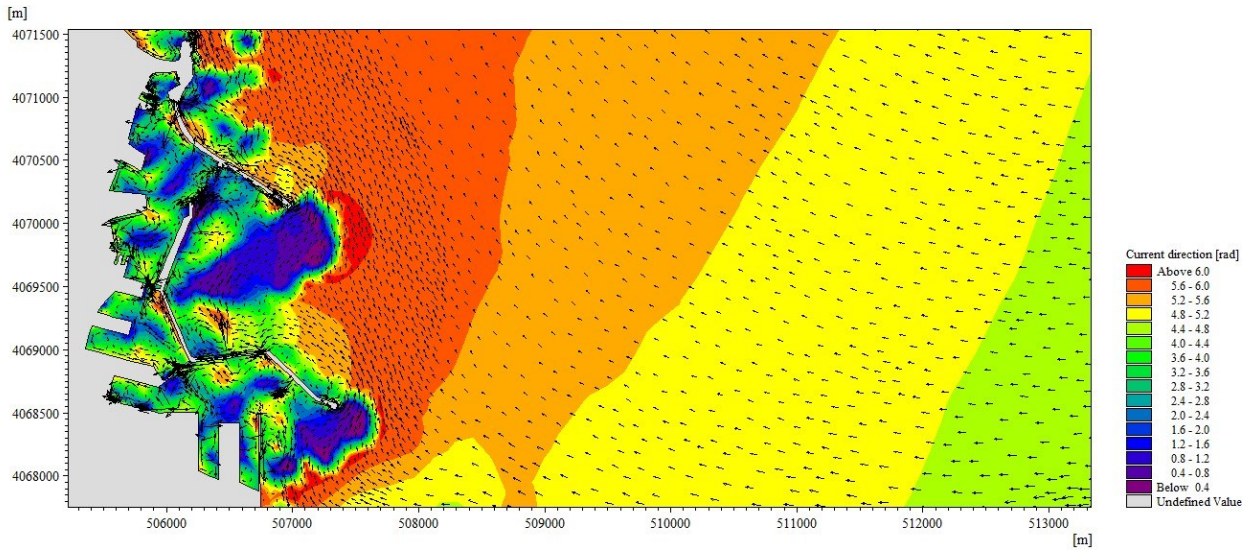

North Northwest direction

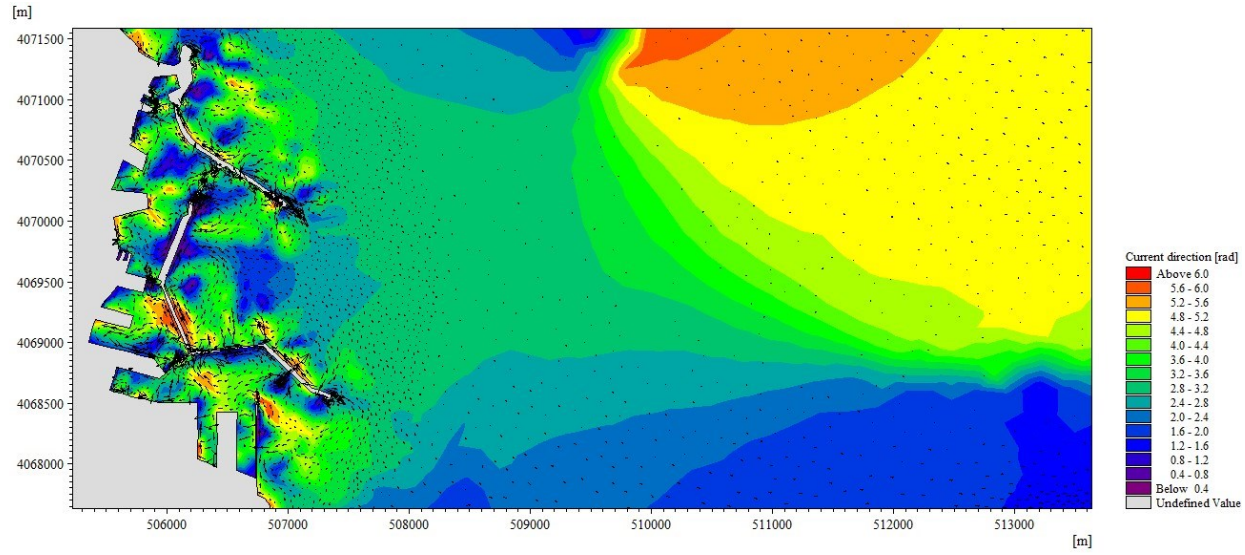

North direction

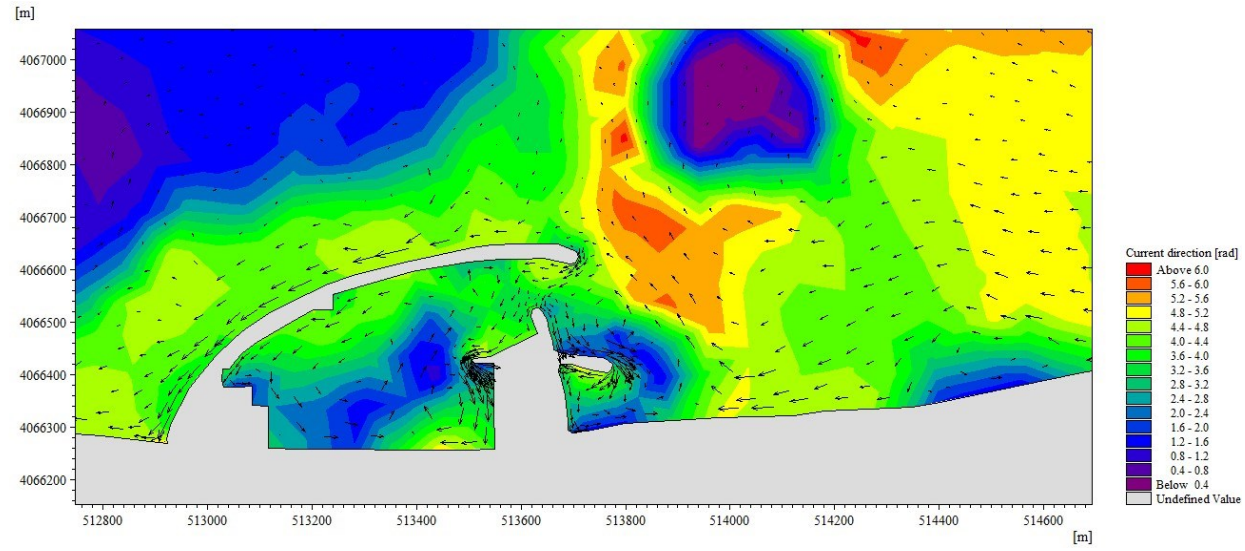

Northeast direction

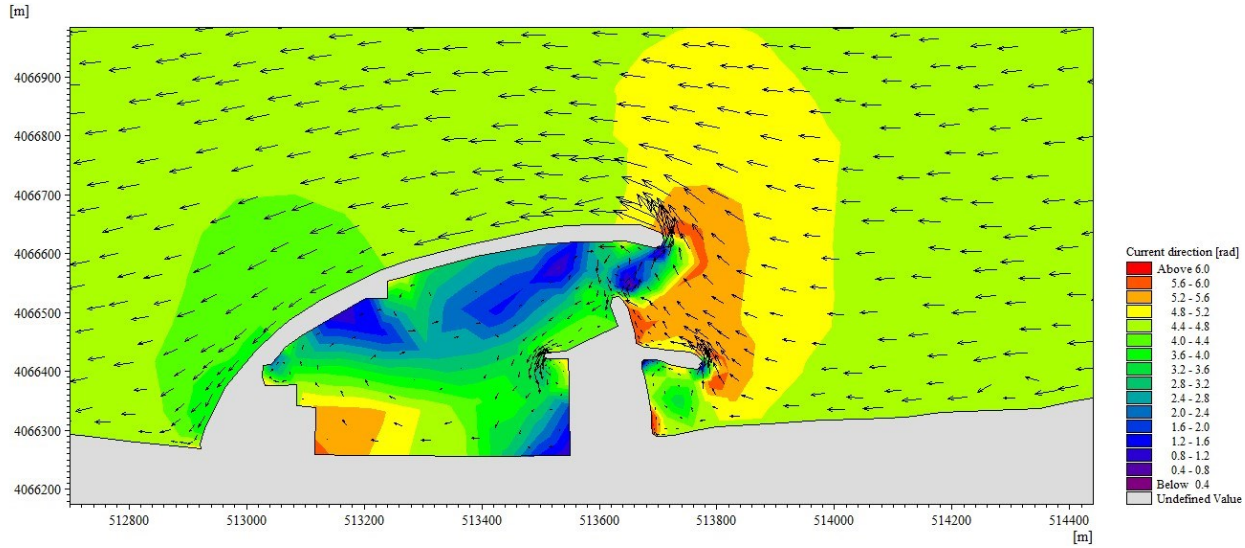

North Northwest direction